Journal of Marine Technology and Environment

Vol.II, year 2026

Editura
NAUTICA

Journal of Marine
Technology and Environment
DOI:10.53464/JMTE.02.2026

ISSN (Print): 1844-6116
ISSN (Online): 2501-8795
https://www.jmte.eu

Journal of Marine Technology and Environment **Year 2026, Vol. 2**

Journal of Marine
Technology and Environment
DOI:10.53464/JMTE.02.2026

ISSN (Print): 1844-6116
ISSN (Online): 2501-8795
https://www. jmte.eu

ISSN (Print): 1844-6116

ISSN (Online): 2501-8795

Journal of Marine Technology and Environment
DOI: 10.53464/JMTE.02.2026
ISSN (Print): 1844-6116
ISSN (Online): 2501-8795
https://www. jmte.eu

This Journal has been founded in 2008 as a biannual publication of Constanta Maritime University/ROMANIA

Topic: MARITIME AREAS

- Marine Science and Engineering
- Marine Environmental Issues
- Marine Renewable Energy and Sustainability
- Maritime Safety
- Climate changes
- Cyber Security and Maritime Technologies

Journal of Marine
Technology and Environment
DOI: 10.53464/JMTE.02.2026

ISSN (Print): 1844-6116
ISSN (Online): 2501-8795
https://www. jmte.eu

Journal of Marine Technology and Environment
DOI: 10.53464/JMTE.02.2026
ISSN (Print): 1844-6116
ISSN (Online): 2501-8795
https://www. jmte.eu

Journal of Marine
Technology and Environment
DOI: 10.53464/JMTE.02.2026

ISSN (Print): 1844-6116
ISSN (Online): 2501-8795
https://www. jmte.eu

Journal of Marine Technology and Environment
DOI: 10.53464/JMTE.02.2026

ISSN (Print): 1844-6116
ISSN (Online): 2501-8795
https://www. jmte.eu

JOURNAL ADDRESS

Journal of Marine Technology and Environment

Constanta Maritime University, 104, Mircea cel Batran Street, 900663, Constanta, Romania

Tel: +40 241 664 740/ 107

Fax: +40 241 617 260

E-mail: office@jmte.eu
https://jmte.eu/

NAUTICA PUBLISHING HOUSE CONSTANTA, ROMANIA

CONSTANTA MARITIME UNIVERSITY, 104, MIRCEA CEL BATRAN STREET, 900663, CONSTANTA, ROMANIA

EDITOR IN CHIEF – PROF. ENG. PANAITESCU MARIANA PHD. CONSTANTA MARITIME UNIVERSITY

email: mariana.panaitescu@cmu-edu.eu

CONTENTS

Journal of Marine Technology and Environment
DOI:10.53464/JMTE.02.2026.01
ISSN (Print): 1844-6116
ISSN (Online): 2501-8795
https://www. jmte.eu

A CELESTIAL NAVIGATION APPROACH TO SALAH TIMEKEEPING FOR SEAFARERS

Alina BUSLĂ[1], Feiza MEMET[2]

[1] Constanta Maritime University, Department of Navigation, Constanta, Romania, e-mail: alina.busla@cmu-edu.eu
[2] Constanta Maritime University, Department of General Engineering Sciences, Constanta, Romania, e-mail: feiza.memet@cmu-edu.eu

Abstract: Ensuring religious practices on board ships is essential for the wellbeing of practicing seafarers. Around 18% of seafarers on board merchant ships are Muslim, and practicing seafarers perform Salah – five prayers a day. The prayers must be performed at appointed times during the day, times which depend on the movement of the sun; this is why astronomy is essential for the Islamic world. Presently, astronomical calculations are used to find the right prayer times, and prayer times across the world are available on the Internet, in tables, for major cities on all continents. Since prayer times depend on location, the objective of this paper is to provide seafarers with Salah times with the help of nautical astronomy calculus. This paper presents a method that allows the use of two successive sights taken at two different stars as if they were two simultaneous sights, by reducing the first observation to the zenith of the second observation or vice versa. At least two astronomical lines of position are required to obtain an astronomical fix, meaning two simultaneous sights at two different celestial bodies; however, only the officer on watch is usually on deck and cannot take two simultaneous sights, and the moving vessel changes its dead reckoning position between the two observations. Science and religion are not in antagonistic positions; they may coexist by jointly addressing aspects of human life. The present study may serve as guidance for Muslim seafarers during their voyages in fulfilling their religious obligations.
Key words: Astronomical fix; Celestial navigation; Muslim seafarers; Nautical astronomy; Prayer times (Salah); Same altitude method.

1. INTRODUCTION

Seafaring is a profession characterised by cultural diversity, and performance on board is affected by a friendly environment for the religious practices of seafarers. Around 18% of the seafarers on board merchant ships are Muslim [12], with practicing seafarers finding support in prayer and other practices associated with their faith.

Among the obligations that a Muslim must follow is Salah [1]. This means that the believer is expected to pray five times a day, at appointed times. These five times depend on the movement of the sun, which is why astronomy plays an essential role in Islam.

The five daily mandatory prayers are: *Fajr* (early morning prayer) – between the appearance of dawn and sunrise; *Dhuhr* (midday prayer) – beginning after the sun has passed the meridian and ending just before the start of *Asr*; *Asr* (afternoon prayer) – from the late afternoon until the yellowing of the sun; *Maghrib* (evening prayer) – lasting as long as twilight; and *Isha* (night prayer) – between sunset and midnight.

Presently, the right prayer times are found through astronomical calculations.

Across the world, prayer times are available on the Internet, provided in tables for major cities on all continents. Since prayer times depend on location, this paper aims to provide seafarers with the right Salah times during sea voyages by using nautical astronomy calculus.

The goal of this paper is to present a method that allows the use of two successive sights taken at two different stars as if they were two simultaneous sights. This can be done by reducing the first observation to the zenith of the second observation, or vice versa.

At least two astronomical lines of position are required to obtain an astronomical fix, meaning two simultaneous sights at two different celestial bodies. Usually only the officer on watch is on deck, and cannot take two simultaneous sights at two different stars. Moreover, since the ship is moving on the surface of the Earth, the second sight is made from another dead reckoning position; as is known, a fix by two simultaneous observations requires the same DR position for both observations.

2. RESEARCH METHODOLOGY

Journal of Marine Technology and Environment
DOI:10.53464/JMTE.02.2026.01
ISSN (Print): 1844-6116
ISSN (Online): 2501-8795
https://www. jmte.eu

2.1 *Horizon and zenith, altitude and zenith distance*

One of the main lines of the celestial sphere is the zenith-nadir line. This line connects the centre of the Earth's sphere with the point where the observer is located. The extension of this line above the observer's head intersects the celestial sphere at the point called zenith. The diametrically opposed point of the zenith is called nadir.

When an altitude is measured at a star, its image is brought with the help of the sextant onto the plane of the observer's horizon. For simplicity, we use the term *observer's horizon* to represent the plane perpendicular to the zenith-nadir line that passes through the observer's eye. The circle that connects the zenith with the nadir and passes through the observed star is called the *vertical circle* of the star; it is perpendicular to the plane of the observer's horizon. The arc of a vertical circle measured from the horizon to the centre of the star is called *altitude*; the arc measured from the zenith to the centre of the star is called the *zenith distance*.

As the vessel moves on the Earth's surface, its position changes over time, and the position of the zenith on the celestial sphere changes accordingly. This determines a variation in the position of the plane of the observer's horizon with respect to the terrestrial sphere, and hence a variation in the value of the star's altitude and zenith distance.

As a result, the altitude measured at a star – considered immobile on the celestial sphere – will increase due to the movement of the ship if the star is sighted forward of the vessel, and will decrease if the star is sighted astern (Figure 1).

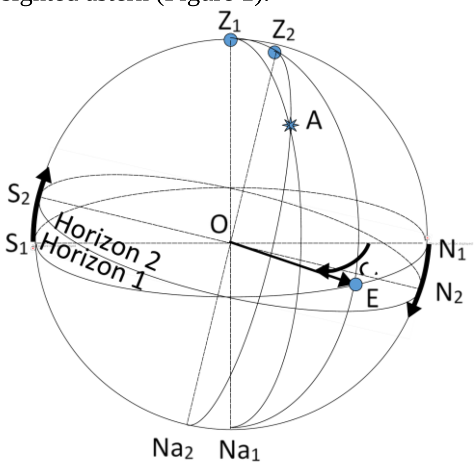

Figure 1 Variation of altitude and zenith distance due to the ship's movement

We note from here that the altitude and zenith distance of a star are constantly changing as a result of the movement of the ship on the Earth's surface.

2.2 *Variation of zenith distance due to the ship's movement*

Suppose that at chronometer time CT_1, in dead reckoning position DR_1, star A is sighted at altitude H_1. The zenith point Z_1 corresponds to the observer's (vessel's) position at that moment. The star's position is considered fixed, unaffected by diurnal motion.

After a time interval (ΔT), in dead reckoning position DR_2, the same star is sighted at altitude H_2. The chronometer time for this moment is CT_2.

As can be seen below (Figure 2), the arc Z_1Z_2 represents the projection on the celestial sphere of the distance (D) travelled by the vessel in the time interval between the two observations. The value of the arc, expressed in arc minutes, is therefore equal to the value of the distance D in nautical miles:

$$\widehat{Z1Z2} = D \tag{1}$$

The zenith distances (z) corresponding to the two observations are Z1A and Z2A, since the star is assumed to have no diurnal motion (Figure 2):

$$z1 = \widehat{Z1A} = 90° - H1 \tag{2}$$

$$z2 = \widehat{Z2A} = 90° - H2 \tag{3}$$

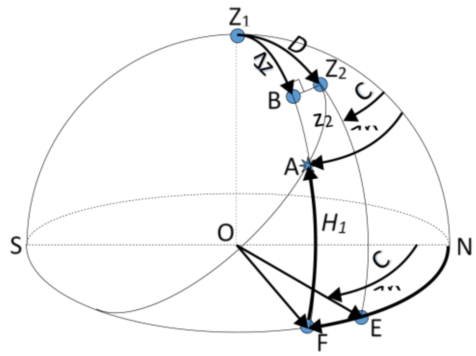

Figure 2 Geometry of the same-altitude reduction between two star sights

From point Z_2, draw a spherical perpendicular to the vertical circle of the star corresponding to the first zenith, and label the point of intersection B.

The arc Z_2B represents the projection of the horizon arc EF on the celestial sphere. As can be seen in Figure 2, the arc EF has as its value the difference between star A's azimuth (Zn) and the ship's course (C):

$$\widehat{EF} = Zn - C \tag{4}$$

The arc Z_1B represents the variation of the zenith distance (Δz) of star A. Notice that the spherical triangle Z_1-Z_2-B is formed; being very small compared to the celestial sphere, it can be treated as a plane triangle. As a result:

$$\widehat{Z1B} = \Delta z = -D \cdot cos\ (Zn - C) \quad (5)$$

Note: the right-hand side of the above equation is negative because the altitude increases due to the lowering of the horizon as the ship moves towards the star.

2.3 Altitude variation due to the ship's movement

Between the variation of the zenith distance of a star (Δz) and the variation of its altitude (ΔH) there is the following relation:

$$\Delta H = |\Delta z| \quad (6)$$

where ΔH = |Δz| represents the variation of altitude due to the movement of the vessel between the two observations, over the travelled distance D. As a result, the above equation can take the following form:

$$\Delta H = D \cdot cos(Zn - C) \quad (7)$$

To calculate the distance between the two dead reckoning positions, the following formula is used: Distance (D) = speed (S) × time (ΔT). For time, the following relation is used:

$$\Delta T = CT2 - CT1 \quad (8)$$

$$\Delta H = S \cdot (CT2 - CT1) \cdot cos\ (Zn - C) \quad (9)$$

Considering the speed in knots and ΔT in minutes, the above relation becomes:

$$\Delta H = \frac{S}{60} \cdot (CT2 - CT1) \cdot cos\ (Zn - C) \quad (10)$$

where S/60 represents the speed in nautical miles per minute.

The algebraic sign of the altitude variation (ΔH) is positive (+) if the vessel moves toward the star, and negative (–) if the ship moves away from the star.

The distance D may also be determined using log indications (LI); in this case the altitude variation is:

$$\Delta H = f \cdot (LI2 - LI1) \cdot cos(Zn - C) \quad (11)$$

Note that Zn – C corresponds to the relative bearing of the star (RB).

- **Practical considerations**

– the distance D is determined using the formula D = S × T, or from the difference between the log indications for the two observations, multiplied by the log correction factor (f):

$$D = f \cdot (LI2 - LI1) \quad (12)$$

– time T is given by the difference between the chronometer indications for each of the two observations (see formula (8));

– the azimuth (Zn) is determined following the algorithm for calculating the elements of the astronomical LOP;

– the term cos(Zn – C) – the relative bearing – has the following algebraic sign:

– plus (+) if the relative bearing (Z_n – C) is between 0–90° and 270–360° (the star is forward of the beam);

– minus (–) if the relative bearing (Z_n – C) is between 90–270° (the star is abaft the beam).

– the altitude variation (ΔH) reaches its maximum when the star is in the bow or astern, and equals zero when the star is abeam.

- **Working algorithm**

– make the observation at the first star and note the sextant index, chronometer time (CT_1) and log indication (LI1);

– make the observation at the second star and note the sextant index, chronometer time (CT_2) and log indication (LI2);

– determine the DR position for the second observation;

– calculate the travelled distance (D) between the two observations;

– calculate the elements of the first astronomical LOP_1: azimuth (Zn_1) and intercept (a1);

– calculate the altitude variation of the first observation (ΔH) due to the travelled distance D;

– apply the altitude variation to the first intercept to obtain the reduced intercept a'1 (a'1 = a1 + ΔH); the first LOP elements are then LOP_1: Zn_1, a'1;

– calculate the elements of the second astronomical LOP: LOP_2: Zn_2, a_2;

– plot the two LOPs; their intersection gives the astronomical fix of the vessel;

– extract the geographical coordinates of the astronomical fix.

3. RESULTS AND DISCUSSION

The effectiveness of the same-altitude method depends on minimising the errors introduced by dead reckoning between observations. The time interval between the two sights should therefore be sufficiently short, and the vessel's speed and course must be known precisely. When properly executed, the method provides a reliable and elegant means of obtaining a navigational fix using fundamental astronomical principles. Since both altitude measurements are taken at similar angles

Journal of Marine Technology and Environment
DOI:10.53464/JMTE.02.2026.01
ISSN (Print): 1844-6116
ISSN (Online): 2501-8795
https://www.jmte.eu

and with the same instrument, systematic errors (index error, dip) tend to cancel out.

Astronomical observations are most effective during astronomical night, when the Sun is more than 18 degrees below the horizon, eliminating residual twilight and providing the darkest possible sky. In most regions this window begins approximately 1.5–2 hours after sunset and ends about 1.5–2 hours before sunrise, maximising the visibility of faint celestial objects and minimising interference from scattered sunlight.

Stars such as Denebola and Arcturus are particularly well suited to this method due to their brightness, well-known positions and wide separation in right ascension, offering flexibility in timing and redundancy for verification. The technique also enhances navigational self-sufficiency, as it does not depend on electronic aids or satellite systems, remaining a valuable and dependable alternative in traditional celestial navigation – especially on long ocean passages, where backup methods are essential for navigational safety.

The algorithm calculus is carried out according to [2]–[11].

On July 14, 2021, at chronometer time CT = 19h46m23s, the star Denebola was sighted. The sextant altitude was Hs = 64°17.7'. Height of eye is 14 m, index

correction IC = +1.5', and chronometer correction CC = +1m12s. Log indication is LI1 = 1234.5 and the log correction factor is f = 1.00; all data are available on board.

After a time interval, at chronometer time CT = 19h58m59s, in DR position Lat = 38°12'N, Lon = 040°51'W, the star Arcturus was sighted. The sextant altitude was Hs = 63°03.4'. The true course was TC = 105° and the speed S = 16 kts. Log indication is LI2 = 1237.9.

Note: the first altitude will be reduced to the zenith of the second observation (Table 1).

Table 1. Meridian angle (t) and declination (Dec)

Date	July 14, 2021	July 14, 2021
Body	Denebola	Arcturus
CT	19h46m23s	19h58m59s
CC	+ 1m12s	+ 1m12s
UT	19h47m35s	20h00m11s
IC	+ 1.5'	+ 1.5'
Alt. Corrn	- 7.2'	- 7.2'
Sum	- 5.7'	- 5.7'
Hs	64°22.5'	63°03.4'
Ho	64°16.8'	62°57.7'
GHA γ (20h)	217°51.3'	232°53.7'
Increments (m/s)	11°55.7'	0°02.8'
Total GHA γ	229°47.0'	232°56.5'
SHA	182°28.0'	145°50.4'
GHA*	412°15.0'	378°46.9'
Lon (E/W)	-040°51.0'	-040°51.0'
LHA*	371°24.0'	337°55.9'
360°	-360°	-359°59.1'
t (E/W)	011°24.0' W	022°04.1' E
Tab. Dec.	N14°27.3'	N19°04.5'

3.1 LOP 1 – Deneb Computed altitude (H_c) and intercept (a) computation.

The following formula is used to determine the computed altitude (H_c) (Table 2):

$$Hc = \underbrace{\sin Lat \,.\, \sin Dec}_{parta} + \underbrace{\cos Lat \,.\, \cos Dec \,.\, \cos t}_{partb} \quad (13)$$

Table 2. Altitude computation (Hc) – Deneb

E Lat	38°12.0' N	sin Lat	0.618408395	cos Lat	0.785856893
Dec	N14°27.3'	sin Dec	0.249619546	cos Dec	0.968343990
tW	11°24.0' W			cos t	0.980271175
Ho	64°16.8'	part a	0.154366823	part b	0.745966562

Journal of Marine Technology and Environment
DOI:10.53464/JMTE.02.2026.01
ISSN (Print): 1844-6116
ISSN (Online): 2501-8795
https://www. jmte.eu

Hc	64°12.1'	part b	0.745966562		
Intercept (a)	+ 4.7'	sin Hc	0.900333384		
		Hc	64°12.1'		

Used formulas:

$$sinZ = sin\ t \cdot secH_c \cdot cosDec \quad (14)$$

$$sinH_{PV} = sin\ Dec \cdot cosecLat \quad (15)$$

The zenith angle given by this formula has a quadrantal size (Table 3).

Table 3. Zenith angle value computation – Deneb

tW	11°24.0' W	sin t	0.197657340	HPV	
Hc	64°12.1'	sec Hc	2.297789525	sin Dec	0.249619546
Dec	N14°27.3'	cos Dec	0.968343990	cosec Lat	1.617054373
Lat	38°12' N	sin Z	0.439797599	sin HPV	0.403648378
HPV	23°48.4'	Z	26°05.5'	HPV	23°48.4'
Dec same name as Lat		Z	26°.1	180°	180°.0
Dec < Lat	Hc > HPV	Z	SW 26°.1	Z	+26°.1
				Zn	206°.1

The following tables (Tables 4–10) help to establish the quadrant of the horizon in which the body is sighted.

Table 4. Quadrant establishment

Name of Dec	Magnitude of Dec	Size of Hc	Origin (1st letter)	Direction (2nd letter)
1	2	3	4	5
contrary to Lat	-	-	contrary to Lat	same name as meridian angle
same name as Lat	Dec < Lat	Hc > HPV	contrary to Lat	same name as meridian angle
same name as Lat	Dec < Lat	Hc < HPV	same name as Lat	same name as meridian angle
same name as Lat	Dec > Lat	-	same name as Lat	same name as meridian angle

Notes: – HPV represents the altitude of the celestial body in the Prime Vertical, computed using the following formula:

$$sinH_{PV} = sin\ Dec \cdot cosecLat \quad (16)$$

To convert the zenith angle (Z) into azimuth (Zn), the following conversion table (Table 5) must be used:

Table 5. Conversion of zenith angle to azimuth

Z	Zn
Z = NE ... °	Zn = Z
Z = SE ... °	Zn = 180° – Z
Z = SW ... °	Zn = 180° + Z
Z = NW ... °	Zn = 360° – Z

Altitude reduction (Tables 6 and 7):

Journal of Marine Technology and Environment
DOI:10.53464/JMTE.02.2026.01
ISSN (Print): 1844-6116
ISSN (Online): 2501-8795
https://www.jmte.eu

Table 6. Altitude reduction – variant 1

LI2	1237.9	Zn	206°.1		
LI1	1234.5	C	105°.0		
Diff.	3.4	(Zn-C)	101°.1		
x f	1.0			a1	+4'.7
Dist	3.4	cos (Zn-C)	x (-0.192521)	ΔH	-0'.7
				a'1	+4'.0

Variant:

Table 7. Altitude reduction – variant 2

S/60	16/60	0.26 x	Zn	206°.1		
CT2	19h58m59s		C	105°.0		
CT1	19h46m23s		(Zn-C)	101°.1		
CT2 - CT1	00h12m36s	13m x			a1	+4.7
cos (Zn-C)	cos 101°.1	-0.192521 =			ΔH	-0.7
ΔH		-0.7			a'1	+4'.0

$$LOP1\begin{cases}Zn1 = 206°,1\\ a'1 = +4',0\end{cases}$$

3.2 LOP 2 – Arcturus

Computed altitude (Hc) and intercept (a) computation.

Used formula:

$$Hc = \underbrace{sinLat * sinDec}_{\text{Part a}} + \underbrace{cosLat * cosDec * t}_{\text{Part b}} \quad (17)$$

Table 8. Altitude computation (Hc) – Arcturus

E Lat	38°12.0' N	sin Lat	0.618408395	cos Lat	0.785856893
Dec	N19°04.5'	sin Dec	0.326805556	cos Dec	0.945091598
tE	022°04.1' E			cos t	0.926736424
Ho	62°57.7'	part a	0.202099300	part b	0.688293395
Hc	62°55.4'	part b	0.688293395		
Intercept (a2)	+ 2.3'	sin Hc	0.890392694		
		Hc	62°55.4'		

Zenith angle (Z) and azimuth (Z_n) computation.

The zenith angle given by this formula has a quadrantal size (Table 9).

Used formulas:

$$sinZ = sin\ t \cdot secH_c \cdot cosDec \quad (18)$$

$$sinH_{PV} = sin\ Dec \cdot cosecLat \quad (19)$$

Table 9. Zenith angle value computation – Arcturus

tE	22°04.1' E	sin t	0.375712125	HPV	
Hc	62°55.4'	sec Hc	2.196869369	sin Dec	0.326805556
Dec	N19°04.5'	cos Dec	0.945091598	cosec Lat	1.617054373
Lat	38°12' N	sin Z	0.780069587	sin HPV	0.528462354
HPV	N45°21.5'	Z	51°16.0'	HPV	31°54.1'
Dec same name as Lat		Z	51°.3	180°	179°.10
Dec < Lat	Hc > HPV	Z	SE 51°.3	Z	-51°.3
				Zn	128°.7

The following table helps to establish the quadrant of the horizon in which the body is sighted (Table 10).

$$LOP2\begin{cases}Zn2 = 128°,7\\ a2 = +2',3\end{cases} Fix\begin{cases}Lat = 38°07,1'N\\ Lon = 40°50,1'W\end{cases}$$

DOI:10.53464/JMTE.02.2026.01
ISSN (Print): 1844-6116
ISSN (Online): 2501-8795
https://www. jmte.eu

The application of the same-altitude method in this context demonstrates both the theoretical robustness and practical utility of classical celestial navigation. Beyond its practical maritime application, the method also echoes a longstanding cultural and religious tradition: the use of celestial bodies to structure human activity.

Both systems – celestial navigation and Islamic prayer timing – demonstrate a profound continuity between observational astronomy and human practice, bridging scientific technique and spiritual rhythm.

They reflect an enduring human inclination to look to the sky not only for spatial orientation but also for temporal structure and metaphysical meaning.

Thus, the same-altitude method serves not only as a precise navigational tool, but also as a reminder of the deep cultural significance embedded in our observation of the cosmos.

Table 10. Quadrant establishment

Name of Dec	**Magnitude of Dec**	**Size of Hc**	**Origin (1st letter)**	**Direction (2nd letter)**
1	2	3	4	5
contrary to Lat	-	-	contrary to Lat	same name as meridian angle
same name as Lat	Dec < Lat	Hc > HPV	contrary to Lat	same name as meridian angle
same name as Lat	Dec < Lat	Hc < HPV	same name as Lat	same name as meridian angle
same name as Lat	Dec > Lat	-	same name as Lat	same name as meridian angle

Journal of Marine Technology and Environment
DOI:10.53464/JMTE.02.2026.01
ISSN (Print): 1844-6116
ISSN (Online): 2501-8795
https://www.jmte.eu

4. CONCLUSIONS

This research highlights several important findings. Firstly, it emphasises that there are numerous connections between science and religion. While these domains are often seen as distinct or even conflicting, this study suggests they are not necessarily parallel or mutually exclusive; instead, science and religion can coexist and complement each other, especially when addressing various aspects of human life.

A key focus of the paper is the strong relationship between nautical astronomy and Islam. The research demonstrates how astronomical knowledge can be practically applied to support Muslim seafarers in observing their daily prayer rituals while at sea.In situations where internet access is unavailable, seafarers must rely on traditional navigational tools – such as the sextant and chronometer – as well as nautical almanacs and calculation tables. These instruments and resources enable them to accurately determine prayer times, thereby maintaining their religious duties even in isolated maritime regions. Ultimately, this study may serve as a valuable guide for Muslim seafarers, offering practical methods to uphold their religious practices throughout their voyages.

5. ACKNOWLEDGMENTS

Not applicable.

6. CREDIT AUTHOR STATEMENT

Conceptualization: F. M., A. B.; Data curation: A.B., F.M.; Formal analysis: F. M., A. B.; Funding acquisition: A.B., F.M.; Investigation: F. M., A. B.;. Methodology: A.B., F.M.; Project administration: F. M., A. B.; Resources: F. M., A. B.; .Supervision: F.M.; Validation: A.B.; Visualization: A.B., F.M.; Writing – original draft: A.B., F.M.; Writing – review & editing: A.B., F.M.

7. REFERENCES

[1] Quran [20:14].

[2] Norie's Nautical Tables, Revised Edition, 2018 (St Ives: Imray).

[3] Bowditch, N., 2020, The American Practical Navigator (Springfield: National Geospatial-Intelligence Agency).

[4] Brown's Nautical Almanac 2020, Brown, Son & Ferguson (Glasgow: Brown, Son & Ferguson Ltd.).

[5] Burch, D., 2015, Celestial Navigation: A Complete Home Study Course (Seattle: Starpath Publications).

[6] Cunliffe, T., 2020, Celestial Navigation (Chichester: Fernhurst Books Ltd.).

[7] Karl, J., 2007, Celestial Navigation in the GPS Age (Arcata: Paradise Cay Publications).

[8] Bartlett, M., 2009, RYA Astro Navigation Handbook (Hamble: Royal Yachting Association).

[9] Meeus, J., 1998, Astronomical Algorithms (Richmond: Willmann-Bell, Inc.).

[10] Read, W.T., 2022, Navigation and Nautical Astronomy (Charleston: Legare Street Press).

[11] Stebbing, F.C., 2022, Navigation and Nautical Astronomy (Charleston: Legare Street Press).

[12] Pontifical Council for the Pastoral Care of Migrants and Itinerant People, https://www.vatican.va/roman_curia/pontifical_councils/migrants/pom2006_101-suppl/rc_pc_migrants_pom101-suppl_apostl-rodriguez.html

[13] Kurteva Galina, *Management of investment risk of economic operators in the BLACK SEA region*, Journal of Marine Technology and Environment, vol. 2, pp 61-64, 2015.

[14] Toneva-Zheynova D., Mednikarov B., Nikolova N., Tenekedjiev K., *Environmental impact of transport and tendencies for development of sustainable transport in BULGARIA*, Journal of Marine Technology and Environment, vol. 1, pp 143-150, 2011.

DOI:10.53464/JMTE.02.2026.01

ISSN (Print): 1844-6116
ISSN (Online): 2501-8795
https://www. jmte.eu

Journal of Marine Technology and Environment
DOI:10.53464/JMTE.02.2026.02
ISSN (Print): 1844-6116
ISSN (Online): 2501-8795
https://www. jmte.eu

COMPUTATIONAL ANALYSIS OF PARAMETRIC ROLL IN SHIPS: FROM MATHIEU TONGUES TO ATTRACTION BASINS

Dumitru DELEANU [1] & Simona-Ana SÎRBU [2,3]

[1] Constanta Maritime University, Faculty of Marine Engineering, 104 Mircea cel Batran Street, 900663, Constanta, Romania, e-mail address: dumitrudeleanu@yahoo.com
[2] Constanta Maritime University, Faculty of Marine Engineering, 104 Mircea cel Batran Street, 900663, Constanta, Romania, ORCID ID 0009-0006-0071-8874, e-mail address: simona.sirbu@cmu-edu.eu
[3] National University of Science and Technology Politehnica Bucharest, Doctoral School of Entrepreneurship, Engineering and Business Management, 313 Splaiul Independentei Street, 060042, Bucharest, Romania

Abstract: Parametric roll is a nonlinear ship-motion instability triggered when the encounter frequency approaches twice the natural roll frequency, causing periodic modulation of restoring moment and possible amplification to large roll angles. This paper develops and exploits a compact, one-degree-of-freedom roll model to numerically detect the principal nonlinear phenomena associated with parametric roll in a modern containership. The model combines a fifth-order polynomial restoring lever, a composite damping with linear, quadratic, cubic and smoothed Coulomb terms, and a parametric modulation of the linear restoring. Starting from the dimensionless parametric roll equation, three diagnostic products are obtained: (i) Ince-Strutt diagram showing the main Mathieu tongue; (ii) basins of attraction that quantify sensitivity to initial conditions and "escape" to extremely large roll angles; (iii) frequency-response curves that expose jumps and hysteresis loops. From an operational point of view, the diagrams show where amplification of roll motion is likely, the basins identify which perturbations lead the ship into a dangerous situation, and the frequency-response/hysteresis curves indicate how transitions occur and how persistent they are. Such tools can guide both ship design as well as the decisions needed during navigation (speeds/courses that avoid critical encounter bands). To make numerical simulation more applicable, we calibrate the model parameters to a representative containership.
Key words: Attraction basin, Instability tongue, Ship parametric rolling.

1. INTRODUCTION

Parametric roll is a nonlinear instability that can drive large roll angles in otherwise modest sea conditions. It arises when the ship's restoring characteristics vary periodically with the encounter of waves, most often in head or following seas, so that the roll dynamics experience an effective parametric excitation near twice the natural roll frequency.

Under such conditions, even small external perturbations can be amplified cycle by cycle, producing sudden growth, large steady oscillations, or strongly modulated responses that challenge the vessel's operational limits.

Despite the fact that this phenomenon has been studied for decades using Mathieu-Hill-Duffing models, there remains a practical need for numerical tools and maps that make the onset and saturation of parametric roll readily identifiable for concrete ship classes and operating points [1 – 2, 5 - 9].

The present paper adopts a numerical-centric perspective to systematically explore interesting nonlinear phenomena associated with parametric roll in ships. Using a compact parametric rolling model in which the parameter values are representative of a classical containership, we focused on three clear and reproducible geometric tools: the main Mathieu tongue, basins of attraction, and frequency-response curves. All simulations employ transient and stationary windows where the peak roll amplitudes are measured.

Escape criteria are defined by angle thresholds motivated by operational practice.

This protocol enables like-for-like comparison across different parameter values.

In future research, we will replace the polynomial restoring moment approximation with tabulated hydrostatic data and the idealized sinusoidal sea forcing with stochastic sea-state excitation to achieve a more realistic representation of the parametric roll phenomenon.

Journal of Marine Technology and Environment
DOI:10.53464/JMTE.02.2026.02
ISSN (Print): 1844-6116
ISSN (Online): 2501-8795
https://www.jmte.eu

2. NONLINEAR PARAMETRIC ROLL EQUATION

We denote the roll angle by $\phi(t)$, with $\dot{\phi}$ and $\ddot{\phi}$ its time derivatives. The nonlinear equation of parametric roll in general form reads:
where:

$$I_{eff}(\phi) \cdot \ddot{\phi} + D(\dot{\phi}) + R(\phi, t) = 0 \qquad (1)$$

- $I_{eff}(\phi) = I_\phi + \delta I_\phi + A\phi^2$ is the effective moment of inertia about the roll axis. Here, I_ϕ is the ship moment of inertia, δI_ϕ the moment of inertia of the added mass of surrounding water, and $A\phi^2$ is weakly amplitude-dependent (it is optional and set to zero in the core results).
- $D(\dot{\phi}) = D_1\dot{\phi} + D_2|\dot{\phi}|\dot{\phi} + D_3\dot{\phi}^3 + D_C\, sgn(\dot{\phi})$ is the nonlinear composite damping moment. D_1, D_2, and D_3 are constants that capture linear, quadratic, and cubic viscous effects, while $D_C\, sgn(\dot{\phi})$ is a smoothed Coulomb term that regularizes dry friction near $\dot{\phi} = 0$. For numerical reasons, it is replaced by $D_C\, tanh(\dot{\phi}/\varepsilon)$, with $\varepsilon \ll 1$.
- $R(\phi, t) = \rho g \nabla [GZ_{stat}(\phi) + GZ_{par}(\phi, t)]$ represents the restoring moment. Here, ρ is the water density, g the gravitational acceleration, ∇ the mass displacement, $GZ_{stat}(\phi)$ the static lever, and $GZ_{par}(\phi, t)$ the contribution of the parametric excitation. The static lever can be approximated by an odd polynomial $GZ_{stat}(\phi) = K_1\phi + K_3\phi^3 + K_5\phi^5$, where $K_1 \approx GM_m$ (constant part of metacentric height), $K_3 < 0$ and $K_5 > 0$ capture softening and saturation, respectively. The periodic variation of the restoring moment induced by longitudinal waves mainly affects the linear part, $GZ_{par}(\phi, t) = (GM_a\, cos\omega_e t) \cdot \phi$, where ω_e denotes the wave encounter frequency and GM_a is the variable part of the metacentric height.

Remark: Some external and bias moments can be introduced in (1). External forcing arises from the small direct roll excitation caused by asymmetry and by diffracted waves. Bias moments can be associated with a constant heel due to wind or cargo shift. Although these moments do not cause instability, they can trigger or amplify it (especially by shifting the equilibrium to an angle $\phi \neq 0$) [3, 4].

The small-angle ship's natural frequency, ω_ϕ, is provided by:

$$\omega_\phi = \sqrt{\frac{\rho g \nabla GM_m}{I_\phi + \delta I_\phi}}$$

Let $\tau = \omega_\phi t$, $x(\tau) = \phi(t)$, $(\cdot)' = d(\cdot)/d\tau$. Dividing (1) by I_{eff} and noting that $d/dt = \omega_\phi d/d\tau$ and $d^2/dt^2 = \omega_\phi^2 d^2/d\tau^2$, yields the nondimensional form of the parametric roll equation:

$$x'' + d_1 x' + d_2|x'|x' + d_3(x')^3 + d_C\, tan(x'/\tilde{\varepsilon}) + \qquad (2)$$
$$+[1 + \mu\, cos(\sigma\tau)]x + k_3x^3 + k_5x^5 = 0$$

where the dimensionless coefficients are:

$$d_1 = \frac{D_1}{(I_\phi + \delta I_\phi)\omega_\phi}, d_2 = \frac{D_2}{I_\phi + \delta I_\phi}, d_3 = \frac{D_3\omega_\phi}{I_\phi + \delta I_\phi},$$

$$d_C = \frac{D_C}{(I_\phi + \delta I_\phi)\omega_\phi^2}, \tilde{\varepsilon} = \frac{\varepsilon}{\omega_\phi}, \mu = \frac{GM_a}{GM_m}, \sigma = \frac{\omega_e}{2\omega_\phi},$$

$$k_3 = \frac{K_3 \cdot \rho g \nabla}{(I_\phi + \delta I_\phi)\omega_\phi^2}, k_5 = \frac{K_5 \cdot \rho g \nabla}{(I_\phi + \delta I_\phi)\omega_\phi^2} \qquad (3)$$

This nondimensionalization makes explicit that the linear restoring scales as unity, the static nonlinearity is governed by (k_3, k_5), and the parametric excitation enters as $\mu\, cos(\sigma\tau)$.

3. VESSEL-SCALE PARAMETRIZATION

We adopt a coherent parametric set representative of a modern ~8000 TEU container ship. These values are used throughout unless stated otherwise (see Table 1).

Table 1. The containership dimensional parameters

Parameter	Value	Unit
I_ϕ	$1.4014 \cdot 10^{10}$	$kg \cdot m^2$
δI_ϕ	$2.17 \cdot 10^9$	$kg \cdot m^2$
D_1	$3.5393 \cdot 10^8$	$kg \cdot m^2/s$
D_2	$1.8826 \cdot 10^8$	$kg \cdot m^2$
D_3	$1.1232 \cdot 10^8$	$kg \cdot m^2 \cdot s$
D_C	$7.4361 \cdot 10^5$	$kg \cdot m^2/s^2$
ε	0.002	$1/s$
ρ	1000	kg/m^3
∇	76468	m^3
$K_1 \approx GM_m$	1.91	m
K_3	−3.96	m
K_5	2.64	m

Journal of Marine Technology and Environment
DOI:10.53464/JMTE.02.2026.02
ISSN (Print): 1844-6116
ISSN (Online): 2501-8795
https://www.jmte.eu

With these values, one has $\omega_\phi = 0.2975\, rad/s$, and $T_\phi = 2\pi/\omega_\phi = 21.12\ s$. Additionally, from (3), the following no dimensional parameters are obtained:

$$d_1 = 0.0736, d_2 = 0.0116, d_3 = 0.0021, d_C = 0.0005,$$

$$\tilde{\varepsilon} = 0.0067, k_3 = -2.0763, k_5 = 1.3842.$$

4. NUMERICAL SIMULATIONS

In every simulation, we integrated the non-dimensional roll equation (2) with an explicit, adaptive Runge-Kutta method using relative and absolute tolerances of 10^{-6} and 10^{-8}. The maximum internal step size was $\Delta\tau_{max} = 0.05$. The running time was split into two equal intervals representing transitory and stationary windows. Unless otherwise stated, the initial conditions correspond to a small perturbation, $\phi(0) = 0.2^0, \dot{\phi}(0) = 0$.

4.1 Single-case dynamics

We first simulated the ship's behaviour in the vicinity of the resonance condition $\omega_e \approx 2\omega_\phi$ to determine the rate of increase of the initial disturbance $\phi(0)$. Figure 1a presents the time histories of ship roll angle for $\omega_e = 0.6055$ (meaning σ = 1.0193 and μ = 0.4) and GM_a = 0.764. An exponential increase in roll oscillations is evident. With a running time of 800 s, the values 23.4° and 19.8° were found for the amplitudes of the transient and stationary phases, respectively. A not-very-consistent "departure" from the theoretical resonance point has the opposite effect. The initial perturbation, even of the order of a few degrees, is "annihilated" by the ship's damping (see Fig. 1b, obtained for σ = 1.076 and ϕ (0) = 2°).

Between the two situations described above, a transition process occurs in which the dangerous roll oscillations develop increasingly more slowly. Thus, for σ = 1.055, at 800 s after the oscillation's initiation, the ϕ angle was only 2°. It reached the maximum value of 14° for t ~1100 s and stabilized at 12.5° (see Fig. 1c).

Similar to chaotic dynamical systems, the initial conditions can play a decisive role in the ship's final response. For example, by choosing σ = 1.0796 and $\phi(0)$ = 1.8508703°, the ship is subjected to a minor rolling of 0.87° for no less than 4000 s, after which a jump occurs to another permanent state characterized by a moderate rolling of 6.5° (see Fig. 1d). Just an infinitesimal shift to ϕ (0) = 1.8598702°, results in a long period with ϕ max = 0.9° followed by a decay to 0°.

In conclusion, two parameters that require great attention when issuing a judgment are the tracking time of the ship's behavior and the starting conditions.

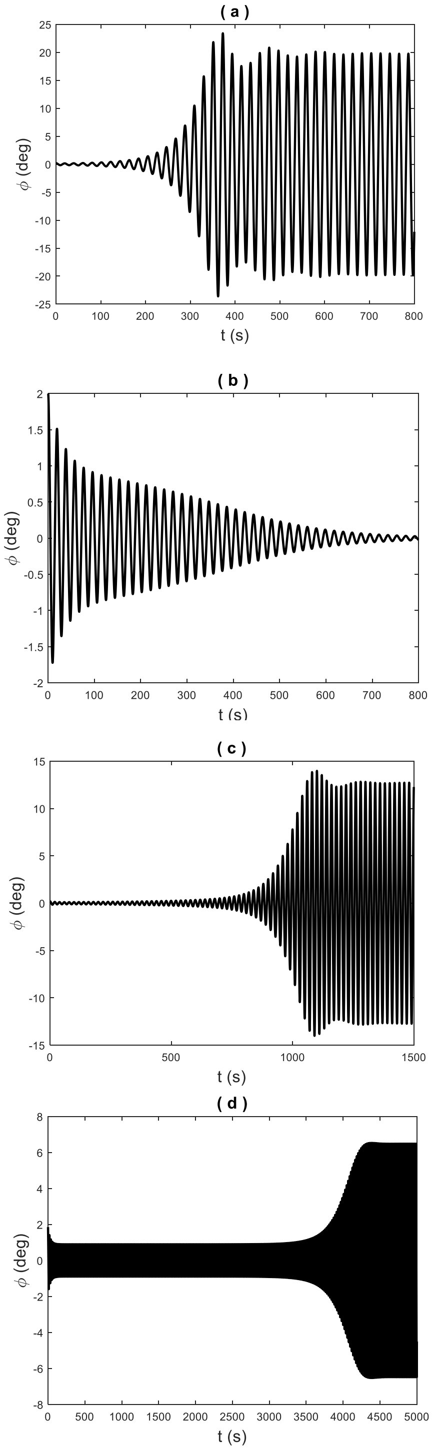

Figure 1 Time histories of ship roll angle

where:
(a) σ = 1.0193, ϕ (0) =0. 2°; (b) σ = 1.076, ϕ (0) = 2°; (c) σ = 1.055, ϕ (0) =0. 2°; (d) σ = 1.0796, ϕ (0) =1.8508703°.

4.2 The principal Mathieu's tongue

Journal of Marine Technology and Environment
DOI:10.53464/JMTE.02.2026.02
ISSN (Print): 1844-6116
ISSN (Online): 2501-8795
https://www. jmte.eu

As expected from Mathieu-type theory, there exists a single dominant V–shaped tongue with a rounded tip centred near σ = 1 in the (σ, μ) plane. It corresponds to the combinations (σ, μ) of parameters associated with the longitudinal waves for which the small initial perturbation is abruptly amplified.

To represent it, we scan over a rectangular grid with 101 × 101 uniformly distributed points. For each pair (σ, μ), we recorded the peak amplitude $A_{max} = max|\phi(t)|$ in the stationary stage and amplitude class. The latter could be 1 if $A_{max} \le 2°$, 2 if $2° < A_{max} \le 10°$, 3 if $10° < A_{max} \le 20°$, 4 if $20° < A_{max} \le 30°$, and 5 otherwise. Figures 2 to 4 report our findings for running times in the ranges [0, 400] s, [400, 800] s, and [1500, 3000] s. A first remark is easy to intuit from the analysis of these figures. A sufficiently long observation is needed for the full formation of the instability tongue and the separation into amplitude classes within it.

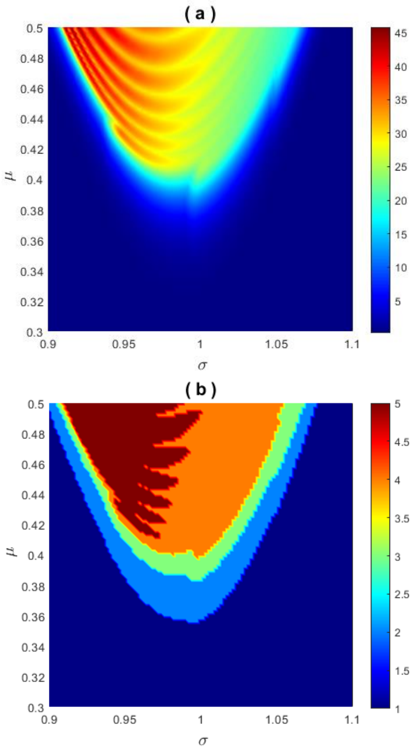

Figure 2 The main instability tongue case I.

The colour bar shows the peak roll amplitude (a) or amplitude class (b).

The running dimensional time *t* was in the range [0, 400] s.

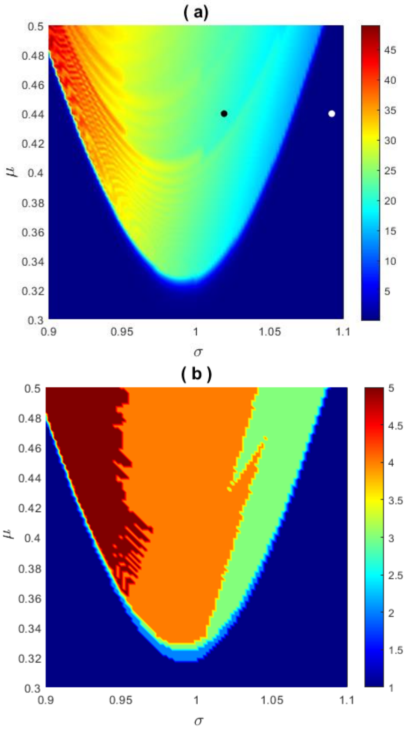

Figure 3 The main instability tongue-case II .

The same as in Fig. 2, but the running time was in the range [400, 800] s.

The black and white points correspond to the time series presented in Figs. 1a, b.

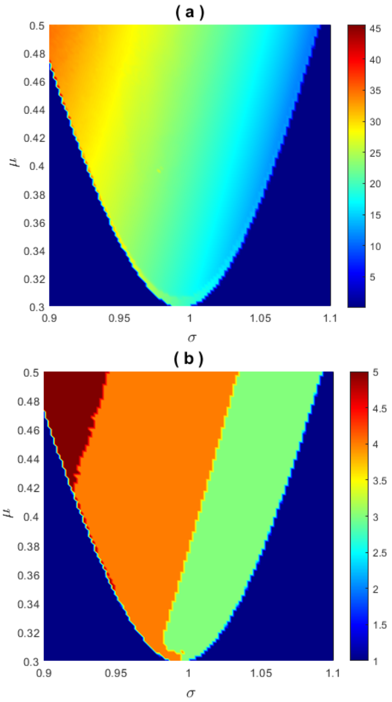

Figure 4 The main instability tongue-case III

Journal of Marine Technology and Environment
DOI:10.53464/JMTE.02.2026.02
ISSN (Print): 1844-6116
ISSN (Online): 2501-8795
https://www.jmte.eu

The same as in Fig. 2, but the running time was in the range [1500, 3000] s.

This division into classes is extremely pronounced, with amplitudes that increase as σ decreases and μ increases. If the (σ, μ) point falls inside the colored tongue, a parametric amplification of the roll angle to a saturated level is expected. Conversely, if the (σ, μ) point lies outside the tongue, any initial perturbation should decay to zero or to very small oscillations. Near the tongue's tip and on its left side, jump phenomena and path dependence are expected. Local grid refinement in these areas reveals fine structures in which large-amplitude branches coexist with moderate-amplitude branches (see Fig. 5).

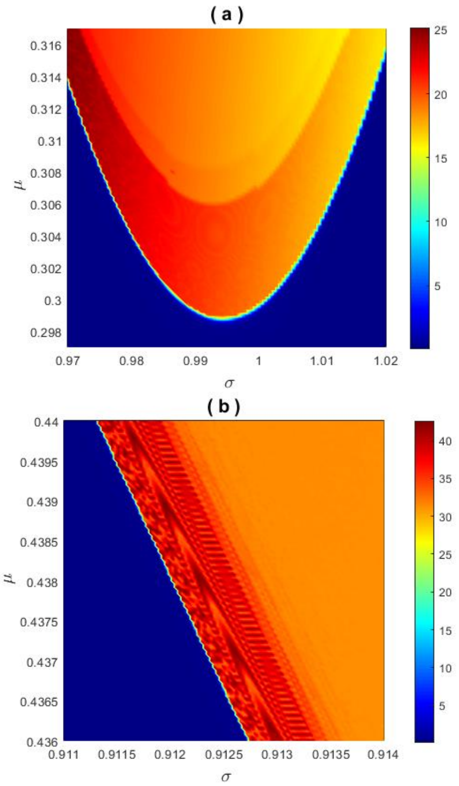

Figure 5 Extracts from Fig. 4a that highlight either jump phenomena or coexistence of different amplitude classes in an extremely small region

We have already highlighted the importance of choosing a sufficiently long observation (running) time to minimize decision-making errors. In addition, Figure 6 shows the variation in the percentages of the five amplitude classes as a function of running time in the two collection windows: the transient and the stationary. We can see that 3000 – 4000 seconds are necessary and sufficient for stabilization. For this reason, the following simulations will use a time that balances efficiency and the correctness of the conclusions: T_{run} = 3000 s.

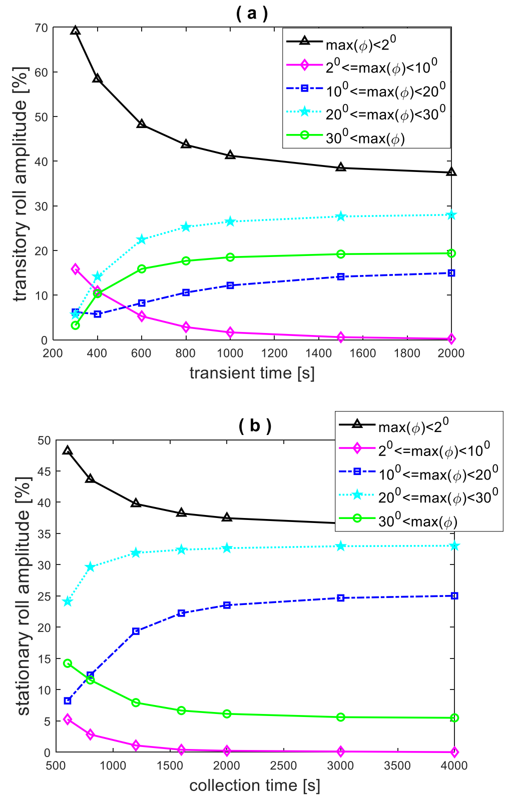

Figure 6 The dependence of the percentage of each amplitude class on running time in (a) transitory window; (b) stationary window

Up to this point we have used the values set in Section 3 for the system's parameters. Let us now identify the effects of changing the most important of them.

As the small-amplitude damping coefficient d_1 is raised, the tip of Mathieu's tongue moves toward higher μ. Therefore, in the previously used domain (σ, μ) a significant increase in the percentage of amplitude class 1 and a decrease of classes 3, 4 and 5 is observed (see Fig. 7a). In addition to the decrease in the steady state amplitude, there is also a delay in the development of the parametric roll, which allows the crew to take the necessary measures (see Fig. 7b). Increasing the nonlinear damping coefficients d_2 and d_3 reduces slightly the saturated amplitude without substantially altering the initial onset.

Journal of Marine
Technology and Environment
DOI:10.53464/JMTE.02.2026.02

ISSN (Print): 1844-6116
ISSN (Online): 2501-8795
https://www. jmte.eu

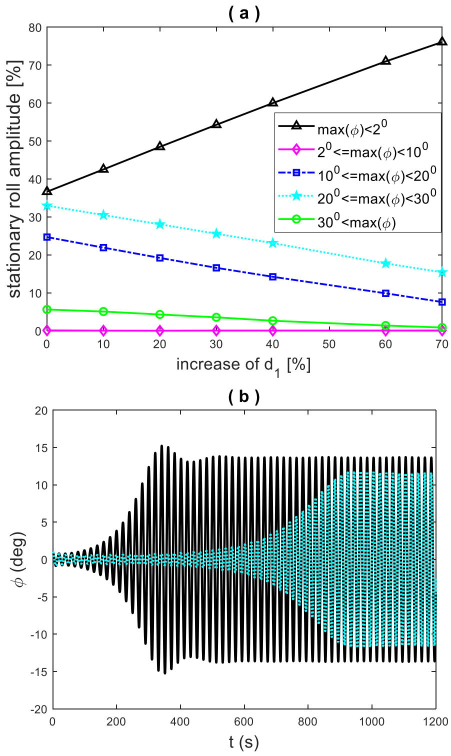

Figure 7 (a) Effect of increasing damping coefficient d_1 on the steady state amplitude;
(b) Time histories of roll angle for $\mu = 0.4$, $\sigma = 1.05$, $\varphi(0) = 1°$ and $d_1 = 0.0736$ (black) or $d_1 = 0.1104$ (green)

An increase in the softening coefficient k_3 does not change the position of the instability zone in the (σ, μ) plane, but within Mathieu tongue a beneficial shift occurs from amplitude classes 4 and 5 to class 3 (see Fig. 8a). At least for the combination of parameters chosen in the paper, a modification of k_5 does not seem to influence significantly the weights of the amplitude classes (see Fig. 8b).

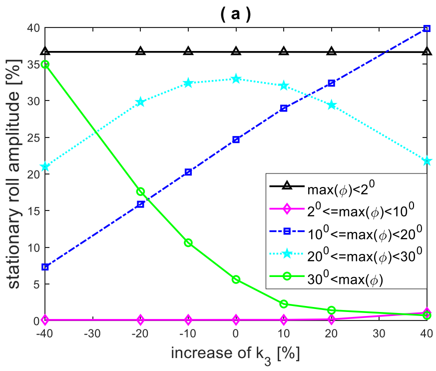

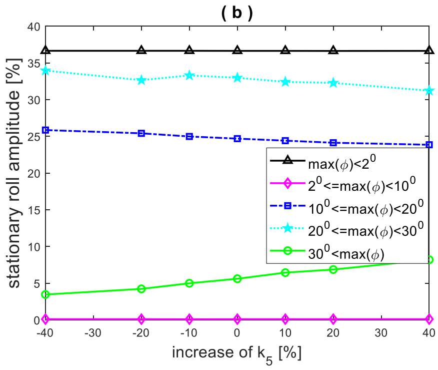

Figure 8 Influence of restoring nonlinearities on the stationary roll amplitudes

We suggested in Fig. 1d a possible factor with a major effect on the ship's response to rolling: the initial conditions. If a small disturbance is more easily attenuated by the ship's damping, it is possible that more severe initial conditions will help the development of parametric roll in a much shorter time and at a significantly reduced wave height (decreased μ). Indeed, compared with Fig. 4b, the two panels of Fig. 9 show a minor reconfiguration within the instability zone, but a shift of the tip toward much lower values of μ (which is undesirable).

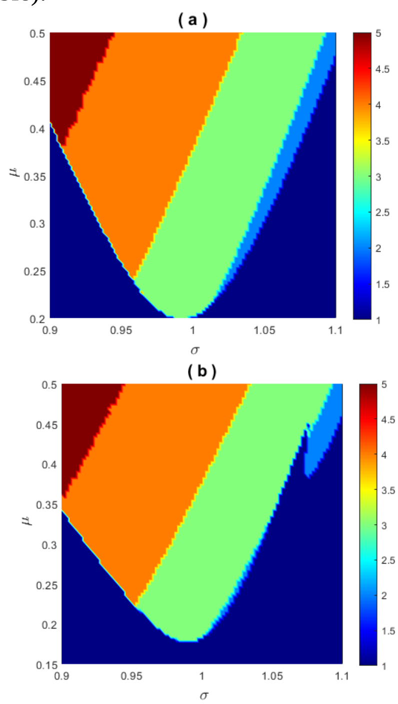

Figure 9 Shifting effect of the initial conditions on the Mathieu tongue

(a) $\varphi(0) = 2°$, $d\varphi/dt(0) = 0$;
(b) $\varphi(0) = 5°$, $d\varphi/dt(0) = 1°/s$

4.3 Basins of attraction

Journal of Marine Technology and Environment
DOI:10.53464/JMTE.02.2026.02
ISSN (Print): 1844-6116
ISSN (Online): 2501-8795
https://www.jmte.eu

Attractor basins are computed in the ($\phi(0)$, dϕ/dt (0)) plane by integrating the roll equation (2) from a Cartesian grid of 101 x 101 initial states over a running time T = 3000. Each trajectory is assigned an amplitude class, as described in the previous section.

For the container ship parametrization presented in Section 3, near the principal resonance σ = 1 and moderate modulation μ, the basin portrait exhibits a safe neighbourhood around the origin $\left(\phi(0) = 0, \dot{\phi}(0) = 0\right)$ where curved bands associated with amplitude classes 1 and 2 intertwine in a seemingly complicated way. Somewhere farther from the origin (a few-degree zone), two or more thin lobes of large response, roughly aligned with the vertical axis, can be observed. A local focus on the boundary between low- and high-amplitude classes reveals a fringed boundary with very thin bands of medium amplitude. For large $\phi(0)$, escape pockets at the corners of the analyzed domain can be detected (see Fig. 10a). With the increase of μ, this picture changes substantially in the sense that small classes disappear and are replaced on an increasingly larger area of the ($\phi(0)$, μ) plane by zones that pose a major risk for ship safety (see Fig. 10b). Far from resonance, we might think that for a fixed μ the small amplitude classes expand and the others retreat. This is true for μ > 1 (see Fig. 10d) but not otherwise. Looking again at Fig. 4b, we can understand that the area of high amplitudes is concentrated to the left of the typical value σ = 1. Here, taking into account the initial disturbances, we can only expect high-amplitude classes (see Fig. 10c).

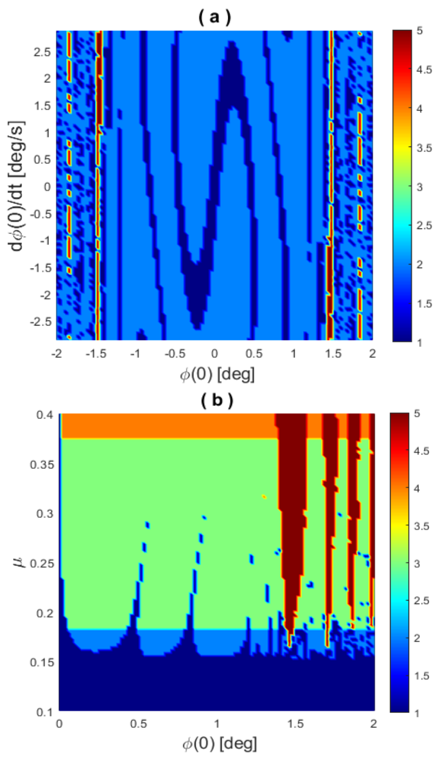

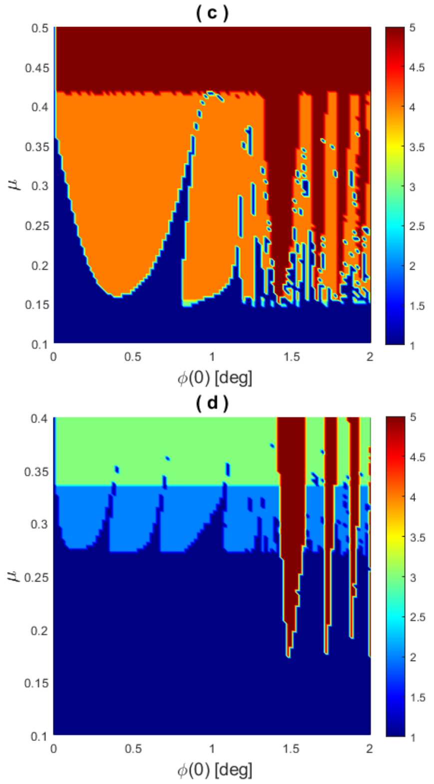

Figure 10 Basins of attraction for different amplitude classes

where
(a) for σ = 1 and μ = 0.178;
(b) Sensitivity of amplitude classes on φ (0) and μ for σ = 1;
(c) The same but for σ = 0.92 (c) or σ = 1.05 (d).

Regarding the influence of the main parameters on the basin's geometry, we can summarize the following:

- Increasing d_1 expands the small-amplitude basin and decreases the others slowly. The large-amplitude lobes are pushed outward. This tendency is strongest near σ = 1 and moderate μ (see Figs. 11a and 12a).
- Stronger k_3 enlarges small amplitudes basins in the (φ (0), μ) plane but introduces a lot of very fringed zones of large amplitude for φ (0) > 1° or μ > 0.35 (see Fig. 12b). For fixed μ and σ = 1, the ship's situation is better because a transfer from amplitude class 3 to class 2 is observed (see Fig. 11b).

Journal of Marine Technology and Environment
DOI:10.53464/JMTE.02.2026.02
ISSN (Print): 1844-6116
ISSN (Online): 2501-8795
https://www. jmte.eu

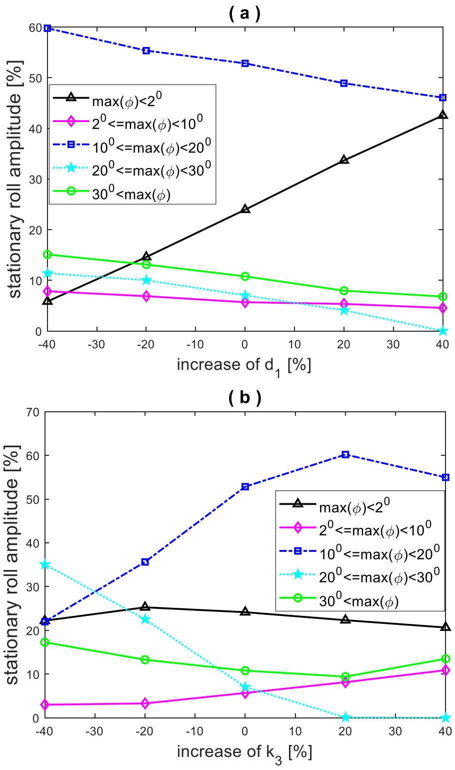

Figure 11 The dependence of the attraction basin of each amplitude class of (a) d_1; (b) k_3

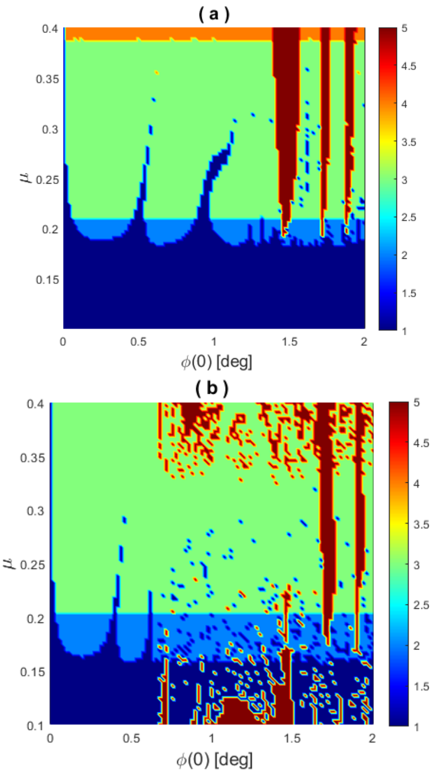

Figure 12 The dependence of amplitude classes on φ (0) and μ for σ = 1:

(a) an increase of d_1 by 20%; (b) an increase of k_3 by 40%

4.4 Frequency – response curves

These curves present the steady peak amplitude as a function of frequency ratio σ for a given set of vessel parameters. Unlike the synchronous roll, where these curves have the shape of Ω letter, with the upper part more or less pointed and inclined to one side, in this case their appearance is trapezoidal (see Fig. 13a). For a fixed modulation depth μ, the damping manages to “extinguish” the initial disturbance except for an interval $[\sigma_{min}, \sigma_{max}]$ approximately centred on σ = 1 at the ends of which a jump up and down in the value of oscillation amplitude occurs. The length of this interval increases with μ, as does the roll amplitude. Of interest are the sharp peaks at the ends of the interval, which indicate major transformations in the ship’s behaviour resulting from small changes in wave encounter frequency or the ship's natural roll frequency. The same type of response is obtained by tightening the initial conditions for a fixed μ, with the observation that, in the interval of non-zero amplitude, the curves are superimposed (see Fig. 13b).

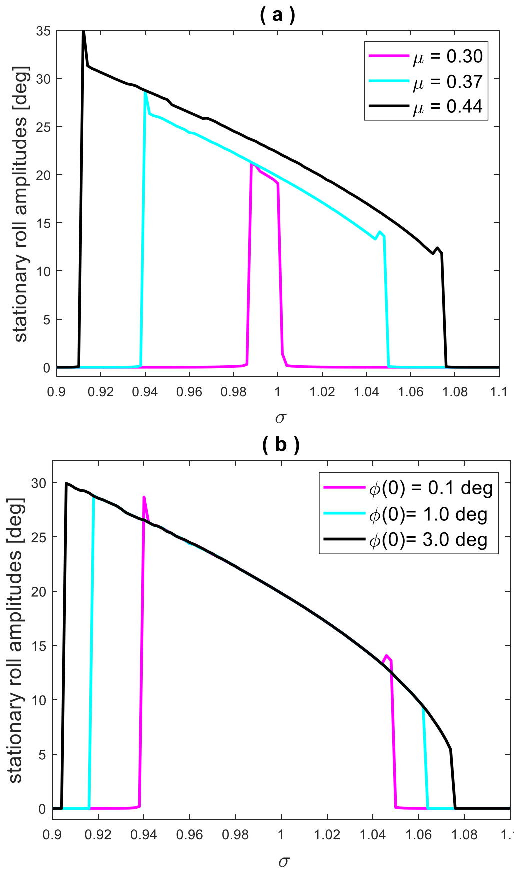

Figure 13 Frequency – response curves for (a) three different μ; (b) three different φ (0) and μ = 0.37

Augmenting the linear drag coefficient d_1 has the expected positive effect, namely narrowing the interval

Journal of Marine
Technology and Environment
DOI:10.53464/JMTE.02.2026.02

ISSN (Print): 1844-6116
ISSN (Online): 2501-8795
https://www. jmte.eu

[σ_{min}, σ_{max}] but not the stationary roll amplitude (only to a small extend; see Fig. 14a). Doing the same but for restoring coefficient k_3, we obtained an opposite effect: preserving the dangerous frequency σ range but decreasing the roll amplitudes as k_3 increases (see Fig. 14b). Somehow similar effects are produced by changing other parameters, for example k_5 and d_c (see Figs. 14c, d).

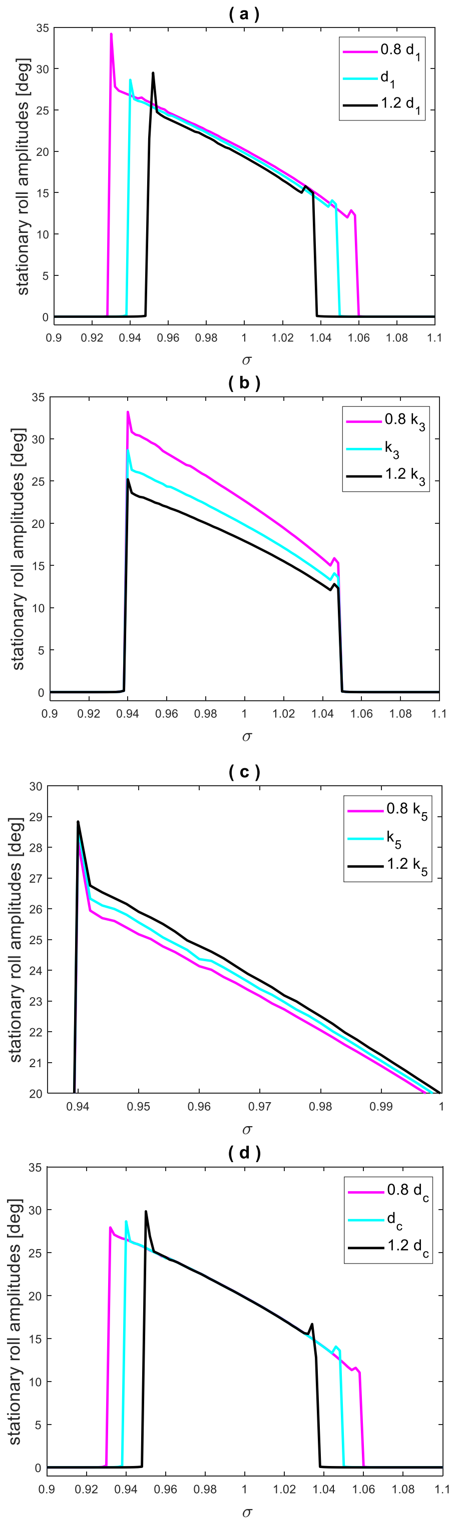

Figure 14 Frequency – response curves for μ = 0.37

and:
(a) Three linear damping coefficients; (b) Three softening restoring coefficients; (c) Three saturation restoring coefficients; (d) Three Coulomb damping coefficients

4.5 Effects of GM_m and frequency detuning

We close this numerical study with a brief presentation of the influence of the constant part of metacentric height, GM_m, on the ship's response. Varying GM_m shifts ω_ϕ and therefore the horizontal placement of the Mathieu tongue when plotted versus σ (for unchanged ω_e). A moderate increase of GM_m generally reduces the likelihood of parametric roll. However, excessively large GM_m does not eliminate parametric instability and may even exacerbate dynamic loads and roll accelerations, merely relocating the resonance rather than suppressing it (see Fig. 15).

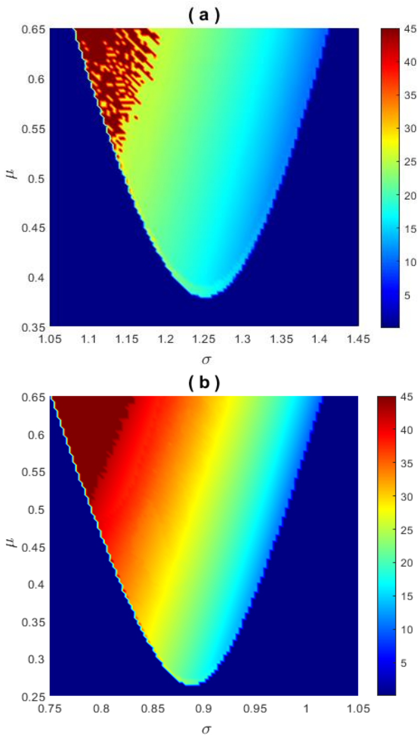

Figure 15 The main Mathieu tongue for (a) GM_m = 1.2; (b) GM_m = 2.4.
The colorbar shows the stationary roll amplitudes

5. CONCLUSIONS

In the paper, we employed a nonlinear Duffing-Mathieu roll oscillator with composite viscous/Coulomb damping and a high-order polynomial restoring lever to

Journal of Marine Technology and Environment
DOI:10.53464/JMTE.02.2026.02
ISSN (Print): 1844-6116
ISSN (Online): 2501-8795
https://www. jmte.eu

obtain clear numerical bifurcation/instability maps, attraction basins, and frequency-response curves for an ~8000 TEU containership. Such maps can guide both ship design (damping devices, GM tuning, etc.) and operations (speed/course choices that affect wave encounter frequency). Limitations of the model (single-degree-of-freedom, polynomial law for GM, sinusoidal sea forcing) are explicit and indicate where the model should be further developed.

Within this scope, we found that:

Onset of parametric roll near the main Mathieu tongue is governed by μ relative to σ, but composite damping and softening shift and shape the instability region;

Basins of attraction expose regions in $\left(\phi(0),\dot{\phi}(0)\right)$ plane where small impulses can trigger large roll amplitudes despite unchanged mean conditions. Additionally, their aspect can be very complicated;

The shape of the frequency-response curves is practically trapezoidal, in obvious contrast to the synchronous roll. The transition from small amplitudes to truly dangerous ones occurs suddenly with small variations of σ and depends on damping components, initial conditions, and modulation depth.

6. CREDIT AUTHORS STATEMENT

Conceptualization: D.D.

Data curation: S-A.S.

Formal analysis: D.D.

Funding acquisition: S-A.S.

Investigation: D.D.

Methodology: D.D.

Project administration: D.D.

Resources: D.D., S-A.S.

Software: D.D., S-A.S.

Supervision: D.D.

Validation: D.D.

Visualization: S-A.S.

Writing – original draft: D.D., S-A.S.

Writing – review & editing: S-A.S..

7. REFERENCES

[1] Azimi M., (2022), Stability and bifurcation of Mathieu-Duffing equation, *Int. J. of Non-linear Mechanics*, vol. 144, DOI 10.1016/j.ijnonlinmec.2022.104049.

[2] Carmel S.M., (2006), Study of parametric rolling event on a Panama container vessel, *Journal of the Transportation Research Board*, vol. 1964, 56 – 63, DOI 10.1177/0361198106196300108.

[3] Deleanu D., Dumitrache C.L., (2019), Numerical study of a container ship model for the uncoupled parametric rolling, *IOP Conf. Ser.: Mater. Sci. Eng.* 591 012106, DOI 10.1088/1757-899X/591/1/012106.

[4] Deleanu D., Dumitrache C.L., (2020), Controlling the parametric roll of a container ship model by changing the forward velocity, *IOP Conf. Ser.: Mater. Sci. Eng.* 916 012024, DOI 10.1088/1757-899X/916/1/012024.

[5] Galeazzi R., Blanke M., Poulsen N.K., (2013), Early detection of parametric roll resonance on containerships, *IEEE Transactions on Control System Technology*, vol. 21(2), 489-503, DOI 10.1109/TCST.2012.2189399.

[6] Ghemari I, Faltinsen O.M., Greco M., (2015), Investigation of parametric resonance in roll for container carrier ships, *Proceedings of the ASME International Conference on Ocean, Offshore and Arctic Engineering*, St. John’s, Newfoundland, Canada, DOI 10.1115/OMAE2015-41528.

[7] Holden Ch., Galeazzi R., Rodriguez C., Perez T., Fossen T.I., Blanke M., Santos Neves M.A., (2007), Nonlinear containership model for the study of parametric roll resonance, *Modelling, Identification and Control*, vol. 28(4), 87-103, DOI 10.4173/mic.2007.4.1.

[8] Kovacic I., Rand R., Sah S.M., (2018), Mathieu’s equation and its generalizations: Overview of the stability charts and their features, *Applied Mechanics Reviews*, vol. 70(2): 020802, DOI:10.1115/1.4039144.

[9] Paulling J.R., (2011), Parametric rolling on ships. Then and now. Contemporary ideas on ship stability and capsizing in waves, *Fluid Mechanics and its Applications*, vol. 97, 253-266, DOI:10.1007/978-94-007-1482-3-19.

Journal of Marine Technology and Environment
DOI:10.53464/JMTE.02.2026.03
ISSN (Print): 1844-6116
ISSN (Online): 2501-8795
https://www. jmte.eu

EXPERIMENTAL STUDY ON ROAD DEFECT DETECTION

Marius-Valentin DUMITRESCU[1], Mariana PANAITESCU [2] & Fanel-Viorel PANAITESCU [2] , Sabina NEDKOVA [3]

[1] PhD Student, National University of Science and Technology POLITEHNICA Bucharest; Doctoral School of Energy Engineering, Romania, e-mail adress: marius_valentin30@yahoo.com
[2] Constanta Maritime University, Faculty of Naval Electro-Mechanics, 104 Mircea cel Batran Street, 900663, Constanta, Romania, 0000-0002-8610-9554, e-mail address:mariana.panaitescu@cmu-edu., 0000-0002-2453-3384, viorel.panaitescu@cmu-edu,
[3] "Assen Zlatarov"University, Burgas, Bulgaria, e-mail address: Sabina_nedkova@abv.bg

Abstract : The main objectives of the study are: exerting pressure on the authorities responsible for road maintenance; increasing the level of civic engagement among citizens; calculating a performance score for companies carrying out infrastructure works; raising the level of trust in public institutions. The proposed solutions are: a) use of the accelerometer to assess road quality and detect potholes, including graphical interpretation; b) pothole detection using a camera; c) dimensional analysis of potholes. The study aims to detect defects in images using two methods:1) the automated YOLOv8 model, where some classes (defectType1, defectType2) have very small bounding boxes, while others (defectType3, defectType4) have large boundaries. Real-time operation is achieved (at least 5 Hz on Jetson Xavier), utilizing the SAHI (Slicing Aided Hyper Inference) technique;2) using an instrumental scanning technique with LiDAR. Data were collected and processed, with the measurements interpreted graphically.

Key words : The infrastructure, defect, detection, LIDAR, SAHI, YOLOv8 model.

1. INTRODUCTION

Road defects can be identified through:

- Visual inspections;
- Non-destructive testing;
- The use of automated equipment.

These methods allow for the identification of visible defects such as cracks, potholes, uneven surfaces, and asphalt layer wear.

Methods used to detect road defects include:

- non-destructive testing that analyses the road's structural integrity without damaging it (ultrasonic testing, thermography);
- instrumental techniques utilizing automated equipment (laser scanning systems, integrated data collection systems).

In the current global context, it has been observed that the "Global country average" reflects the mean result for all countries and markets where the survey on transport quality was conducted. It has not been adjusted for the population size of each country or market and is not intended to suggest an aggregate result."[1] There is considerable variation in satisfaction across the 32 surveyed countries (Fig. 1). [2-4]

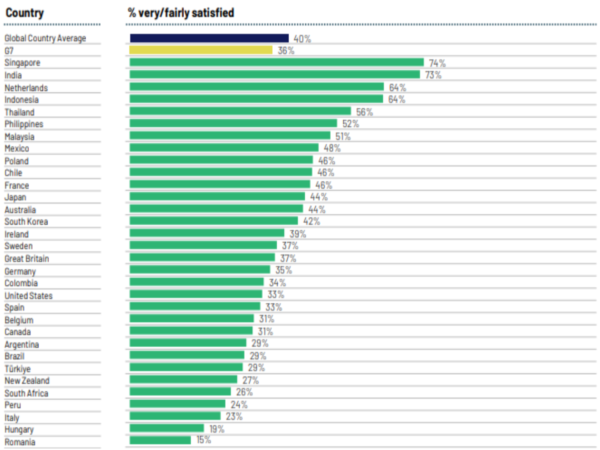

Figure 1 Global infrastructure index as of 2024. [4]

There is variation in how differently the transport sectors are perceived (Fig. 2). [2]:

Journal of Marine Technology and Environment
DOI:10.53464/JMTE.02.2026.03
ISSN (Print): 1844-6116
ISSN (Online): 2501-8795
https://www.jmte.eu

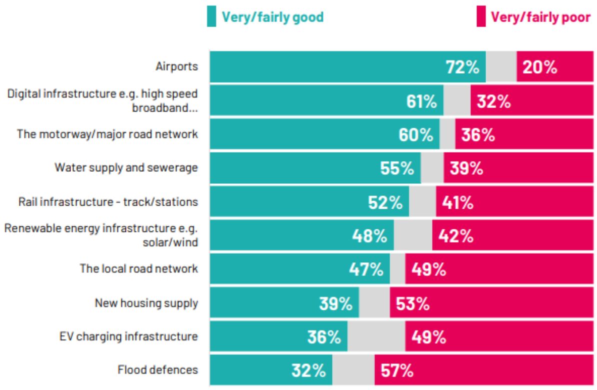

Figure 2 The country's global average [2]

Regarding global statistics, the satisfaction index concerning the mode of transport differs (Fig. 3, Fig. 4)[2].

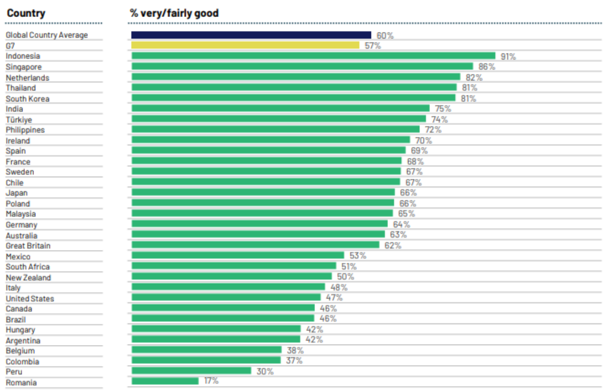

Figure 3 Motorway/major road network assessments. [2]

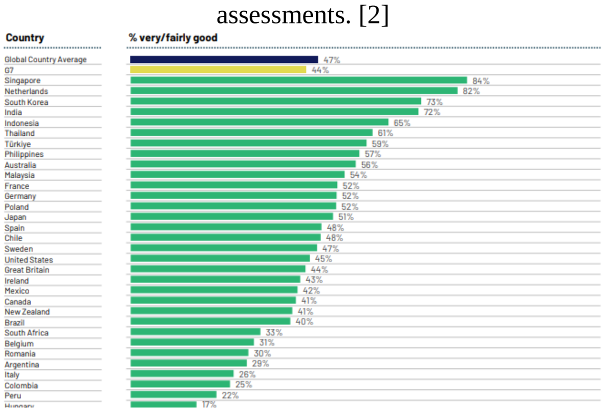

Figure 4 Local road network assessments. [2]

2. MATERIALS AND METHODES

2.1 Objectives of study:

The main objectives of the study are: exerting pressure on the authorities responsible for road maintenance; increasing the level of civic engagement among citizens; calculating a performance score for companies carrying out infrastructure works; raising the level of trust in public institutions.

2.2 The proposed solutions:

a) use of the accelerometer to assess road quality and detect potholes, including graphical interpretation;
b) pothole detection using a camera;
c) dimensional analysis of potholes (Fig. 5, Fig. 6, Fig. 7).

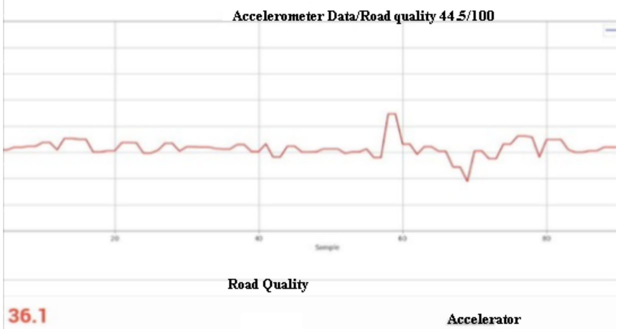

Figure 5 Road quality measured using an accelerometer

Figure 6 Identifying potholes using a camera

Journal of Marine Technology and Environment
DOI:10.53464/JMTE.02.2026.03
ISSN (Print): 1844-6116
ISSN (Online): 2501-8795
https://www. jmte.eu

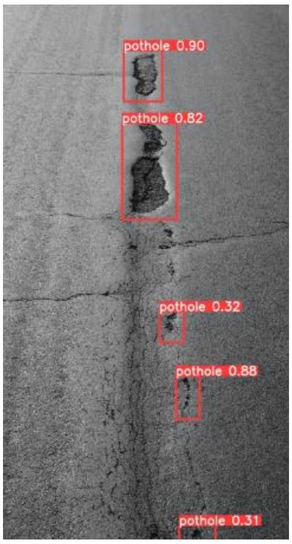

Figure 7 Dimensional analysis of pits

2.3 Defect detection methods :

The study aims to detect defects in images using two methods:

1) the automated YOLOv8 model, where some classes (defectType1, defectType2) have very small bounding boxes, while others (defectType3, defectType4) have large boundaries. Real-time operation is achieved (at least 5 Hz on Jetson Xavier), utilizing the SAHI (Slicing Aided Hyper Inference) technique;

2) using an instrumental scanning technique with LiDAR. Data were collected and processed, with the measurements interpreted graphically.

The steps we follow are:

- we use the SAHI (*Slicing Aided Hyper Inference*) [5]technique, specifically:

1. We attempted iterative learning, first training on smaller image slices (340px x 340px) and then using the trained weights for the next slice size (e.g., 480px x 480px), up to 640px x 640px slices.

2. We also tried training the network on a dataset combining these slices of different sizes [340px, 480px, 640px].

The second method yields the best results. The computational algorithm is shown below (Fig. 8):

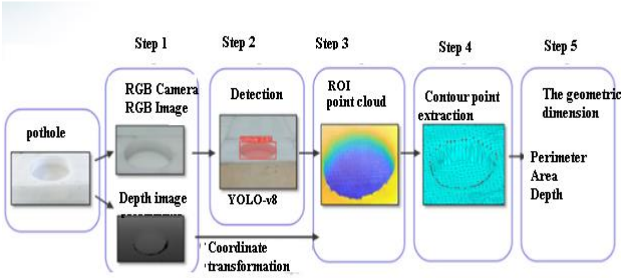

Figure 8 Calculation algorithm for pothole identification

2.4 Selection of the LiDAR instrumental scanning technique

Selecting a LiDAR (Light Detection and Ranging) sensor for pothole detection requires a careful analysis of several key criteria to ensure accuracy and efficiency. The technology utilizes laser pulses to create high-resolution 3D models of the road surface, enabling the automated identification of defects (Fig. 9). [6]

Figure 9 LiDAR – operating principle. [6]

This process, leveraging the constant speed of light, enables the highly precise calculation of the beam's distance from the target. This distance information is combined with X, Y, and Z coordinates to create a three-dimensional point cloud. This point cloud provides a highly detailed model of the scanned area or object.

The LiDAR system consists of:

- a laser scanner,
- a global positioning receiver (GPS system),
- an inertial measurement unit (IMU).

The laser scanner measures distance by transmitting and receiving beams.

The GPS receiver determines the device's location.

The inertial measurement unit measures the angular position—that is, the device's orientation.

Using these three components, a three-dimensional model is created through the precise geo-referencing of the acquired data.

Journal of Marine Technology and Environment
DOI:10.53464/JMTE.02.2026.03
ISSN (Print): 1844-6116
ISSN (Online): 2501-8795
https://www.jmte.eu

2.5 Data collection

The LiDAR system employed can be mounted on a platform that presents both advantages and disadvantages. Our LiDAR system is a terrestrial system capable of providing higher-resolution data. When data collection begins, laser beams are continuously directed at the surface to be scanned, and the return times of the reflected beams are recorded. The collected data is subsequently processed and converted into a three-dimensional model. Proper system calibration during the data collection process is essential. The operational stages of the LiDAR system are:

a) emission of the laser beam;
b) detection of the reflected light beam;
c) measurement of the return time of the reflected beams;
d) calculation of the distance;
e) positioning to determine location using GPS and measurement of angular position using an Inertial Measurement Unit (IMU);
f) creation of a 3D point cloud;
g) analysis and interpretation of the collected data.

2.6 Data processing

The collected LiDAR data are processed to make them usable. They undergo several stages: data cleaning, filtering, classification, and modelling.

- The data cleaning phase involves removing data deemed useless or erroneous.
- The filtering phase entails classifying data based on specific criteria and removing unwanted elements.
- The classification phase involves grouping data according to characteristics specific to the study area.
- The modelling phase involves creating three-dimensional models using the processed data.

2.7 Method for analysing collected data

The technology for analysing data collected via the LIDAR system is presented in Annex 3. It involves: classification algorithms, segmentation techniques, filtering methods, feature extraction operations, surface modelling, and change detection analyses.

2.8 Equipment used for LiDAR technology

The following LiDAR equipment is used to detect imperfections on national roads (Fig. 10):

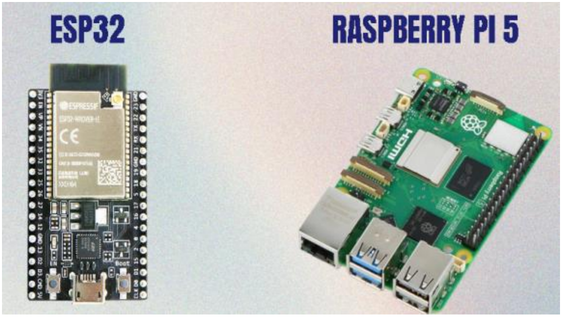

Figure 10 Choosing the processor.[3]

1. A LiDAR laser scanner that measures distances by emitting laser beams.[2]
2. A positioning system (GPS/IMU) required for the geo-referencing of the correct geographic location.[2]
3. A unit for recording and storing the collected data.
4. Equipment for controlling the scanning process and displaying data in real time.
5. A power source to meet the system's energy requirements.
6. Calibration equipment to ensure the accuracy of the LiDAR system. [2]

3. RESULTS AND DISSCUTIONS

The results are: LiDAR data (Fig. 11); Graph conversion and interpretation (Fig. 12) and Mapping (Fig. 13).

Figure 11 : LiDAR data

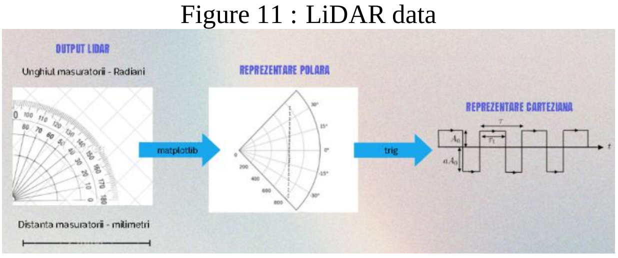

Journal of Marine Technology and Environment
DOI:10.53464/JMTE.02.2026.03
ISSN (Print): 1844-6116
ISSN (Online): 2501-8795
https://www.jmte.eu

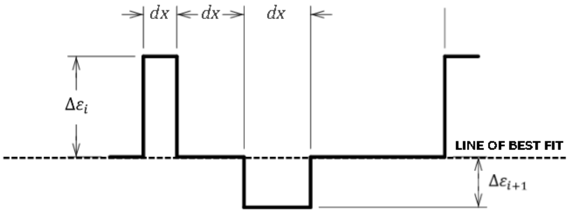

$$\overline{\partial_p} = \sqrt{\frac{\sum_{i=1}^{n} f_i(\varepsilon_i - \bar{\varepsilon})^2}{\sum_{i=1}^{n} f_i}}$$

Figure 12 Graph conversion and interpretation

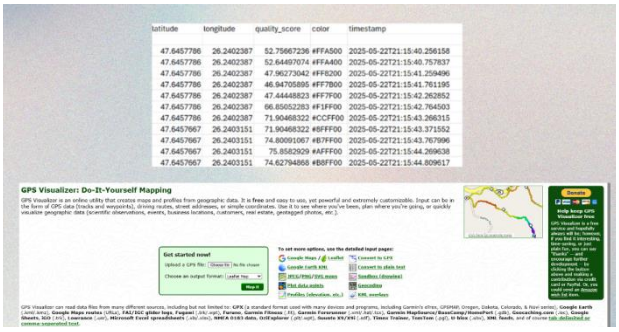

Figure 13 GPS mapping visualization

To examine the practical application of this method, a case study is presented below.

2. 9 Case Study – Lake Tăbăcăriei Neighborhood

GPS, IMU, and a LiDAR system were used to georeference the correct geographical location.

Lake Tăbăcăriei is located north of the city of Constanța and covers an area of approximately 99 hectares.[7]

Its banks have been entirely straightened and reinforced. The western bank rises to an elevation of 6–7 m, while the elevations to the east and south are lower, ranging from 2 to 4 m. In the northern section, the shoreline is very low-lying (1–2 m).

Relatively isolated from natural sources, Lake Tăbăcăriei has a depth varying between 1.5 m and 4.4 m, relying on water inflow from Lake Siutghiol. Excess water is discharged from Lake Tăbăcăriei into the sea via a sluice gate located at the "Pescărie" site.[7]

Google Earth will be used for the Lake Tăbăcăriei location (Fig. 14, Fig. 15).

Figure 14 Studied location

Figure 15 Google Earth's map representation

. 2. 10 Road defect detection

The LiDAR system employs remote sensing technology, emitting pulsed laser beams and calculating the time required for these pulses to reflect back to the sensor. [26]

The LiDAR scanner generates point clouds—effectively constructing a 3D model—that accurately map the contours of defects on the analysed road.

The distance to the object is calculated using the following relationship:

$$D_{ob} = v_l * t/2 \qquad (1)$$

where:

D_{ob} – distance to the object;

v_l – speed of light;

t – time of flight of the light pulse.

This relationship clearly demonstrates how LiDAR technology utilizes the speed of light and the time of flight of the light pulse.

At the same time, it ensures extremely precise and reliable measurements.

The road defect is captured by the LiDAR system sensor, which measures the 3D depth of the pothole or road defect (Fig. 3.16). The detector captures the light reflected from the road defect (via silicon avalanche photodiodes (APDs) or photomultipliers (PMTs) – Fig. 3.8), while the GPS receiver tracks altitude and location using the coordinates used for mapping (Fig. 3.13).

Journal of Marine
Technology and Environment
DOI:10.53464/JMTE.02.2026.03
ISSN (Print): 1844-6116
ISSN (Online): 2501-8795
https://www.jmte.eu

Figure 16 Representation of the road defect

An Inertial Measurement Unit (IMU) monitors the vehicle's speed and direction, ensuring precise positioning of the pulsed laser beams on the ground surface—and, by extension, on road defects (potholes) (Fig. 3.16).

A topographic LiDAR is used for mapping land surfaces.

2.11 *Analysis of road quality in the study area*

Based on information regarding air quality indicators in the study area, it was found (Fig. 17)[8-9].

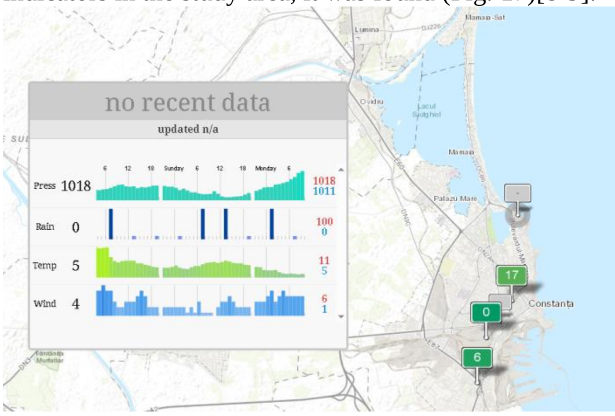

Figure 17 Air quality indices in the Lake Tăbăcărie-Dolphinarium neighborhood area

A comparison with historical data for the area reveals an improvement in air quality resulting from the improved quality of the roads (Fig. 18, Fig. 19, Fig. 20, Fig. 21, Fig. 22) [10]:

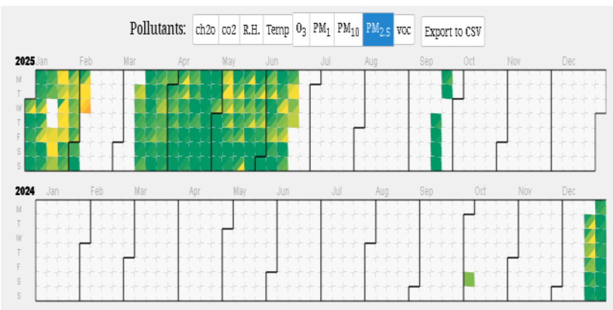

Figure 18 History of pollutants in the study area – PM2.5. [10]

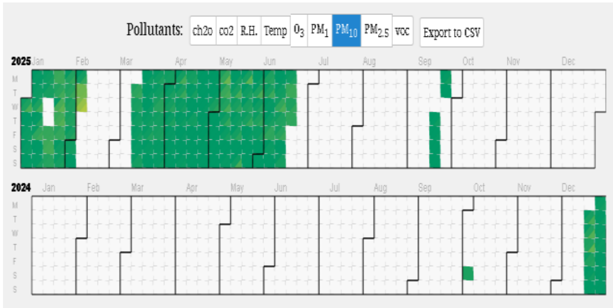

Figure 19 History of pollutants in the study area – PM10. [10]

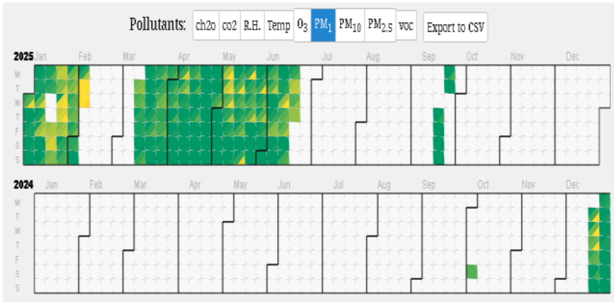

Figure 20 History of pollutants in the study area – PM1. [10]

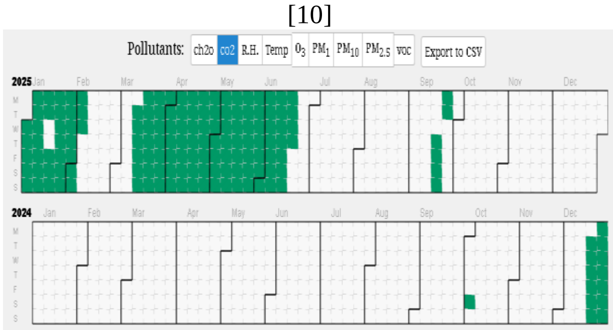

Figure 21 History of pollutants in the study area – CO_2. [10]

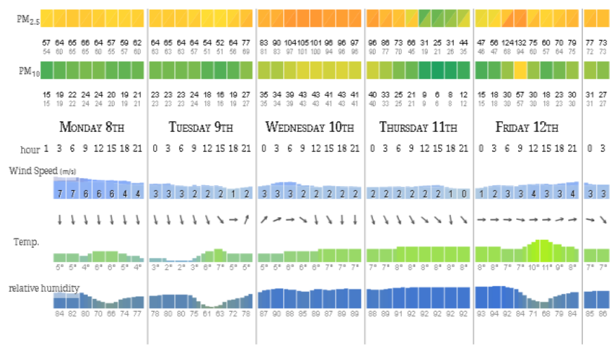

Figure 22 PM2.5 and PM10 air quality index levels as of December 2025. [10]

Journal of Marine Technology and Environment
DOI:10.53464/JMTE.02.2026.03
ISSN (Print): 1844-6116
ISSN (Online): 2501-8795
https://www. jmte.eu

A road network reorganization project is currently being implemented in Constanța, under which 28 streets are being converted to one-way traffic to alleviate congestion and improve road quality. In conclusion, the air quality index map for the study area can be analysed in terms of risk as follows (Fig. 23, Table 1, Table 2):

Figure 23 Real-time visual map of the air quality index in the Tăbăcărie Lake – Dolphinarium area.

Table 1. Air risk matrix for the Lake Tăbăcărie-Dolphinarium area

Type of Risk	Probability	Environmental impact	Pollution	Cause
High	Big	Big	NOx, NO_2, suspended particulate matter	Heavy road traffic on Mamaia Bd. and adjacent streets.
Medium	Medium	Medium	Odor pollution (unpleasant odors)	The lake's poor ecological condition (reed beds, waste accumulation, eutrophication)

Table 2 Air quality assessment for March 2026

Pollutant	Level of risk	Environmental and health impact
PM2.5	Moderate	Respiratory discomfort
NO_2	Low/Medium	Traffic on Mamaia Boulevard
O_3	Variable	It grows during warm days.

The implementation of additional traffic-smoothing measures also aims to reduce road surface deterioration caused by large vehicles or by construction work not originally included in the city's urban development plan [9-11].

4. CONCLUSIONS

The Constanța Municipality, through SC Confort Urban SRL, has initiated a traffic management project to reorganize the road layout in the Dolphinarium area, addressing mobility and traffic safety issues along the streets within the perimeter defined by Mamaia Boulevard, Ion Rațiu Street, Tomis Boulevard, Alexandru Lăpușneanu Boulevard, and Soveja Street.

This measure was adopted both to improve traffic flow and to rectify identified shortcomings. Current conditions show that these two-way streets have become difficult to navigate due to the large number of vehicles parked on the roadway; these vehicles impede traffic in both directions and can even block the passage of emergency vehicles when intervention is required.

Journal of Marine Technology and Environment
DOI:10.53464/JMTE.02.2026.03
ISSN (Print): 1844-6116
ISSN (Online): 2501-8795
https://www. jmte.eu

This study examined road and air quality in the context of current legislative requirements and modern technologies mandated at the European level.
The durability of asphalt roads is fundamental to ensuring an efficient and sustainable transport network. Our multidimensional approach encompasses the selection of quality materials, advanced construction techniques, and a rigorous maintenance and monitoring program. Selecting high-quality asphalt mixtures is the essential first step in ensuring road durability. Proper asphalt compaction is crucial for maintaining the road's structural integrity. Integrating geo-synthetics into the road structure offers an effective solution for enhancing stability and durability. Geo-synthetic materials, such as geogrids and geotextiles, contribute to uniform load distribution, thereby preventing deformation and cracking. Continuous monitoring and performance assessment are vital components in maintaining and improving road infrastructure quality. Implementing an effective monitoring and evaluation strategy enables us to promptly identify issues and intervene quickly with repairs or improvements, thereby extending the roads' service life and optimizing the user experience.

5. CREdit authors statement

Conceptualization: D.M.-V., P.M., P.F-V.;Data curation; D.M.-V., P.M., P.F-V.;

Formal analysis: D.M.-V., P.M., P.F-V.;

Funding acquisition:-not applicable;

Investigation: D.M.-V., P.M., P.F-V.;

Methodology: D.M.-V.;

Project administration: P.M.;

Resources: D.M.-V., P.M., P.F-V.;

Software: D.M.-V.;

Supervision: D.M.-V.;

Validation: D.M.-V.;

Visualization: D.M.-V.;

Writing – original draft: P.M.;

Writing – review & editing: P.M.

6. REFERENCES

[1] https://www.canva.com/design/DAGklqWDOow/Lb-b-8yN-aw_K5ulYS-A5A/edit

[2] https://www.ipsos.com/sites/default/files/ct/news/documents/2024-11/ipsos-global-infrastucture-index-2024.pdf

[3] Radu B., *Încrederea cetățenilor în instituțiile publice. o perspectivă teoretică*, Revista Transilvană de Ştiinţe Administrative 2(47), pp. 72-84, 2020.

[4] https://www.spglobal.com/spdji/en/methodology/article/sp-thematic-indices-methodology/

[5] F. K. Akyon, S.O., Altinuc, A. Temizel, *Slicing Aided Hyper Inference and Fine-Tuning for Small Object Detection*, Proc. Of 2022 IEEE International Conference on Image Processing (ICIP) pp 1-5, Bordeaux, France

[6] https://www.hostragons.com/ro/blog/principiul-de-functionare-al-tehnologiei-lidar

[7] udiotravelguide.ro/parcul-tabacariei-constanta/

[8] https://www.sinoseen.com/ro/what-is-lidar-technologyhow-does-it-help-with-depth-measurement,

[9] https://aqicn.org/station/romania-constan%C8%9Ba-lac-tabacarie-delfinariu-strada-pescarilor/

[10] https://aqicn.org/station/@506818/

[11] SALAMA BENAZAR. ROSANA, MARTINEZ MARIN. JESUS E., *SOCIO-ECONOMIC & ENVIRONMENTAL IMPACT OF THE PORT EFFICIENCY IN THE TRANSPORT LOGISTIC CHAIN*, Journal of Marine Technology and Environment, vol. 2, pp 69-76, 2013, Nautica Publish House, Constanta, Romania.

Journal of Marine Technology and Environment
DOI:10.53464/JMTE.02.2026.04
ISSN (Print): 1844-6116
ISSN (Online): 2501-8795
https://www. jmte.eu

SERIOUS HUMAN CONSEQUENCES IN SHIPPING ACCIDENTS: TEMPORAL DISCRIMINATION AND CALIBRATION USING TSB MARSIS DATA, 1995-2026

Dr. David O. KREMELBERG[1]

[1]Adjunct Instructor, Maine Maritime Academy, 1 Pleasant Street, Castine, ME 04420, USA
ORCID: 0009-0003-1260-5779; e-mail address: david.kremelberg@mma.edu

Abstract: Maritime risk management requires separating accident occurrence from consequence severity conditional on an accident. This study used the Transportation Safety Board of Canada public Marine Safety Information System (MARSIS) to examine serious human consequences among 9,491 reportable shipping accidents from 1995 through July 2026; 293 (3.09%) involved death, a missing person, or serious injury. Among accident types, the all-period occurrence-level logistic model showed the largest adjusted association for capsize (odds ratio, OR 10.36, 95% confidence interval, CI 6.76-15.88), followed by sinking/loss/abandonment (OR 2.74, 95% CI 1.79-4.19); moderate/adverse/ice sea state had OR 2.25 (95% CI 1.65-3.08). A historical model developed on 6,923 accidents from 1995-2014 retained discrimination in 2,568 later accidents (area under the receiver operating characteristic curve (AUC) 0.826; precision-recall AUC (PR-AUC) 0.237) but under predicted absolute risk: 93 events were observed versus 41.9 expected (observed/expected ratio 2.22). Connected-component resampling supported these conclusions. Post hoc time-specification checks predicted 61.3 events without calendar year and 67.7 with a linear year term, indicating that extrapolation of the original spline contributed to under prediction while not fully explaining it. The full historical model also materially outperformed an accident-type-only benchmark for AUC, PR-AUC, and Brier score. Expanding-origin refits using more contemporary data improved average calibration in later forward blocks. The results support transparent retrospective consequence-risk stratification, but not a fixed operational probability threshold: contemporary refitting, prospective evaluation, and a defined prediction time are required before deployment.
Key words : Accident severity; calibration; consequence risk; maritime safety; MARSIS; temporal validation.

1. INTRODUCTION

Maritime safety risk is not a single probability. Risk-management frameworks separate hazard identification, event occurrence, consequence development, controls, and monitoring [1]. For accident databases, an additional distinction is essential: the probability that a vessel experiences an accident is different from the probability that an accident already recorded by an authority produces death or serious injury. Commercial-fishing research has made this distinction explicitly when comparable data on safe trips were unavailable [2]. The public Marine Safety Information System (MARSIS) is likewise occurrence-centred rather than a denominator of safe voyages or vessel-time exposure [3]. The estimand here is therefore P(serious human consequence | TSB-reportable shipping accident), not accident incidence.

Human-consequence modelling has substantial precedent. Weng and Yang analysed 24,301 worldwide ship-accident records from 2001 through February 2011, using logistic regression for fatal versus nonfatal accidents and a zero-truncated negative-binomial model for mortality among fatal accidents; their design used a random training/test split and found especially strong consequences for sinking as well as associations with accident type, adverse weather, darkness, distance from shore, and cruise-vessel status [4]. Talley, Jin, and Kite-Powell modelled nonfatal injuries, deaths, and missing crew in U.S. Coast Guard vessel accidents with count methods [5]. More recently, Wang et al. modelled four ordered injury-severity levels using 1,128 investigation reports from seven national agencies, including the TSB, and a zero-inflated ordered probate model; collision vessels were represented separately, producing 1,294 ship-level observations [6]. These studies establish that regression-based and human-specific maritime consequence models are not themselves novel.

A broader literature has modelled accident severity and accident mechanisms using ordered regression, Bayesian networks, and data-driven methods [7,8,9,10,11]. Recent studies add text mining, explainable ensemble methods, and operationally richer Bayesian or machine-learning frameworks [12,13,14,15]. Reviews emphasize that

Journal of Marine Technology and Environment
DOI:10.53464/JMTE.02.2026.04
ISSN (Print): 1844-6116
ISSN (Online): 2501-8795
https://www. jmte.eu

maritime risk analyses are strongly shaped by the characteristics and availability of underlying data [1,16].

Canadian fishing studies further show that environmental conditions can affect both incident occurrence and consequences, while policy translation requires attention to stability, weather information, training, communication, and search-and-rescue planning [17,18].

The present contribution is therefore methodological and data-structural rather than algorithmic. It uses the full public TSB structured occurrence record over approximately three decades, defines an occurrence-level human endpoint so that a single accident outcome is not duplicated across its vessels, excludes obvious post-outcome response variables, and distinguishes relative discrimination from absolute probability calibration. Calibration is important because a model may rank cases well while systematically misstating risk levels [19]. Temporal structure also matters: random cross-validation can understate predictive error when nearby observations share temporal or hierarchical dependence, so out-of-time evaluation is more appropriate when the intended question concerns later periods [20]. Reporting and model-identity terminology were additionally informed by TRIPOD+AI guidance for regression and machine-learning prediction studies, adapted here to a nonclinical maritime setting [21].

The objectives were to identify accident, vessel, operational, geographic, temporal, and environmental characteristics associated with serious human consequences among TSB-reportable shipping accidents; to determine how well a transparent multivariable model stratified later accidents; and, after cross-era under prediction was observed, to conduct a limited set of explicitly post hoc checks addressing calendar-time specification, incremental value, recurrent-vessel dependence, missingness, multi-vessel aggregation, and a specific gross-tonnage data-quality anomaly. Because the source contains finalized occurrence fields rather than time-stamped initial reports, the analysis is described as retrospective consequence profiling.

Operational triage or pre-accident deployment is not claimed.

2. DATA AND METHODS

2.1 Data source, cohort, and outcome:

Data were obtained from the TSB public MARSIS release, comprising occurrence, vessel, navigation-equipment, lifesaving-equipment, recording-equipment, injury, and data-dictionary files [3]. The study window was 1 January 1995 through 31 July 2026. Starting from 88,054 raw occurrence rows representing 48,820 unique occurrence identifiers, 27,035 identifiers fell within the study window, 11,228 were classified as accidents, and 9,491 met the predefined shipping-accident classifications.

All 9,491 linked to occurrence-level vessel aggregates. Reportable incidents were excluded. Accidents aboard ship were also excluded because the TSB definition incorporates a person being killed or seriously injured, which would make the analytic denominator partly outcome-defined [22].

The primary endpoint was occurrence-level: at least one death, missing person, or serious injury. TSB regulations define serious injury using specified clinical and hospitalization criteria [23]. Of the 9,491 accidents, 293 met the primary endpoint, 9,198 did not, 199 involved death or a missing person, and 94 involved serious injury without death or missing persons. Death, missing-person, and injury fields can overlap and were not summed as mutually exclusive person counts. Injury records were de-duplicated by victim-count identifier before reconciliation, and reconstructed July 2026 shipping-accident counts agreed with the TSB published table [24]. A prespecified secondary endpoint included death or missing person only.

The TSB introduced a new marine occurrence database in November 2013 and revised reporting requirements effective 1 July 2014 [22]. The primary all-period association model used all eligible accidents. For temporal evaluation, 1995-2014 accidents formed the development sample and 2015-July 2026 accidents formed the later evaluation sample, thereby beginning evaluation with the first full calendar year after the reporting change. The later era was subsequently inspected during model revision, so no post hoc comparison is described as a new untouched holdout.

2.2 Predictors and pre-processing:

Accident type was coded as collision/allision (reference), grounding, fire/explosion, capsize, sinking/loss/abandonment, or unseaworthy/unfit. Vessel composition was represented by overlapping occurrence indicators for fishing, passenger/ferry, cargo/tanker, and tug/barge/service vessels. Maximum gross tonnage (GT) across vessels represented size and was $\log_2$-transformed so that one coefficient represented a doubling of GT. Operational phase used overlapping indicators for underway, secured/stationary, and not under own power. Region was harmonized to Pacific, Central/Arctic, Atlantic, or Foreign waters. Calendar year, light condition, weather, and sea state completed the core set. Post-accident response, damage, pollution, investigation-class, evacuation, and lifesaving-use variables were excluded from the primary model.

Weather was grouped as clear/overcast, adverse, or unknown/unrecorded; sea state as calm-to-slight, moderate/adverse/ice, or unknown/unrecorded. Positive GT was available for 8,689 accidents (91.5%). Missing $\log_2$(GT) was replaced by the median observed $\log_2$(GT)

Journal of Marine Technology and Environment
DOI:10.53464/JMTE.02.2026.04
ISSN (Print): 1844-6116
ISSN (Online): 2501-8795
https://www. jmte.eu

within each training sample and accompanied by a missing-GT indicator. Unknown categorical states were retained because recording completeness varied strongly by era. This approach preserves a recording-state signal but does not imply that missing-indicator methods recover unbiased physical-variable associations in observational data; that limitation is well established in the missing-data literature [25]. A post hoc deterministic, outcome-blind conditional GT-imputation sensitivity therefore assessed whether the principal associations and temporal calibration were dependent on median imputation. The unusable people-aboard field was excluded before outcome-association fitting after audit showed 3,795 accidents recorded zero aboard, including 75 primary events.

2.3 *Statistical model and validation:*

The primary model was occurrence-level multivariable logistic regression with 26 slope parameters plus an intercept. Calendar year used a natural cubic spline with three degrees of freedom, with knots and boundaries determined only from the corresponding development sample. All core predictors were entered simultaneously; stepwise selection, univariate screening, and outcome-driven deletion were not used. Results are reported as adjusted odds ratios (ORs) with 95% model-based Wald confidence intervals (CIs). Average standardized probabilities and risk differences were obtained by marginal standardization over the empirical all-period covariate distribution; their CIs used the delta method. These are descriptive model translations, not contemporary calibrated predictions and not causal intervention effects. A Firth-type logistic model with intercept correction was prespecified only as a numerical fall-back for sparse sensitivity fits [26].

Internal validation used 500 bootstrap resamples with training-dependent pre-processing repeated inside each resample. Five repeats of stratified 10-fold cross-validation were retained as a secondary internal check. The primary transport assessment applied the 1995-2014 historical equation unchanged to 2015-July 2026. Discrimination was measured with ROC AUC and precision-recall AUC (PR-AUC); overall probability error used Brier score and log loss. Calibration was summarized by calibration intercept, calibration slope, observed-to-expected (O/E) event ratio, and a flexible calibration curve. The calibration intercept used the predicted logit as an offset with slope fixed at one; the calibration slope was estimated in a separate logistic model with an intercept. In the convention used here, a positive calibration intercept denotes systematic under prediction. Because only 93 events occurred in the later sample, the flexible high-risk tail was interpreted cautiously, consistent with recommendations that calibration curves need substantial event counts [19].

Recurrent vessel identifiers created dependence across accidents. Vessel-linked connected components were therefore constructed across the full sample. Later-period performance uncertainty used 2,000 resamples of whole connected components while holding each historical fitted equation fixed. The later sample contained 1,830 components; the largest had 71 accidents. These intervals quantify evaluation-sample dependence conditional on the fitted historical model, not model-development uncertainty. Random cross-validation was not treated as independent temporal evidence because structured random splits can produce optimistic error estimates [20].

Model complexity was interpreted without a mechanical events-per-parameter (EPP) rule. Modern prediction-methodology work shows that required sample size depends on anticipated model performance, outcome risk, and parameterization rather than a universal threshold [27]. Accordingly, the 26-slope historical model and smaller modern updating samples were accompanied by internal validation, sensitivity analyses, and a limited ridge experiment rather than a retrospective claim that a simple EPP threshold proved adequacy.

2.4 *Post hoc revision analyses*

After the original temporal result had been examined, three calendar-time diagnostics were specified using the same historical development sample and later evaluation sample: refitting without calendar year, refitting with a linear year term, and holding the original spline input at the 2014 boundary while retaining the original coefficients. An accident-type-only logistic model provided a simple benchmark. Fixed historical models were also evaluated in 2015-2018, 2019-2022, and 2023-July 2026 blocks; expanding-origin comparisons refit each specification using only preceding eligible accidents. All of these comparisons are labelled post hoc; none restores the independence of the already inspected later outcomes. Paired component resampling compared the original full historical equation with the accident-type-only benchmark.

Additional focused checks addressed data quality and aggregation. Two records for the 42-m ferry R.G.L. Fair weather contained GT=301,287. The design firm lists gross registered tonnage of 304 for the sister-ferry family [28], which flags implausibility but does not verify the individual vessel’s exact GT. Therefore, the raw value was retained in the baseline and treated as missing only in sensitivity analyses; neither 304 nor 301.287 was substituted. A single-vessel sensitivity removed 1,663 multi vessel accidents. Conditional GT imputation also treated the two flagged ferry values as missing and used training-only vessel and era information without the outcome. Performance was also

Journal of Marine Technology and Environment
DOI:10.53464/JMTE.02.2026.04
ISSN (Print): 1844-6116
ISSN (Online): 2501-8795
https://www.jmte.eu

examined separately for later accidents involving vessel identifiers seen or unseen historically. Finally, a limited ridge model was tuned within 2015-2020 using three forward folds and evaluated on the already examined 2021-July 2026 period. These analyses were designed to test stability, not to search until a preferred result appeared.

The font for first and last name of the authors is Times New Roman 11.

3. RESULTS

3.1 Cohort and primary associations

Table 1 describes the cohort. Among 9,491 eligible accidents, 293 (3.09%) met the primary endpoint. Collision/allision (30.7%) and grounding (29.1%) were the most common classifications, but serious outcomes were concentrated in capsize and sinking/loss/abandonment: 90 of 315 capsizes and 81 of 830 sinking/loss/abandonment accidents met the endpoint.

The outcome rate was 28.57% for capsize, 9.76% for sinking/loss/abandonment, 2.30% for fire/explosion, 2.03% for collision / allision, 0.87% for grounding, and 0.19% for unseaworthy/unfit accidents.

The all-period model converged normally (Table 2). Capsize had the largest adjusted association (OR 10.36, 95% CI 6.76-15.88). Its all-period model-standardized descriptive risk was 19.95% (95% CI 15.73%-24.16%), compared with 2.73% for collision / allision. Sinking/loss/abandonment had OR 2.74 (95% CI 1.79-4.19), whereas grounding had OR 0.26 (95% CI 0.16-0.43). Moderate/adverse/ice sea state had OR 2.25 (95% CI 1.65-3.08). The broad adverse-weather indicator did not show a clear additional association conditional on the specified variables (OR 1.04, 95% CI 0.73-1.46); this comparison does not establish that weather has little total causal importance. Passenger/ferry involvement had OR 2.18 (95% CI 1.23-3.85). Each doubling of recorded maximum GT had OR 0.87 (95% CI 0.83-0.92), while secured/stationary status had OR 0.37 (95% CI 0.22-0.63).

Table 1. Selected characteristics of reportable shipping accidents, overall and by serious human-consequence status

Characteristic	**Level**	**Overall *N*=9,491**	**No event *N*=9,198**	**Event *N*=293**
Sample size	*N*	9491	9198	293
Accident type	Collision /allision	2913 (30.7%)	2854 (31.0%)	59 (20.1%)
Accident type	Grounding	2763 (29.1%)	2739 (29.8%)	24 (8.2%)
Accident type	Fire/explosion	1611 (17.0%)	1574 (17.1%)	37 (12.6%)
Accident type	Capsize	315 (3.3%)	225 (2.4%)	90 (30.7%)
Accident type	Sinking/loss/abandonment	830 (8.7%)	749 (8.1%)	81 (27.6%)
Accident type	Unseaworthy/unfit	1059 (11.2%)	1057 (11.5%)	2 (0.7%)
Any fishing vessel involved	Yes	3795 (40.0%)	3633 (39.5%)	162 (55.3%)
Any passenger/ferry vessel involved	Yes	1126 (11.9%)	1085 (11.8%)	41 (14.0%)
Any tug/barge /service vessel involved	Yes	2318 (24.4%)	2269 (24.7%)	49 (16.7%)
Maximum gross tonnage	Median [Q1, Q3]	184.0 [24.0, 9304.1]	204.1 [25.1, 9611.0]	25.0 [10.0, 145.6]
Maximum vessel length (m)	Median [Q1, Q3]	23.4 [12.0, 126.9]	25.0 [12.2, 129.9]	11.4 [8.0, 19.1]
Any vessel secured/stationary	Yes	1723 (18.2%)	1696 (18.4%)	27 (9.2%)
Weather condition	Adverse	1422 (15.0%)	1366 (14.9%)	56 (19.1%)

Note: Percentages are column percentages. Vessel-type flags can overlap and need not sum to 100%. Continuous summaries use observed positive values, with length additionally limited to 500 m. Available-value denominators and unknown categories are in Supplement Table S14.

3.2 Temporal discrimination, calibration, and incremental value

Journal of Marine Technology and Environment
DOI:10.53464/JMTE.02.2026.04
ISSN (Print): 1844-6116
ISSN (Online): 2501-8795
https://www.jmte.eu

The historical development sample contained 6,923 accidents and 200 events; the later evaluation sample contained 2,568 accidents and 93 events. The original historical equation retained AUC 0.826 and PR-AUC 0.237. Connected-component percentile intervals were 0.780-0.869 for AUC and 0.164-0.334 for PR-AUC. The Brier score was 0.03178 (component interval 0.02546-0.03832). Relative ranking therefore transported reasonably well. Table 3 distinguishes the all-period model from the historical fitted equations.

Absolute probabilities did not. The original historical equation predicted 41.9 events where 93 occurred, for O/E 2.22 (component interval 1.80-2.63), calibration intercept 0.938 (0.686-1.148), and calibration slope 0.905 (0.764-1.062). The flexible calibration curve (Figure 1) was above the identity line through most of the supported probability range, with wide uncertainty in the sparse high-risk tail. Thus, discrimination and calibration gave different conclusions, consistent with the distinction emphasized in prediction-methodology literature [19,29].

The post hoc accident-type-only benchmark had lower AUC (0.741) and PR-AUC (0.141) and a higher Brier score (0.03268) but better average calibration (O/E 1.25). Relative to that benchmark, the original full historical equation improved AUC by 0.0846 (paired component interval 0.0517-0.1186), PR-AUC by 0.0955 (0.0580-0.1582), and had a Brier-score difference of -0.00090 (-0.00168 to -0.00016). The fuller model therefore added meaningful ranking information beyond accident type alone, even though its fixed historical probability scale transported less well.

Table 2. Selected all-period adjusted associations and standardized descriptive risk translations.

Predictor / contrast	Adjusted OR (95% CI)	Standardized risk (95% CI)	Risk difference (95% CI)
Grounding vs collision/allision	0.26 (0.16-0.43)	0.74% (0.44-1.03)	-1.99 pp (-2.81 to -1.17)
Fire/explosion vs collision/allision	0.96 (0.61-1.51)	2.62% (1.78-3.46)	-0.10 pp (-1.25 to +1.05)
Capsize vs collision/allision	10.36 (6.76-15.88)	19.95% (15.73-24.16)	+17.22 pp (+12.85 to +21.59)
Sinking/loss/abandonment vs collision/allision	2.74 (1.79-4.19)	6.87% (5.25-8.48)	+4.14 pp (+2.24 to +6.04)
Passenger/ferry vessel involved	2.18 (1.23-3.85)	5.32% (3.21-7.43)	+2.45 pp (+0.25 to +4.65)
Tug/barge/service vessel involved	0.58 (0.35-0.97)	2.15% (1.38-2.93)	-1.24 pp (-2.30 to -0.18)
Maximum GT, per doubling	0.87 (0.83-0.92)	-	-
Vessel secured/stationary	0.37 (0.22-0.63)	1.49% (0.86-2.13)	-2.00 pp (-2.86 to -1.15)
Adverse weather vs clear/overcast	1.04 (0.73-1.46)	3.59% (2.70-4.48)	+0.11 pp (-0.89 to +1.11)
Moderate/adverse/ice sea state	2.25 (1.65-3.08)	4.88% (3.93-5.84)	+2.40 pp (+1.35 to +3.45)

Note: Model-based Wald CIs are shown for ORs; delta-method CIs for standardized probabilities and differences. Standardization uses all 9,491 accidents. Risk units are percent; difference units are percentage points (pp). References are collision / allision for accident type, clear/overcast for weather, calm-to-slight for sea state, and absence for binary vessel/phase flags. Reference risks are in Supplement Table S15. These are descriptive associations, not contemporary calibrated probabilities or causal effects.

3.3. What the time diagnostics changed

Calendar-time specification materially affected the magnitude of under prediction without materially changing discrimination. Using the same 1995-2014 development and 2015-July 2026 evaluation samples, removing year predicted 61.3 events (O/E 1.52; AUC 0.830), while a linear year term predicted 67.7 (O/E 1.37; AUC 0.831). Holding the original spline input at 2014 predicted 52.8 (O/E 1.76). Under prediction therefore persisted, but extrapolation of the original natural-spline time term contributed substantially to its magnitude. Because these alternatives were evaluated after the later outcomes were known, none is presented as a newly validated replacement model.

Shorter forward blocks showed the same pattern. With the fixed 1995-2014 original equation, O/E increased from 1.66 in 2015-2018 to 2.31 in 2019-2022 and 3.32 in 2023-July 2026. The fixed linear-year sensitivity reduced those values to 1.19, 1.38, and 1.65. However, expanding-origin refits added an important qualification: when the original specification was refit through 2018, O/E was 1.02 for 2019-2022, and when

Journal of Marine Technology and Environment
DOI:10.53464/JMTE.02.2026.04
ISSN (Print): 1844-6116
ISSN (Online): 2501-8795
https://www.jmte.eu

refit through 2022, O/E was 0.96 for 2023-July 2026. This pattern suggests that updating with contemporary data can improve average calibration more effectively than treating any one historical time parameterization as permanent. It does not identify a single causal source of the temporal shift.

3.4 Risk concentration and robustness

Development-defined risk strata separated later accidents strongly. The highest-risk 302 accidents, 11.8% of the later sample, contained 52 of 93 events (55.9%); the highest two strata contained 71.0% of events in 24.3% of accidents. This demonstrates concentration of retrospective consequence risk, not an optimal operational threshold or decision benefit.

The new robustness checks did not materially alter the central conclusions. Treating the two unresolved ferry GT values as missing changed temporal AUC from 0.82604 to 0.82591 and O/E from 2.2206 to 2.2159; all-period capsize OR changed from 10.357 to approximately 10.38. Train-only conditional GT imputation yielded temporal AUC 0.827 and O/E 2.19. The single-vessel subset contained 7,828 accidents and 248 events; its historical-to-later AUC was 0.833 and the same cross-era under prediction remained (O/E 2.39). In later data, 863 accidents involved at least one vessel identifier seen historically but contained only eight events; 1,705 accidents with no historically seen vessel contained 85 events, so the subgroup contrast is exploratory rather than a stable transport estimate. The limited ridge diagnostic in the 2021-July 2026 reused era produced AUC 0.839 and O/E 1.26, essentially similar to the modern reduced-model refit.

Table 3 Predictive performance, model identity, and post hoc temporal comparisons

Model / evaluation	**AUC**	**PR-AUC**	**Brier**	**O/E**	**Cal. int.**	**Cal. slope**
All-period apparent (1995-Jul 2026)	0.851	0.275	0.02519	1.00	0.000	1.000
All-period bootstrap corrected	0.838	0.250	0.02580	-	0.005	0.945
Historical original: 1995-2014 → 2015-Jul 2026	0.826	0.237	0.03178	2.22	0.938	0.905
Post hoc: historical model without year	0.830	0.242	0.03084	1.52	0.499	0.929
Post hoc: historical model with linear year	0.831	0.243	0.03066	1.37	0.383	0.929
All-period apparent (1995-Jul 2026)	0.851	0.275	0.02519	1.00	0.000	1.000
Post hoc: accident-type-only benchmark	0.741	0.141	0.03268	1.25	0.259	0.803

Note: The historical original row records the preexisting historical equation applied to the later era. All no-year, linear-year, and benchmark comparisons were added after the later outcomes had been examined and are therefore exploratory. Connected-component 95% intervals for the historical original model were AUC 0.780-0.869, PR-AUC 0.164-0.334, O/E 1.80-2.63, calibration intercept 0.686-1.148, and calibration slope 0.764-1.062. The all-period model uses 9,491 accidents/293 events for development and internal evaluation; historical comparisons use 6,923/200 for development and 2,568/93 for evaluation. O/E = observed/expected events; Cal. int. = calibration-in-the-large; PR-AUC = precision-recall AUC.

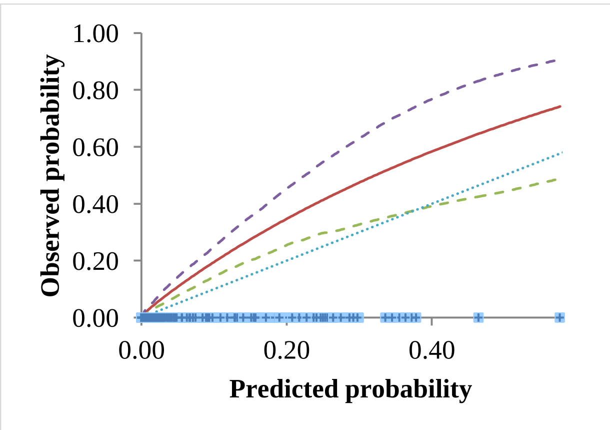

Figure 1 Calibration of the original 1995-2014 model in 2015-July 2026.

Journal of Marine Technology and Environment
DOI:10.53464/JMTE.02.2026.04
ISSN (Print): 1844-6116
ISSN (Online): 2501-8795
https://www. jmte.eu

The solid curve is a three-degree-of-freedom natural-spline logistic smoother of the predicted logit; dashed boundaries are pointwise 95% limits from 500 component resamples. The dotted diagonal denotes equality and baseline marks show predicted probabilities. The sparse high-risk tail is uncertain. The historical model is held fixed.

4. DISSCUTIONS

The principal substantive finding is a clear hierarchy of serious human-consequence risk conditional on a reportable shipping accident. Capsize and sinking/loss/abandonment were the strongest major accident-type signals, and moderate/adverse/ice sea state remained an important environmental marker after adjustment. These patterns agree with earlier evidence linking sinking or stability loss to fatalities or higher injury severity [2,4,5,6]. The present occurrence-level design differs from ship-level analyses that represent the vessels in a collision separately: that choice prevents one accident outcome from being counted repeatedly merely because multiple vessels were involved.

The environmental result should be interpreted specifically. Sea state showed a clear adjusted association, whereas the broad weather composite did not show a clear additional association conditional on the model's other variables. Canadian fishing research has linked wind, temperature, ice, storm intensity, and other environmental factors to incident severity, and policy reviews emphasize weather information, stability, and response planning [17,18]. The current findings therefore do not imply that weather is unimportant; they show that, within this coarse administrative representation, sea state carried a more clearly estimated conditional association than the general adverse-weather flag.

Vessel findings require similar restraint. Passenger/ferry involvement was associated with higher consequence risk, while greater recorded maximum GT was associated with lower conditional odds. Wang et al. also found that GT can act differently across injury-propensity and conditional-severity processes [6]. Because the MARSIS people-aboard field could not be used reliably, passenger/ferry involvement may partly proxy the number of persons exposed to harm within an accident. Neither that association nor the inverse GT association can be translated into fleet-wide accident incidence without appropriate traffic or vessel-time denominators; passenger-ship safety studies using exposure concepts address a different estimand [30].

The methodological result is at least as important as the association estimates. The fixed historical equation retained good discrimination yet substantially under predicted later events. Post hoc time diagnostics showed that the original spline's extrapolation amplified this problem, but they did not reduce the issue to a single modelling mistake: a linear term still under predicted, and regular expanding-origin refitting improved average calibration more effectively in later blocks. This is consistent with the general prediction literature's warning that population drift, measurement changes, and model specification can all affect calibration, and that model updating may be required [19]. The TSB's 2013-2014 system and reporting transition provides a plausible administrative discontinuity, but the data do not identify how much of the temporal pattern reflects reporting, fleet composition, safety practice, case mix, or unmeasured variables.

The accident-type-only benchmark clarifies what the full model contributes. Accident type alone was better calibrated on average in the later era, but the full model materially improved AUC, PR-AUC, and Brier score under paired component resampling. Thus, the choice is not between a 'good' simple model and a 'bad' full model. The fuller score carries additional information for ranking accidents, while its absolute probability scale requires updating. This is precisely the situation in which reporting only discrimination would be incomplete [19,21].

Finally, the dependence analyses support a more qualified interpretation of validation. Chronological splitting is preferable to random splitting for later-period transport, but recurrent vessel identifiers mean that time alone does not remove every hierarchical connection. Whole-component resampling accounted for recurrent-vessel dependence in performance uncertainty while leaving the core conclusion intact. This aligns with structured-validation work showing that validation design should reflect the dependence structure relevant to the intended prediction target [20].

5. PRACTICAL MARITIME RISK-MANAGEMENT IMPLICATIONS

The results are most defensible as a retrospective consequence-risk layer for safety review, scenario planning, and research prioritization. They are not a pre-accident incidence model and do not establish that all retained fields are available at an operational decision time. In the later sample, risk was nevertheless strongly concentrated: 55.9% of events fell within the highest-risk 11.8% of accidents. That concentration may help identify scenarios deserving deeper review, but no decision-curve, cost function, or resource-allocation threshold was evaluated.

The substantive signals support attention to stability and loss-of-buoyancy scenarios, sea-state conditions, and the response implications of passenger/ferry involvement, while not estimating the effectiveness of any particular intervention. Canadian fishing-policy work illustrates how environmental evidence can be translated into stability, weather-information, training,

Journal of Marine Technology and Environment
DOI:10.53464/JMTE.02.2026.04
ISSN (Print): 1844-6116
ISSN (Online): 2501-8795
https://www. jmte.eu

communication, and search-and-rescue planning questions [18]. Within this journal, Demirci and Cicek similarly used data-driven risk-area prioritization to focus port-state-control inspections by ship characteristics [31]. The present model can inform that kind of prioritization logic only as a research signal: operational use would require a clearly defined prediction time, a predictor-availability audit, contemporary fitting, prospective evaluation, and an explicit utility framework.

6. LIMITATIONS

Several limitations constrain the inference. First, MARSIS is occurrence-centred and provides no corresponding population of safe voyages or vessel-time exposure [3]. The study cannot estimate accident incidence. Accidents aboard ship were excluded because their definition incorporates human harm, and the binary composite endpoint gives equal occurrence-level weight to one serious injury and multiple fatalities. The fatal/missing sensitivity partially addresses, but does not eliminate, that loss of severity detail.

Second, the public records span more than three decades of changes in reporting, taxonomy, fleet composition, safety practice, and field completeness. Explicit unknown categories preserve information but are not substitutes for measured physical conditions. The post hoc conditional GT sensitivity is assumption-dependent deterministic imputation, not multiple imputation, and the missing-data literature cautions against interpreting missing indicators as unbiased confounder adjustment in observational settings [25]. The GT=301,287 ferry value remains unresolved; retaining the raw value in the baseline and isolating it in sensitivity avoids inventing an unsupported correction.

Third, the structured public fields omit many human, organizational, management, and response-context factors available in detailed investigation reports [10,12,16]. Residual confounding and measurement error are therefore plausible, and adjusted associations are not causal effects. The all-period standardized probabilities describe the observed 1995-July 2026 covariate distribution; they are not calibrated contemporary risk estimates.

Fourth, the 2015-July 2026 period was originally held out for the historical equation but was subsequently inspected during revision. The original temporal result remains a valid record of how that pre-existing historical equation performed when first applied, but post hoc no-year, linear-year, benchmark, expanding-origin, updating, and ridge comparisons are exploratory analyses within already examined data. No language in this paper treats those comparisons as a new independent validation cohort.

Finally, this is temporal evaluation within the same national administrative system, not external-country or prospective validation. Connected-component performance intervals condition on the fitted historical equations and do not incorporate development-sample uncertainty. No decision-analytic net benefit was estimated. These constraints preclude operational probability thresholds while leaving the observed association patterns and relative risk concentration scientifically informative.

7. CONCLUSIONS

Across 9,491 TSB-reportable shipping accidents from 1995 through July 2026, serious human consequences were uncommon overall but concentrated in capsize, sinking/loss/abandonment, and moderate or adverse sea-state contexts. Passenger/ferry involvement was also associated with higher conditional consequence risk, whereas grounding and secured/stationary status were associated with lower risk. These are observational, occurrence-conditional associations rather than estimates of accident incidence or causal intervention effects.

A historical multivariable model retained useful discrimination in later accidents and materially outperformed an accident-type-only benchmark for ranking, but its absolute probabilities under predicted later events. Post hoc analyses showed that calendar-time extrapolation contributed to the discrepancy and that refitting with more contemporary data improved average calibration in later forward blocks. The strongest interpretation is therefore not that one fixed equation has been operationally validated, but that transparent consequence profiling can identify stable relative risk concentration while absolute probability models require ongoing temporal evaluation and updating.

8. AVAILABILITY AND DECLARATIONS

8.1 Data and code availability

The MARSIS public marine occurrence data and data dictionary are available from the Transportation Safety Board of Canada [3]. The analysis code and supporting numerical outputs are available from the author upon reasonable request. Analyses used R 4.2.2 with data.table 1.17.6, ggplot2 4.0.0, pROC 1.19.0.1, PRROC 1.4, and logistf 1.26.1 where required.

8.2 Ethics statement

The study used publicly released administrative occurrence records from which the TSB excludes third-party, personal, privileged, and other protected information [3]. No interaction with human participants

Journal of Marine Technology and Environment
DOI:10.53464/JMTE.02.2026.04
ISSN (Print): 1844-6116
ISSN (Online): 2501-8795
https://www. jmte.eu

occurred; institutional review board approval and informed consent were not applicable.

8.3 Funding

This research received no external funding.

8.4 Declaration of interest

The author declares no competing financial or personal interests that could have influenced the work reported in this paper.

9. CREdit authors statement DATA

Conceptualization; Methodology; Software; Validation; Formal analysis; Investigation; Data curation; Visualization; Writing - original draft; Writing - review and editing; Project administration - David O. Kremelberg.

10. REFERENCES

[1] Huang, X., Wen, Y., Zhang, F., Han, H., Huang, Y., & Sui, Z., 2023, *A review on risk assessment methods for maritime transport*, Ocean Engineering, 279, 114577. https://doi.org/10.1016/j.oceaneng.2023.114577

[2] Jin, D., Kite-Powell, H., & Talley, W. K., 2001, *The safety of commercial fishing: Determinants of vessel total losses and injuries*, Journal of Safety Research, 32(2), 209-228. https://doi.org/10.1016/S0022-4375(01)00047-0

[3] Transportation Safety Board of Canada, 2026, Marine transportation occurrence data from January 1995: MARSIS public dataset and data dictionary. https://www.tsb.gc.ca/eng/stats/marine/data-6.html (accessed 3 September 2026).

[4] Weng, J., & Yang, D., 2015, *Investigation of shipping accident injury severity and mortality*, Accident Analysis & Prevention, 76, 92-101. https://doi.org/10.1016/j.aap.2015.01.002

[5] Talley, W. K., Jin, D., & Kite-Powell, H., 2005, *Determinants of crew injuries in vessel accidents*, Maritime Policy & Management, 32(3), 263-278. https://doi.org/10.1080/03088830500139760

[6] Wang, H., Liu, Z., Wang, X., Huang, D., Cao, L., & Wang, J., 2022, *Analysis of the injury-severity outcomes of maritime accidents using a zero-inflated ordered probit model*, Ocean Engineering, 258, 111796. https://doi.org/10.1016/j.oceaneng.2022.111796

[7] Wang, H., Liu, Z., Wang, X., Graham, T., & Wang, J., 2021, *An analysis of factors affecting the severity of marine accidents*, Reliability Engineering & System Safety, 210, 107513. https://doi.org/10.1016/j.ress.2021.107513

[8] Wang, L., & Yang, Z., 2018, *Bayesian network modelling and analysis of accident severity in waterborne transportation: A case study in China*, Reliability Engineering & System Safety, 180, 277-289. https://doi.org/10.1016/j.ress.2018.07.021

[9] Li, B., Lu, J., & Li, J., 2021, *Investigation of accident severity in sea lanes from an emergency response perspective based on data mining technology*, Ocean Engineering, 239, 109920. https://doi.org/10.1016/j.oceaneng.2021.109920

[10] Fan, S., Blanco-Davis, E., Yang, Z., Zhang, J., & Yan, X., 2020, *Incorporation of human factors into maritime accident analysis using a data-driven Bayesian network*, Reliability Engineering & System Safety, 203, 107070. https://doi.org/10.1016/j.ress.2020.107070

[11] Cao, Y., Wang, X., Wang, Y., Fan, S., Wang, H., Yang, Z., Liu, Z., Wang, J., & Shi, R., 2023, *Analysis of factors affecting the severity of marine accidents using a data-driven Bayesian network*, Ocean Engineering, 269, 113563. https://doi.org/10.1016/j.oceaneng.2022.113563

[12] Liu, D., Cheng, L., Ai, B., Xie, R., Wang, X., & Shang, H., 2026, *Determinants of casualty severity in maritime accidents: Evidence from text mining of 581 investigation reports*, 2014-2023, Ocean Engineering, 351, 124456. https://doi.org/10.1016/j.oceaneng.2026.124456

[13] Khan, R. U., & Yang, Z., 2026, *Maritime accident severity modelling with operationally realistic multi-factor data-driven Bayesian networks*, Reliability Engineering & System Safety, 275, 112823. https://doi.org/10.1016/j.ress.2026.112823

[14] Duan, N., Guan, W., Wang, X., & Li, L., 2026, *An explainable ensemble learning framework for maritime accident severity and type identification: Multi-method feature selection and SHAP*

interpretation, Ocean Engineering, 363, 126776. https://doi.org/10.1016/j.oceaneng.2026.126776

[15] Cao, W., Wang, X., Feng, Y., Zhou, J., & Yang, Z., 2026, *Improving maritime accident severity prediction accuracy: A holistic machine learning framework with data balancing and explainability techniques*, Reliability Engineering & System Safety, 266, 111648. https://doi.org/10.1016/j.ress.2025.111648

[16] Shi, X., Zhuang, H., & Xu, D., 2021, *Structured survey of human factor-related maritime accident research*, Ocean Engineering, 237, 109561. https://doi.org/10.1016/j.oceaneng.2021.109561

[17] Rezaee, S., Pelot, R., & Finnis, J., 2016, *The effect of extratropical cyclone weather conditions on fishing vessel incidents' severity level in Atlantic Canada*, Safety Science, 85, 33-40. https://doi.org/10.1016/j.ssci.2015.12.006

[18] Rezaee, S., Brooks, M. R., & Pelot, R., 2017, *Review of fishing safety policies in Canada with respect to extreme environmental conditions and climate change effects*, WMU Journal of Maritime Affairs, 16(1), 1-17. https://doi.org/10.1007/s13437-016-0110-z

[19] Van Calster, B., McLernon, D. J., van Smeden, M., Wynants, L., & Steyerberg, E. W., 2019, *Calibration: The Achilles heel of predictive analytics*, BMC Medicine, 17, 230. https://doi.org/10.1186/s12916-019-1466-7

[20] Roberts, D. R., Bahn, V., Ciuti, S., Boyce, M. S., Elith, J., Guillera-Arroita, G., et al., 2017, *Cross-validation strategies for data with temporal, spatial, hierarchical, or phylogenetic structure*, Ecography, 40(8), 913-929. https://doi.org/10.1111/ecog.02881

[21] Collins, G. S., Moons, K. G. M., Dhiman, P., Riley, R. D., Beam, A. L., Van Calster, B., et al., 2024, *TRIPOD+AI statement: Updated guidance for reporting clinical prediction models that use regression or machine learning methods*, BMJ, 385, e078378. https://doi.org/10.1136/bmj-2023-078378

[22] Transportation Safety Board of Canada, 2015, Statistical summary - Marine transportation occurrences in 2014. https://www.tsb.gc.ca/eng/stats/marine/2014/ssem-ssmo-2014.html (accessed 3 September 2026).

[23] Transportation Safety Board Regulations, SOR/2014-37 (Canada), current consolidated regulations. https://laws-lois.justice.gc.ca/eng/regulations/SOR-2014-37/ (accessed 3 September 2026).

[24] Transportation Safety Board of Canada, 2026, Table 1. Marine occurrences (types, vessels and losses involved), July 2026. https://www.tsb.gc.ca/eng/stats/marine/2026/07/2026-07-t1.html (accessed 3 September 2026).

[25] Groenwold, R. H. H., White, I. R., Donders, A. R. T., Carpenter, J. R., Altman, D. G., & Moons, K. G. M., 2012, *Missing covariate data in clinical research: When and when not to use the missing-indicator method for analysis*, CMAJ, 184(11), 1265-1269. https://doi.org/10.1503/cmaj.110977

[26] Puhr, R., Heinze, G., Nold, M., Lusa, L., & Geroldinger, A., 2017, *Firth's logistic regression with rare events: Accurate effect estimates and predictions?*, Statistics in Medicine, 36(14), 2302-2317. https://doi.org/10.1002/sim.7273

[27] Riley, R. D., Snell, K. I. E., Ensor, J., Burke, D. L., Harrell, F. E., Jr., Moons, K. G. M., & Collins, G. S., 2019, *Minimum sample size for developing a multivariable prediction model: Part II - binary and time-to-event outcomes*, Statistics in Medicine, 38(7), 1276-1296. https://doi.org/10.1002/sim.7992

[28] E.Y.E. Marine Consultants, n.d., Henry Nace / William Pitt II / RGL Fairweather, vessel particulars. https://www.eyemarine.com/vessel/henry-nace-william-pitt-ii-rgl-fairweather/ (accessed 5 September 2026).

[29] Steyerberg, E. W., Vickers, A. J., Cook, N. R., Gerds, T., Gonen, M., Obuchowski, N., Pencina, M. J., & Kattan, M. W., 2010, *Assessing the performance of prediction models: A framework for traditional and novel measures*, Epidemiology, 21(1), 128-138. https://doi.org/10.1097/EDE.0b013e3181c30fb2

[30] Eliopoulou, E., Alissafaki, A., & Papanikolaou, A., 2023, *Statistical analysis of accidents and review of safety level of passenger ships, Journal of Marine Science and Engineering*, 11, 410. https://doi.org/10.3390/jmse11020410

[31] Demirci, S. M. E., & Cicek, K., 2022, *Deficiency analysis identified in PSC inspections using event tree analysis*, Journal of Marine Technology and Environment, 2022(1), 40-46. https://doi.org/10.53464/JMTE.01.2022.05

Journal of Marine Technology and Environment
DOI:10.53464/JMTE.02.2026.05
ISSN (Print): 1844-6116
ISSN (Online): 2501-8795
https://www. jmte.eu

FUNCTIONAL DIAGNOSIS AND ANALYSIS OF THE MANIFOLD ABSOLUTE PRESSURE SENSOR IN TURBOCHARGED COMPRESSION-IGNITION ENGINES

Bogdan-Cristian MANDACHE[1], Traian DORDEA [1] & Gabriela IANCULESCU [2]

[1]" Ovidius" University of Constanța,, Faculty of Mechanical, Industrial and Maritime Engineering, 124 Mamaia Street, 900527, Constanta, Romania, e-mail address:traiandordea@yahoo.com; body_crys12@yahoo.com

Abstract : This paper presents the diagnosis and functional analysis of the MAP sensor used in turbocharged Diesel engines. The experimental study was conducted using the VCDS diagnostic platform through real-time monitoring and analysis of engine operating parameters under actual vehicle operating conditions. The obtained values were analysed in real time in order to evaluate the operation of the sensor and the turbocharging system
Key words : Combustion, diagnosis, MAP (Manifold Absolute Pressure), optimization, turbocharged compression-ignition engine, sensor, verification.

1. INTRODUCTION

Modern Diesel engines use advanced electronic systems to control turbocharger pressure and optimize the combustion process. Within these systems, the MAP sensor (Manifold Absolute Pressure) is responsible for transmitting the intake manifold pressure values to the ECU unit. This information is used for fuel injection adjustment, variable geometry turbocharger control, and engine performance monitoring.

Improper operation of the MAP sensor may lead to power loss, limp mode operation, increased fuel consumption, and the occurrence of turbocharging-related faults. For this reason, the correct analysis and diagnosis of this sensor represent an important stage in the verification of modern electronic management systems used in Diesel engines.

2. MATERIALS AND EXPERIMENTAL METHODS

During the experimental study, the VCDS diagnostic platform was used together with the communication interface connected to the vehicle ECU, in order to monitor the turbocharging system parameters and identify possible operating faults.[1] The parameter values were monitored in real time and compared with the values calculated by the engine control unit.

The experimental investigations were carried out on a 2016 Audi A7 powered by a 3.0 TDI V6 compression-ignition engine (CVUA engine code) rated at 320 HP (235 kW), equipped with a Bosch EDC17 electronic engine management system.[2] The turbocharging system is electronically controlled and continuously monitored by the ECU through the VCDS diagnostic platform.[3]

In the first stage of the experiment, measurements were performed at idle speed in order to determine the baseline values of the intake manifold pressure and verify the stable operation of the MAP sensor. Using the VCDS software, the actual pressure values, calculated pressure values, sensor voltage, and turbocharger actuator activation were monitored.

In the second stage, measurements were carried out under load conditions at an engine speed of approximately 2600 rpm in order to observe the variation of the boost pressure during acceleration. The obtained data allowed the comparison between the ECU-requested values and the actual values measured by the MAP sensor, as well as the analysis of the turbo system response depending on the engine operating regime.[4]

The VCDS platform (*VAG-COM Diagnostic System*) represents an advanced diagnostic system used for vehicles belonging to the VAG group. The tester allows real-time parameter reading, sensor value

Journal of Marine Technology and Environment
DOI:10.53464/JMTE.02.2026.05
ISSN (Print): 1844-6116
ISSN (Online): 2501-8795
https://www.jmte.eu

monitoring, dynamic data logging, and analysis of the operation of electronic engine components. *The Advanced Measuring Values* function enabled the comparison between ECU-calculated parameters and the actual measured values during engine operation both at idle and under load conditions (Figure 1, Figure 2, Figure 3, Figure 4).[5]

Figure 1 Experimental diagnosis performed on the vehicle using the VCDS platform

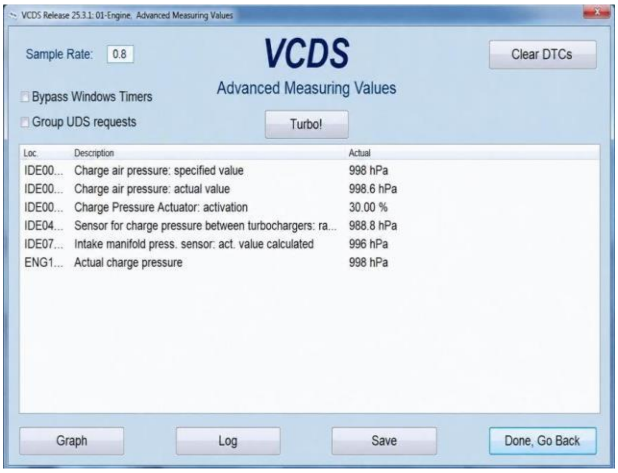

Figure 2 MAP parameter values measured at idle using the VCDS interface

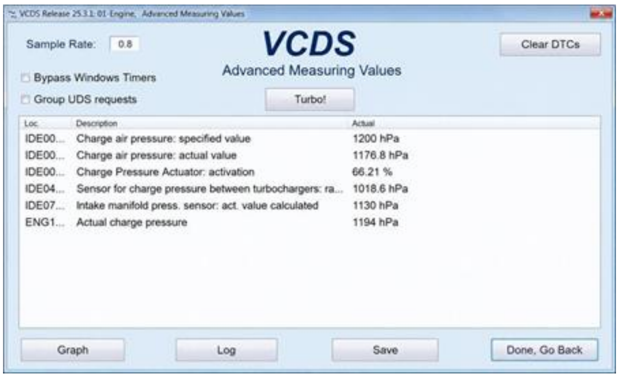

Figure 3 MAP parameter values under load at approximately 2600 rpm

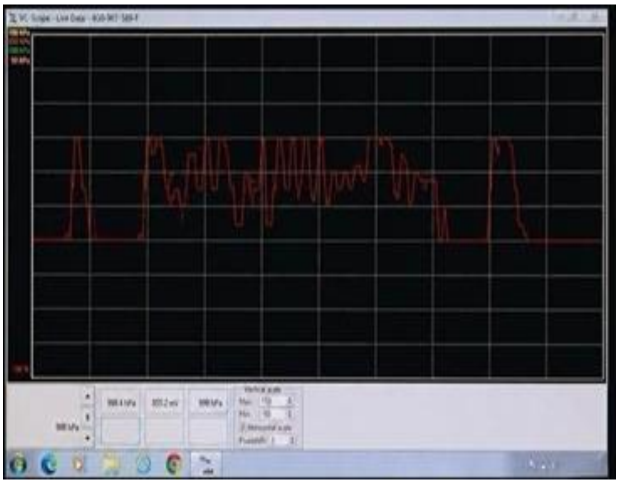

Figure 4 Real-time graphical analysis of turbocharging system parameters

Diagram interpretation:

From a functional point of view, the graph obtained using the oscilloscope-type function in VCDS shows the way in which the turbocharging system responds to ECU requests. The monitored signal highlights the variation in intake pressure and turbocharger actuator command during changes in engine operating conditions. The rapid increases in the curve indicate moments when the turbocharger is requested to increase pressure, while the more stable areas indicate pressure maintenance close to the requested value.The absence of sudden drops or excessive oscillations confirms that the MAP sensor transmits a coherent signal and that the turbocharger actuator responds correctly to the electronic command.

Journal of Marine Technology and Environment
DOI:10.53464/JMTE.02.2026.05
ISSN (Print): 1844-6116
ISSN (Online): 2501-8795
https://www. jmte.eu

Thus, the diagram confirms a normal correlation between the measured pressure, requested pressure, and turbocharging system command percentage (Figure 5).

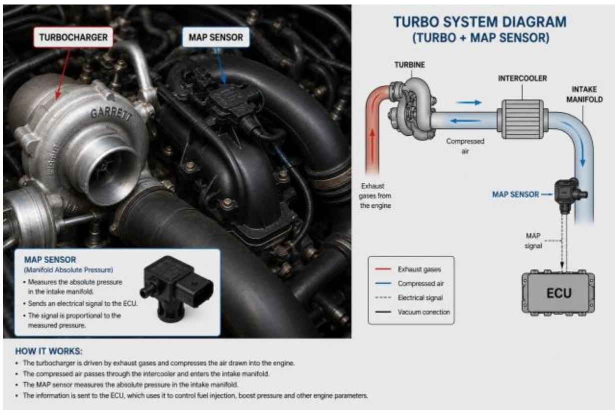

Figure 5 Functional diagram of the turbocharging system and MAP sensor positioning within the intake circuit

3. RESULTS AND DISSCUTIONS

The measurements performed using the VCDS software indicated stable operation of the MAP sensor both at idle and under load conditions. At idle, the measured pressure values remained close to atmospheric pressure, confirming the correct operation of the sensor and its monitoring system.

During the tests performed at approximately 2600 rpm, an increase in turbocharging pressure and variation in turbocharger actuator activation were observed. The values recorded through VCDS highlighted the rapid response of the turbo system and the stability of the signal transmitted by the MAP sensor.

To highlight the differences between engine operation at idle and under load conditions, the values of the main parameters monitored through VCDS were centralized in the following table.

Analysing the values presented in the Table 1, the difference between engine operation at idle and under load conditions can be observed. At idle, the actual and calculated MAP pressure values are close to atmospheric pressure, indicating stable intake system operation and reduced turbocharger demand. Under load conditions, at approximately 2600 rpm, an increase in MAP pressure and turbocharger actuator activation percentage can be observed, confirming the turbo system response to ECU requests.

Table 1. Comparison of turbocharging system parameters at idle and under load

Monitored parameter	Idle	Load (~2600rpm)
Actual MAP pressure	998 hPa	1197 hPa
Calculated MAP pressure	994 hPa	1121 hPa
MAP sensor voltage	0.85 V	0.88 V
Turbocharged actuator activation	30%	68.47%
Engine speed	850 rpm	~2600 rpm
Operating conditions	Stable conditions	Increase in turbo pressure

The recorded data highlighted an effective pressure of approximately 1197 hPa and a calculated intake manifold pressure value of approximately 1121 hPa. The turbocharger actuator activation reached approximately 68 %, while the MAP sensor voltage remained stable between approximately 0.85 V at idle and 0.88 V under load conditions. The limited variation of the sensor voltage confirms the stable electrical behaviour of the MAP sensor and the correct conversion of pressure values into electrical signals transmitted to the ECU.

The values presented in Table 1 represent the representative operating values recorded during the load test performed at approximately 2600 rpm. The values displayed in Figure 3 correspond to a specific acquisition moment captured during the dynamic measurement process. Small differences between the numerical values shown in the table and those visible in the VCDS screenshot are caused by the continuous variation of boost pressure during engine operation and by the real-time sampling rate of the diagnostic platform.

From a diagnostic perspective, the values obtained during the experimental tests indicate normal operation of the MAP sensor and turbocharging system. However, in practical applications, several failure modes may affect the sensor performance and lead to incorrect

Journal of Marine Technology and Environment
DOI:10.53464/JMTE.02.2026.05
ISSN (Print): 1844-6116
ISSN (Online): 2501-8795
https://www. jmte.eu

pressure measurements. One of the most common faults is signal drift, where the sensor gradually deviates from its calibrated values, causing discrepancies between the actual and ECU-calculated boost pressure. Electrical faults such as short circuits, open circuits, or unstable supply voltage may also generate implausible sensor readings and trigger diagnostic trouble codes. Another relevant failure mode is delayed sensor response during transient operating conditions, where the MAP sensor reacts slower than expected to rapid pressure changes caused by acceleration or turbocharger activation. Such behaviour may lead to inaccurate boost pressure control and reduced engine performance.

The stable values obtained during the present study, together with the absence of abnormal fluctuations in the recorded signals, indicate that none of these failure modes were present during the experimental tests.[6]

4. CONCLUSIONS

The conclusions obtained following the experimental tests confirm the correct operation of the MAP sensor and the analysed turbocharging system. The values monitored through the VCDS platform highlighted an appropriate correlation between the pressure requested by the ECU unit and the actual pressure measured in the intake manifold, both at idle and under load conditions at approximately 2600 rpm.

At idle, the MAP pressure values remained close to atmospheric pressure, while the turbocharger actuator activation percentage had low values, indicating minimal demand on the turbo system.

Under load conditions, an increase in turbocharging pressure and turbocharger actuator command percentage was observed, demonstrating the correct system response to engine operating requirements.

The analysis of the recorded values and the interpretation of the diagram obtained using the VC-Scope function highlighted the stability of the signal transmitted by the MAP sensor and the absence of abnormal intake pressure fluctuations.

The small differences between the actual values and those calculated by the ECU confirm the proper operation of the sensor and the efficiency of the electronic turbocharger control system.

The use of the VCDS platform proved effective for monitoring intake system parameters and for the rapid diagnosis of possible turbocharging system faults. The method used in this paper may represent a practical basis for future studies regarding the analysis of sensors used in the electronic management of modern Diesel engines.

5. CREdit authors statement

Conceptualization: M.B.-G., D.T, I.G;

Data curation; M.B.-G., D.T, I.G;

Formal analysis: M.B.-G., D.T, I.G;

Funding acquisition: not applicable;

Investigation: M.B.-G., D.T, I.G;

Methodology: M.B.-G., D.T, I.G;

Project administration: D.T;

Resources: M.B.-G., D.T, I.G;

Software: M.B.-D., D.T;

Supervision :D.T.;

Validation: M.B.-D., D.T;

Visualization: M.B.-D., D.T;

Writing – original draft: M.B.-D., D.T;

Writing – review & editing:. M.B.-D., D.T.

6. REFERENCES

[1] Robert Bosch GmbH, *Diesel-Engine Management*, 2nd ed., Society of Automotive Engineers (SAE), Warrendale, ISBN: 978-0768005097, PA, USA, 1999.

[2] V. S. Jagtap et al., "*Diagnostics Methodology for Turbocharger System Using Data-Driven Models*," SAE Technical Paper 2025-28-0404, SAE International, 2025.

[3] Ross-Tech LLC, *VCDS Diagnostic Manual and User Guide*, Ross-Tech, available online: Ross-Tech VCDS Manual (accessed May 2026).

Journal of Marine
Technology and Environment
DOI:10.53464/JMTE.02.2026.05

ISSN (Print): 1844-6116
ISSN (Online): 2501-8795
https://www. jmte.eu

[4] James E. Duffy, *Modern Automotive Technology*, 10th ed., Goodheart-Willcox Publisher, ISBN: 978-1645646884, Tinley Park, IL, USA, 2020.

[5] https://en.wikipedia.org/wiki/VCDS_(software)

[6] https://www.gendan.co.uk/vcds-v2.php

[7] Bohoz, A., *Elaboration and testing of laboratory stand for investigation of an arc fault detection device*, Journal of Marine Technology and Environment, vol. 1, pp 11-16, 2016.

Journal of Marine Technology and Environment
DOI:10.53464/JMTE.02.2026.06
ISSN (Print): 1844-6116
ISSN (Online): 2501-8795
https://www.jmte.eu

REPURPOSING THE VESSEL EXPERIENCE FACTOR AS A STATISTICAL PROCESS CONTROL TOOL FOR TANKER CARGO MEASUREMENT

Valentin-Adrian MIRON[1], Andrei PREDA[1] & Nicoleta ACOMI[1]

[1] Constanta Maritime University, Faculty of Navigation and Naval Transport, 104 Mircea cel Batran Street, 900663, Constanta, Romania, e-mail: valentinmiron156@yahoo.com
2 Constanta Maritime University, Faculty of Marine Engineering, 104 Mircea cel Batran Street, 900663, Constanta, Romania, e-mail: andrei.preda@cmu-edu.eu
[1] Constanta Maritime University, Faculty of Navigation and Naval Transport, 104 Mircea cel Batran Street, 900663, Constanta, Romania, ORCID: https://orcid.org/0000-0003-3564-6867, e-mail: nicoleta.acomi@cmu-edu.eu

Abstract: Accurate reconciliation of cargo quantities measured on board a tanker with those declared by shore terminals is central to reliable tanker operations and to the prevention of commercial disputes. The Vessel Experience Factor (VEF), provides a historical, vessel-specific relationship between shipboard and shore measurements and is traditionally used as a cargo-reconciliation and loss-control tool. This paper investigates whether the same historical VEF population can additionally support the statistical quality control of the ship/shore measurement process itself. A case study was carried out using operational data from 23 consecutive loading operations of a medium-range product/chemical tanker, covering nine cargo grades and fifteen terminals. For each voyage, the Ship/Shore Ratio was computed and compared with unity, with the vessel's historical VEF and with a ±0.3% tolerance band reinterpreted as Shewhart-type control limits. Descriptive statistics, a normality check and an individuals control chart were used to assess the stability of the measurement process and to identify voyages departing from the vessel's established behaviour. The historical VEF was 0.99947 (n = 20 qualified voyages), all 23 ratios remained inside the ±0.3% band, and a five-voyage window (voyages 241-246) revealed two short downward runs separated by a partial recovery - a pattern invisible to a simple per-voyage tolerance check. The results show that VEF data, already collected for commercial reasons, can be repurposed at no additional cost into a vessel-specific quality-control indicator that complements, rather than replaces, conventional cargo reconciliation.

Keywords: Cargo reconciliation; Quality control; Ship/Shore ratio; Statistical process control; Tanker cargo measurement; Vessel Experience Factor.

1. INTRODUCTION

Seaborne trade continues to move the overwhelming majority of the world's liquid energy cargoes, and product and crude oil tankers remain the backbone of this logistical chain. On every laden voyage, the quantity of cargo transferred between a shore terminal and a vessel is determined twice, independently, by two measurement systems that rarely agree perfectly: the terminal's tank gauges or mass-flow meters, and the vessel's own calibrated tank tables read through Ullage, Temperature and Interface (UTI) probes or fixed radar gauges [2],[3]. The resulting "ship figures" and "shore figures" are reconciled at the close of every cargo operation, and the discrepancy between them - however small - is one of the most frequent triggers of commercial disputes between shipowners, charterers and terminal operators.

The industry's principal instrument for managing this discrepancy is the Vessel Experience Factor (VEF), formalised by the American Petroleum Institute in the Manual of Petroleum Measurement Standards (MPMS), Chapter 17.9 / Energy Institute HM 49 [1]. VEF condenses the historical ship/shore performance of an individual vessel, typically over its last 20 or more qualifying voyages, into a single correction coefficient applied to future Bills of Lading to separate the vessel's own systematic bias from genuine cargo loss. In this original conception, VEF answers a commercial question - how much cargo is really missing - rather than an engineering one: is the measurement process itself in a state of statistical control.

Journal of Marine Technology and Environment
DOI:10.53464/JMTE.02.2026.06
ISSN (Print): 1844-6116
ISSN (Online): 2501-8795
https://www. jmte.eu

This paper argues that the second question is equally important, and that the historical VEF data set already collected by every tanker for commercial reasons can be repurposed, at no additional operational cost, into a quality-control instrument for the ship/shore measurement process. Framed in the language of statistical process control (SPC), the vessel-specific VEF becomes a process centre line, its ±0.3% commercial tolerance becomes a pair of control limits, and every new voyage becomes an individual observation to be plotted, monitored for drift and investigated when it strays. This turns cargo reconciliation - traditionally a retrospective, voyage-by-voyage commercial exercise - into a prospective, statistically grounded quality-control routine that a Chief Officer can run from the cargo office with data already generated for other purposes.

The remainder of the paper is organised as follows. Section 2 reviews the regulatory and theoretical background of tanker cargo measurement and the VEF methodology, and situates the proposed approach within the wider statistical process control literature. Section 3 describes the case-study vessel, the operational data set and the statistical methods applied. Section 4 reports the results for 23 consecutive loading operations, including an individuals control chart and a distributional assessment. Section 5 discusses the practical and methodological implications, and Section 6 concludes with recommendations for onboard practice and directions for further research. Related tanker-safety and tanker-efficiency studies have previously been reported in this journal, addressing port-state-control deficiency analysis [10] and energy-efficiency trends on large crude carriers [11], underscoring the continued relevance of tanker-specific operational research.

2. REGULATORY AND THEORETICAL BACKGROUND

2.1 Cargo measurement and custody transfer on tank vessels

On a product or crude oil tanker, the quantity of liquid cargo loaded or discharged is never weighed directly; it is reconstructed from a sequence of volumetric and physical measurements standardised by the American Petroleum Institute through the Manual of Petroleum Measurement Standards (MPMS) and by the American Society for Testing and Materials [3],[4], and operationally framed by the International Safety Guide for Oil Tankers and Terminals (ISGOTT) [2]. For each cargo tank, a UTI probe or fixed radar gauge yields the observed ullage, corrected for trim and list to obtain the Total Observed Volume (TOV) through the ship's calibration tables. Free water is subtracted to obtain the Gross Observed Volume (GOV), which is converted to the Gross Standard Volume (GSV) at the reference temperature of 15°C using the Volume Correction Factor obtained from the ASTM tables on the basis of density and observed temperature [4]. The GSV is finally converted into metric tons in air, the unit used commercially, through the standard air-buoyancy correction. Every step of this chain - the Ullage Report, the On-Board-Quantity and Remaining-On-Board surveys and the Bill of Lading - is retained on board as part of the Oil Record Book, Part II, required under MARPOL 73/78, Annex I [5], and forms the documentary basis on which cargo disputes are ultimately settled.

2.2 The Vessel Experience Factor as a loss-control instrument

Because the ship's tanks are calibrated by the shipyard under idealised conditions, while the vessel operates under continuously varying trim, list, structural deflection and sediment loading, a small, largely constant bias between ship and shore figures is expected even when both measurement systems function correctly. API MPMS Chapter 17.9 / EI HM 49 formalises the Vessel Experience Factor as the tool that isolates this vessel-specific bias from genuine cargo loss [1]. VEF is defined as the ratio of the cumulative ship-measured volume to the cumulative shore-measured (Bill of Lading) volume over the vessel's last minimum of 20 qualifying voyages carrying similar cargo grades:

$$\mathrm{VEF} = \frac{\sum_{i=1}^{n} V_{\mathrm{ship},i}}{\sum_{i=1}^{n} V_{\mathrm{shore},i}} \tag{1}$$

A voyage qualifies for inclusion in this historical population only if it is not a part cargo (loaded below 75% of tank capacity), is not a ship-to-ship (STS) transfer, and its individual Ship/Shore Ratio does not fall outside a control band of approximately ±0.3% around the vessel's running average [1]. For any subsequent voyage, the Ship/Shore Ratio is computed as

$$\text{Ship/Shore Ratio} = \frac{\text{Ship TCV}}{\text{Shore B/L TCV}} \tag{2}$$

where Ship TCV is the Total Calculated Volume determined on board immediately after loading (or

Journal of Marine Technology and Environment
DOI:10.53464/JMTE.02.2026.06
ISSN (Print): 1844-6116
ISSN (Online): 2501-8795
https://www. jmte.eu

before discharge) and Shore B/L TCV is the corresponding volume declared on the Bill of Lading. When the current voyage's ratio, once corrected by the vessel's historical VEF, still departs from unity by more than the contractually agreed tolerance - typically 0.3% under a standard Charter Party - the Chief Officer is obliged to issue a Letter of Protest to preserve the owner's position against a subsequent cargo-shortage claim.

2.3 From loss control to statistical quality control

Read purely as a loss-control ratio, VEF answers a single, retrospective, per-voyage question. Read as a time-ordered sequence, however, the same 20 or more historical Ship/Shore ratios are formally indistinguishable from the individual measurements plotted on a Shewhart control chart, the foundational SPC tool introduced by Shewhart [6] and developed into its modern form by Montgomery [7]: a centre line (the process average, here the historical VEF), upper and lower control limits (here the ±0.3% commercial tolerance) and a sequence of individual observations screened for out-of-control points, run patterns and gradual drift. This reinterpretation is not merely semantic. A control-chart view distinguishes between situations that a raw voyage-by-voyage comparison against unity cannot: ordinary common-cause variation around the vessel's own baseline; an assignable-cause signal at a single voyage; and a sustained, unidirectional drift across several consecutive voyages, the classical SPC signature of a slowly developing measurement fault rather than of a single erroneous reading.

Related work has approached the reliability of tanker cargo custody transfer from complementary angles. Meškuotienė et al. [9] analysed the metrological uncertainty of liquid-level gauging in cylindrical storage tanks, and Senol [8] modelled the human-factor contribution to chemical-cargo shortage incidents using fuzzy fault-tree analysis. To the authors' knowledge, however, the historical VEF population itself has not previously been analysed as a control-chart data set for onboard quality assurance, which is the specific contribution of the present study, building on prior operational case analysis conducted by the lead author during his sea-going assignment.

3. MATERIALS AND METHODS

3.1 Case-study vessel and data set

The empirical analysis uses operational cargo-measurement data collected on board a medium-range (MR) product/chemical tanker of approximately 40,000 DWT, compiled by the lead author during a six-month sea-going assignment as Second Officer. The data set comprises 23 consecutive laden voyages (internal voyage numbers 232 to 254), spanning loading operations at fifteen terminals in the Mediterranean, Black Sea, North Sea, Atlantic and Red Sea areas and covering nine clean-petroleum-product grades (unleaded gasoline, Jet A-1, ultra-low-sulphur diesel, gas oil, naphtha and reformate/gasoline blends). For every voyage, the ship-measured Total Calculated Volume and the corresponding Bill-of-Lading volume were extracted from the vessel's Ullage Reports and cargo documents and centralised in the vessel's onboard VEF record.

3.2 Variables and eligibility screening

For each voyage, the Ship/Shore Ratio and the percentage difference , 100 × (Ship TCV−Shore TCV) / Shore TCV, were computed. Voyages were flagged as qualified or excluded from the VEF calculation following the eligibility criteria of API MPMS 17.9 [1]: three voyages (nos. 242, 243 and 250) were STS transfers and were excluded, leaving n = 20 qualified voyages for the calculation of the vessel's historical VEF. All 23 voyages, including the three excluded ones, were retained for the descriptive and distributional analysis, since their measurement behaviour remains informative about the operational envelope of the ship/shore comparison even though it is not used to define the vessel's baseline.

3.3 Statistical analysis

The historical VEF was computed according to Eq. (1) over the 20 qualified voyages, and the corresponding ±0.3% control band was established around the aggregate ratio computed over all 23 voyages, consistent with the vessel's own onboard practice. The 23 individual Ship/Shore ratios were then plotted, in chronological order, as an individuals (Shewhart X) control chart against this centre line and control limits, and screened for points outside the ±0.3% band, for the most extreme voyages, and for runs of consecutive same-direction departures indicative of drift. Descriptive statistics of the percentage difference were computed separately for the full sample (n = 23) and the qualified sample (n = 20), and the normality of the qualified sample was assessed with the Shapiro-Wilk test, a

Journal of Marine
Technology and Environment
DOI:10.53464/JMTE.02.2026.06
ISSN (Print): 1844-6116
ISSN (Online): 2501-8795
https://www. jmte.eu

standard precondition check before treating a small sample as consistent with the Gaussian assumptions implicit in classical Shewhart limits [7].

4. RESULTS

4.1 Data set and Ship/Shore ratio

Table 1 summarizes the ship-measured Total Calculated Volume, the Bill-of-Lading volume declared by the shore terminal, the resulting Ship/Shore ratio and the API MPMS 17.9 qualification status for each of the 23 voyages analysed, together with the totals used in the aggregate VEF calculation of Eq. (1).

Table 1. Ship/Shore cargo reconciliation data from the case-study vessel - 23 consecutive loading operations

No.	Voy.	Product	Load port	Ship TCV (m^3)	Shore B/L TCV (m^3)	Ship/Shore ratio	Diff. (%)	Qual.
1	232	Unleaded Gasoline	Midia	32,728.462	32,755.180	0.99918	-0.082	Yes
2	233	Gasoline 95 RON	Bourgas	40,109.140	40,146.298	0.99907	-0.093	Yes
3	234	Unleaded Gasoline	Midia	32,051.080	32,063.503	0.99961	-0.039	Yes
4	235	Gas Oil 10 ppm	Sidi Kerir	39,866.990	39,902.387	0.99911	-0.089	Yes
5	236	ULSD 10 ppm	El Dekheila	37,478.605	37,495.010	0.99956	-0.044	Yes
6	237	Unleaded Gasoline	Bourgas	30,029.018	30,016.572	1.00041	+0.041	Yes
7	238	Unleaded Gasoline	Aspropyrgos	26,920.517	26,940.794	0.99925	-0.075	Yes
8	239	Unleaded Gasoline 95	Thessaloniki	32,930.169	32,915.065	1.00046	+0.046	Yes
9	240	ULSD 10 ppm	Sidi Kerir	30,670.872	30,723.675	0.99828	-0.172	Yes
10	241	ULSD 10 ppm	Sidi Kerir	32,485.938	32,493.192	0.99978	-0.022	Yes
11	242	JET A1	STS OPL Ceuta	26,420.864	26,431.635	0.99959	-0.041	No
12	243	ULSD 10 ppm	STS Gibraltar	34,892.759	34,931.158	0.99890	-0.110	No
13	244	Naphtha	Bilbao	31,583.681	31,603.260	0.99938	-0.062	Yes
14	245	ULSD 10 ppm	Antwerp	32,908.125	32,924.124	0.99951	-0.049	Yes
15	246	Gasoline 98RON/Eurobob	Amsterdam	25,381.375	25,443.972	0.99754	-0.246	Yes
16	247	Reformate/Gasoline C7	Lavera	30,423.045	30,413.835	1.00030	+0.030	Yes
17	248	Unleaded Gasoline 95 RON	Antwerp	32,613.266	32,635.530	0.99932	-0.068	Yes
18	249	Gasoline	Sarroch	32,484.214	32,411.372	1.00225	+0.225	Yes
19	250	ULSD 10 ppm	STS OPL Limassol	27,944.248	27,933.535	1.00038	+0.038	No
20	251	Unleaded Gasoline 95 RON	Vassiliko	29,908.892	29,932.193	0.99922	-0.078	Yes
21	252	Unleaded Gasoline 95 RON	Agioi Theodoroi	44,544.945	44,599.288	0.99878	-0.122	Yes
22	253	JET A1	Aliaga	41,661.189	41,646.448	1.00035	+0.035	Yes
23	254	Unleaded Gasoline 95 RON	Antwerp	44,742.369	44,820.465	0.99826	-0.174	Yes
		TOTAL (n=23)		**770,779.763**	**771,178.491**	**0.99948**	**-0.052**	-
		Qualified VEF (n=20, Eq. 1)		681,521.892	681,882.163	**0.99947**	-	-

Journal of Marine
Technology and Environment
DOI:10.53464/JMTE.02.2026.06
ISSN (Print): 1844-6116
ISSN (Online): 2501-8795
https://www. jmte.eu

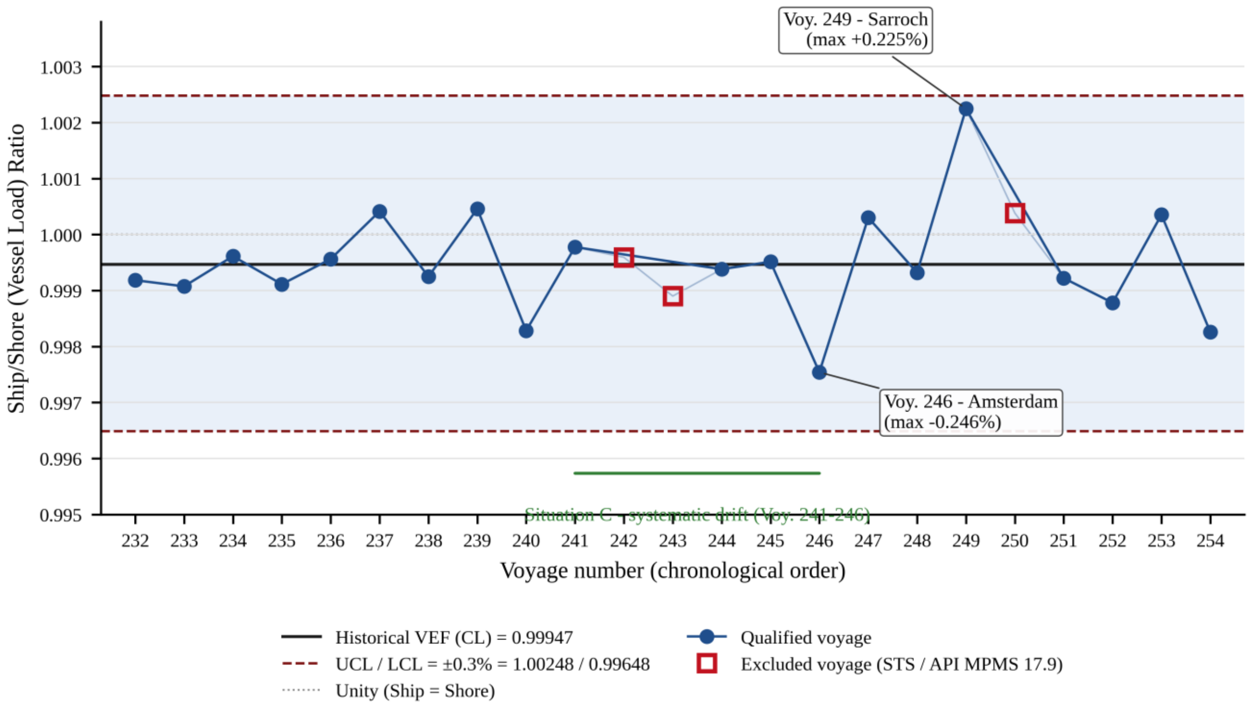

Figure 1 Individuals control chart of the Ship/Shore ratio for 23 consecutive loading operations of the case-study vessel, with centre line at the qualified VEF (0.99947) and ±0.3% control limits [1]

4.2 Vessel Experience Factor and process center line

Over the 20 qualified voyages, the aggregate historical VEF was 0.99947 (ΣShip TCV = 681,521.892 m³; ΣShore TCV = 681,882.163 m³), i.e. the vessel measured on average about 0.053% less cargo than declared by the shore terminals - a bias well inside the ±0.3% commercial tolerance and consistent with the small, structurally driven under-reading typically expected from an MR product tanker of this tank geometry. Over all 23 voyages the aggregate ratio was 0.99948, confirming that the three STS voyages excluded on eligibility grounds did not materially bias the vessel's overall measurement behaviour; they were excluded for procedural, not statistical, reasons. The mean of the 20 qualified percentage differences was -0.052% (s = 0.099%), closely matching the full-sample mean of -0.050% (s = 0.095%, n = 23), and a Shapiro-Wilk test on the qualified sample did not reject normality (W = 0.933, p = 0.178), supporting the use of Gaussian-based control limits for this data set.

4.3 Control-chart analysis

Figure 1 plots the 23 Ship/Shore ratios in chronological order against the qualified VEF centre line and the ±0.3% control band. All 23 voyages fall inside the band. Voyage 249 (Sarroch, +0.225%) came closest to the upper control limit, a departure attributed in the source record to line-pack effects and transient micro-foaming at high loading rates; voyage 246 (Amsterdam, -0.246%) recorded the largest negative departure, about 0.1 percentage points inside the lower limit, associated with the flashing of light hydrocarbon fractions from a gasoline/Eurobob blend measured by shore mass-flow meters. Neither point constitutes a formal out-of-control signal, but both fall in the region that API MPMS 17.9 identifies as warranting re-verification of ullage, temperature, density and trim/list corrections before the Bill of Lading is signed [1].

A closer inspection of voyages 241-246 - flagged in the source operational record as a single continuous downward trend - shows a more nuanced pattern: a three-voyage downward run from voyage 241 to voyage 243 (0.99978 → 0.99959 → 0.99890), a two-voyage partial recovery to voyage 245 (0.99938 → 0.99951), and a further sharp drop at voyage 246 (0.99754). Neither individual run reaches the six-point length conventionally required by the Western Electric/Nelson rules to declare a formal trend signal [7], so no alarm would have been triggered under strict SPC criteria; nevertheless, the coincidence of two short downward runs within a five-voyage window is operationally noteworthy and illustrates the diagnostic value of visual

Journal of Marine
Technology and Environment
DOI:10.53464/JMTE.02.2026.06
ISSN (Print): 1844-6116
ISSN (Online): 2501-8795
https://www. jmte.eu

control-chart inspection even below formal alarm thresholds, and is more consistent with two distinct assignable causes than with a single progressive drift mechanism such as continuous sediment accumulation.

4.4 Distribution of the Ship-Shore difference

Figure 2 shows the distribution of the percentage difference between ship and shore figures for all 23 voyages, together with a fitted normal density and the ±0.3% tolerance lines. The distribution is unimodal and reasonably symmetric around a small negative mean, with no observations approaching the ±0.3% boundary from either side; the three STS voyages excluded from the VEF calculation (hatched bars) are distributed similarly to the qualified population rather than forming a separate cluster, which supports treating their exclusion as a procedural rather than a statistical adjustment.

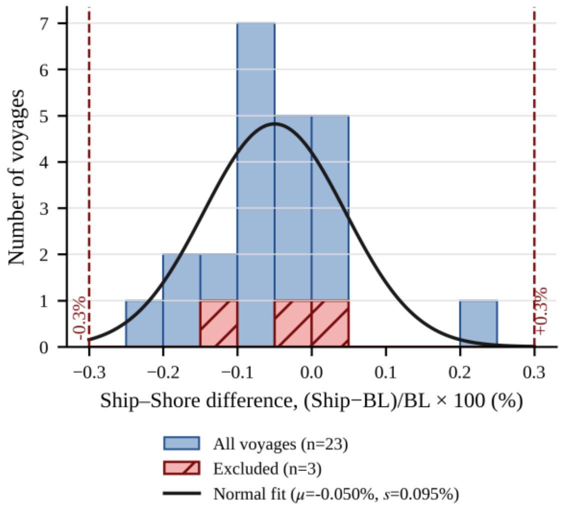

Figure 2 Distribution of the Ship-Shore percentage difference for 23 voyages, with a fitted normal density (μ = -0.050%, s = 0.095%) and the ±0.3% tolerance lines.

5. DISCUSSION

The case study demonstrates that a data set collected purely for commercial loss-control purposes can be read, without any additional instrumentation or data collection, as a small but genuine SPC data set. The clearest illustration of the added value of this reframing is the 241-246 window: none of the five voyages individually breached the ±0.3% tolerance, so a conventional per-voyage reconciliation check would have raised no flag at any point in the sequence, yet the control-chart view highlights two short, directionally consistent runs that would be worth a documented investigation - re-checking ullage readings, temperature stratification, density correlation and trim/list corrections - well before any single voyage approaches the tolerance limit.

Several limitations should be acknowledged. The analysis is based on a single vessel over a one-year operating window, so the results describe the measurement behaviour of that vessel rather than of the product-tanker fleet in general; extending the approach to a multi-vessel, pooled data set is a natural next step. The sample size (n = 20-23) is modest relative to the minimum of about 25 individual observations conventionally recommended for estimating stable Shewhart control limits [7], and consecutive voyages of the same vessel are unlikely to be fully independent, since they share instrumentation, calibration tables and often crew - a form of serial dependence that classical control-chart theory does not assume. The Shapiro-Wilk result and the run-length argument in Section 4.3 should therefore be read as indicative screening tools rather than as confirmatory hypothesis tests. It is also worth noting that all three STS voyages excluded under the API MPMS 17.9 eligibility rule in fact fell inside the ±0.3% band (Section 4.4); while the procedural exclusion of STS transfers from the baseline calculation remains prudent given the additional third-party measurement involved, this observation suggests that, for a modern tanker with redundant radar/UTI gauging, the exclusion may be conservative - an empirically testable question on a larger sample.

The proposed approach is complementary to, rather than competitive with, other strands of tanker-measurement research. Meškuotienė et al. [9] address the instrument-level metrological uncertainty of liquid-level gauging, and Senol [8] addresses the human and organisational contribution to cargo-shortage incidents through fault-tree analysis; the present study adds an intermediate, operational layer, using data that every tanker already generates, to monitor whether the ship/shore measurement process for a specific vessel remains statistically stable over time. In practice, the approach requires no more than plotting each new voyage's ratio against the standing VEF baseline and its ±0.3% band, and flagging any run of three or more consecutive voyages moving in the same direction - a check that can be implemented in a simple spreadsheet or in the cargo-calculation software already carried on board, since the underlying figures are already generated for the Letter-of-Protest and VEF-update process.

6. CONCLUSIONS

This study repurposed the Vessel Experience Factor, a long-established cargo-reconciliation and loss-

Journal of Marine Technology and Environment
DOI:10.53464/JMTE.02.2026.06
ISSN (Print): 1844-6116
ISSN (Online): 2501-8795
https://www. jmte.eu

control instrument, as a lightweight statistical process-control indicator for the ship/shore cargo-measurement process. Using 23 consecutive loading operations of an product/chemical tanker, the historical VEF (0.99947 over 20 qualified voyages) was shown to be fully compatible with the vessel's own ±0.3% commercial tolerance acting as Shewhart-type control limits, with all 23 voyages remaining inside the band and the sample distribution consistent with normality. The individuals control chart identified a genuine, if modest, five-voyage episode of directional drift that was not visible to a conventional single-voyage tolerance check, illustrating the practical value of the proposed reframing. Because the required data are already generated for commercial reconciliation purposes, routine control-chart monitoring of the Ship/Shore ratio can be adopted by ships' staff at essentially no additional cost. Future work should extend the analysis to a multi-vessel, fleet-level data set to test the generality of the observed behaviour, apply more sensitive charts such as EWMA or CUSUM to the small sustained drifts identified here, and explore integration of the proposed monitoring scheme into digital cargo-management and loss-control software.

7. CREDIT AUTHORS STATEMENT DATA

Conceptualization: N.A.; Methodology: A.P.; Software: V.A.M.; Validation: V.A.M.; Formal analysis: N.A.; Investigation: V.A.M.; Data curation: A.P.; Visualization: A.P.; Writing - original draft: V.A.M. and N.A; Writing - review and editing: A.P

8. REFERENCES

[1] American Petroleum Institute (API) / Energy Institute, 2019, Manual of Petroleum Measurement Standards (MPMS) Chapter 17.9 - Vessel Experience Factor (VEF) [EI HM 49], 3rd Edition, API, Washington, DC, US.
https://www.energyinst.org/industry/publications/topics/hydrocarbon-management/hm-49api-mpms-chapter-17.9-vessel-experience-factor-vef

[2] International Chamber of Shipping (ICS), Oil Companies International Marine Forum (OCIMF), International Association of Ports and Harbors (IAPH), 2020, International Safety Guide for Oil Tankers and Terminals (ISGOTT), 6th Edition, Witherby Publishing Group, Livingston, UK.
https://www.ics-shipping.org/publications/international-safety-guide-for-oil-tankers-and-terminals-isgott-sixth-edition

[3] American Petroleum Institute (API), Manual of Petroleum Measurement Standards (MPMS) Chapter 17.2, Measurement of Cargoes on Board Tank Vessels, API, Washington, DC, US.
https://standards.globalspec.com/std/1647252/api-mpms-17-2

[4] ASTM International / American Petroleum Institute (API), ASTM D1250 - API MPMS Chapter 11.1, Petroleum Measurement Tables, ASTM International, West Conshohocken, PA, US.
https://store.astm.org/d1250-08.html

[5] International Maritime Organization (IMO), International Convention for the Prevention of Pollution from Ships (MARPOL 73/78), Annex I, Oil Record Book, Part II.
https://www.imorules.com/MARPOL_ANNI.html

[6] Shewhart, W.A., 1931, *Economic Control of Quality of Manufactured Product*, D. Van Nostrand Company, New York, US.
https://archive.org/details/economiccontrolo0000shew

[7] Montgomery, D.C., 2020, *Introduction to Statistical Quality Control*, 8th Edition, John Wiley & Sons, Hoboken, NJ, US.
https://www.wiley.com/en-us/Introduction+to+Statistical+Quality+Control,+8th+Edition-p-9781119399308

[8] Senol, Y.E., 2024, *Assessment of human factor contribution to risk analysis of chemical cargo shortage incidents by using intuitionistic fuzzy integrated fault tree analysis*, Ocean Engineering, Vol.301, 117559, Elsevier.
https://doi.org/10.1016/j.oceaneng.2024.117559

[9] Meskuotiene, A., Kaskonas, P., Urbonavicius, B.G., Balciunas, G., Dobiliene, J., 2022, *Analysis of Liquid Quantity Measurement in Loading/Unloading Processes in Cylindrical Tanks*, Computation, Vol.10, no.7, 122, MDPI.
https://doi.org/10.3390/computation10070122

[10] Demirci, S.M.E., Cicek, K., 2022, *Deficiency Analysis Identified in PSC Inspections Using Event Tree Analysis*, Journal of Marine Technology and

Journal of Marine
Technology and Environment

DOI:10.53464/JMTE.02.2026.06

ISSN (Print): 1844-6116
ISSN (Online): 2501-8795
https://www. jmte.eu

Environment, Vol.1, pp.40-46, Constanta Maritime University.
https://doi.org/10.53464/JMTE.01.2022.05

[11] Ene, I., Dinu, D., 2024, *Short Introduction on Present Design and Trends Regarding Energy Efficiency Improvement on Large Crude Oil Tankers*, Journal of Marine Technology and Environment, Vol.2, pp.22-29, Constanta Maritime University.
https://doi.org/10.53464/JMTE.02.2024.03

Journal of Marine Technology and Environment
DOI:10.53464/JMTE.02.2026.07
ISSN (Print): 1844-6116
ISSN (Online): 2501-8795
https://www. jmte.eu

ELECTROCHEMICAL RECHARGEABLE BATTERY TECHNOLOGIES: A COMPARATIVE STATE-OF-THE-ART REVIEW

Ciprian POPA[1] & Andrei-Darius DELIU[2*]

[1]Romanian Naval Academy "Mircea cel Bătrân", Faculty of Marine Engineering, 1 Fulgerului Street, 900218, Constanța, Romania, ORCID ID 0009-0001-8630-7729, e-mail address: ciprian.popa@anmb.ro
[2*]National University of Science and Technology Politehnica Bucharest, Faculty of Electrical Engineering, 313 Splaiul Independentei Street, 060042, Bucharest, Romania, corresponding e-mail address: andrei_darius.deliu@stud.electro.upb.ro

Abstract: Electrical energy storage plays a critical role in modern industrial, transport, and power-system applications, particularly in the context of renewable-energy integration and grid-support services. Among available storage technologies, electrochemical batteries are especially important because they enable reversible conversion between electrical and chemical energy and provide a practical solution for a wide range of operating requirements. This paper presents a comparative technical analysis of the main rechargeable battery technologies, with emphasis on their electrochemical structure, operating principles, and application-related performance. The study examines the fundamental characteristics of electrochemical cells and battery packs, including nominal voltage, capacity, energy rating, and series-parallel configuration. It then reviews the main rechargeable chemistries currently used in practice, namely lead-acid, nickel-cadmium, nickel-metal hydride, lithium-ion, lithium-polymer, and sodium-based batteries. The analysis highlights the principal advantages and limitations of each technology in terms of energy density, cycle life, charging behaviour, safety constraints, environmental impact, and engineering applicability. The results indicate that no single battery chemistry is universally optimal, and that technology selection must be based on application-specific trade-offs involving cost, performance, durability, safety, and system-integration requirements.

Key words: Electrochemical energy storage, energy density, lead-acid batteries, lithium-ion batteries, nickel-based batteries, rechargeable batteries.

1. INTRODUCTION

Electrical energy is highly practical for generation, transmission, and end-use, yet it remains inherently difficult to stockpile at grid scale. In practice, the overwhelming share of electricity produced by utility plants is delivered and consumed almost instantaneously. Even so, a range of technologies can store energy at smaller scales by converting it into other domains-most commonly electrical, mechanical, chemical, or magnetic forms. These options are often compared using metrics such as energy density and typical discharge duration [1], [2], [3], [4], [5].

Among storage solutions, electrochemical batteries are widely employed in both consumer devices and industrial installations because they enable reversible conversion between electrical and chemical energy. The conversion efficiency for each direction (electrical → chemical or chemical → electrical) is typically on the order of ~ 85%, although this value depends on the specific chemistry and operating conditions. Electrochemical batteries are generally classified into two main categories [1], [5], [6], [7], [8], [9]:

1. Primary batteries (non-rechargeable). In these devices, electricity is produced through an electrochemical reaction that proceeds essentially in one direction. Once the active materials are depleted and the cell reaches end-of-discharge, the battery is not restored and is normally discarded. Primary cells are attractive where high energy density, both gravimetric (Wh/kg) and volumetric (Wh/L), is required for single-use applications.
2. Secondary batteries (rechargeable). Secondary cells operate via reactions that are largely reversible. After a battery has been discharged, it can be charged again by applying direct current from an external power source, which reverses the electrochemical reaction and stores energy in chemical form. When the battery is used again, this process goes in the opposite direction, converting the stored chemical energy back into electrical energy. Since some of the energy is lost as heat during both charging and

Journal of Marine Technology and Environment
DOI:10.53464/JMTE.02.2026.07
ISSN (Print): 1844-6116
ISSN (Online): 2501-8795
https://www. jmte.eu

discharging, the overall round-trip efficiency depends on the efficiency of each step. In practice, with each process typically operating at around 85% efficiency, the total round-trip efficiency is usually in the range of 70–75%, depending on the battery chemistry involved [5].

At the transmission and distribution level, utility-scale batteries support a broader set of grid services, including buffering variable output from wind and photovoltaic plants, enabling smart-grid functionalities and resilient communications/cyber-secure operation, strengthening system adequacy and dynamic stability to mitigate voltage instability and large-scale outages, enhancing power quality for both utility networks and downstream consumers, and contributing to decarbonization-oriented programs by lowering emissions, improving overall energy efficiency, and delivering co-benefits for environmental performance [1], [2], [3], [5].

Table 1. Overview of selected electrical, mechanical and magnetic energy-storage options [5]

Storage option	Dominant stored-energy domain	Typical discharge / storage timescale in applications	Qualitative specific energy kWh·kg^{-1}
Electrostatic capacitor	Electric field	sub-second (millise-conds to seconds)	low
Inductive storage (coil)	Magnetic field	sub-second (millise-conds to seconds)	medium
Electrochemi-cal battery	Chemical (electro-chemical)	long-duration (days to months)	medium
Flywheel system	Mechani-cal (rotational kinetic)	long-duration (days to months)	high
SMES (superconduct-ting magnetic energy storage)	Magnetic field	long-duration (days to months)	very high

A representative electrochemical cell, whether primary or rechargeable, consists of a positive and a negative electrode, electrically isolated by a separator, and an electrolyte that provides ionic conduction between the electrodes. The electrode assemblies are interfaced with external terminals integrated into the cell casing. Depending on the chemistry, a single cell typically operates at a low nominal potential, commonly in the range of ~1.2 to 3.6 V [5], [10], [11], [12].

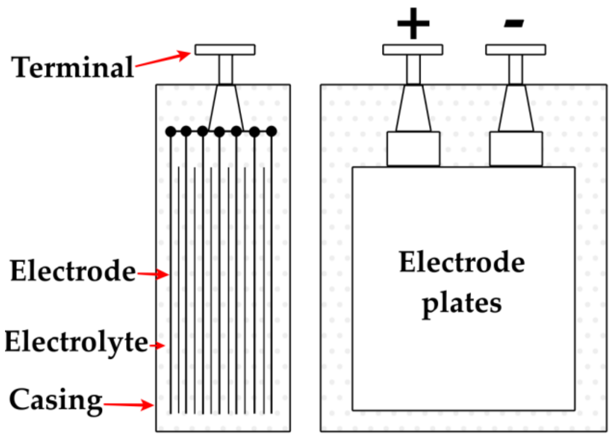

Figure 1 Architecture of the electrochemical cell

The charge storage capability of a cell is expressed as its capacity, *C*, usually reported in ampere-hours (Ah). Since 1A = Cs^{-1}, it follows that 1Ah = 3600C of transferable charge. Accordingly, a cell with capacity *C* can ideally supply *C* amperes for 1 hour, or equivalently C/n amperes for n hours, under a constant-current discharge assumption. In first approximation, Ah capacity scales with the effective electrode area (and associated active material utilization), whereas the cell voltage is primarily chemistry-determined and is not governed by electrode area [5].

A battery pack is formed by interconnecting multiple cells in series and/or parallel to meet required voltage and current levels. Increasing the pack voltage is achieved by adding cells in series, while increasing deliverable current (and capacity) requires additional cells in parallel. Practical battery ratings are commonly specified using the average discharge voltage and the Ah capacity available until the terminal voltage reaches a defined cutoff. The corresponding energy capability is typically expressed in watt-hours (Wh), obtained as the product of the representative voltage and the Ah rating, representing the energy that can be delivered to a load from a fully charged state under the specified conditions [5], [9], [13], [14], [15].

2. MAIN TYPES OF RECHARGEABLE BATTERIES

Journal of Marine Technology and Environment
DOI:10.53464/JMTE.02.2026.07
ISSN (Print): 1844-6116
ISSN (Online): 2501-8795
https://www.jmte.eu

Rechargeable battery technologies currently represent a well-established component of both industrial infrastructure and consumer electronics. In parallel, advanced electrochemical storage systems are being continuously improved to satisfy the requirements of a broad spectrum of applications, such as electric mobility, spacecraft systems, utility-scale load balancing, and renewable energy conversion systems, particularly those based on wind and solar resources, which are characterized by fluctuating power generation. The most widely recognized rechargeable battery chemistries are as follows [5], [9], [16], [17], [18]:

- Lead-acid (Pb-acid)
- Nickel-cadmium (NiCd)
- Nickel-metal hydride (NiMH)
- Lithium-ion (Li-ion)
- Lithium-polymer (Li-poly)
- Sodium battery

Table 2. Representative discharge cell voltages of common rechargeable battery chemistries [5]

Battery chemistry	Representative applications	Nominal discharge voltage (V)	Key observations
Lead-acid	Commonly employed in industrial systems, road vehicles, and marine applications	2.0	Conside-red one of the most economi-cal battery technolo-gies
Nickel-cadmium (NiCd)	Frequently used in portable power equipment	1.2	May be affected by the memory effect during repeated cycling
Nickel-metal hydride (NiMH)	Widely applied in automotive systems	1.2	Perfor-mance can be influenced by temperatu-re variations
Lithium-ion (Li-ion)	Typically used in laptops, mobile phones, and aerospace equipment	3.6	Regarded as safe under normal operation and does not contain metallic lithium
Lithium-polymer (Li-polymer)	Common in computers, mobile devices, and spacecraft-related applications	3.0	Includes metallic lithium in its construc-tion

The average discharge voltage varies according to the type of electrochemical system, as indicated in Table 2. In addition, Figure 2 presents a comparison of the energy densities of different battery technologies in terms of both specific energy (Wh/kg) and volumetric energy density (Wh/L). The selection of a suitable battery chemistry for a particular application depends on the optimization of performance, physical dimensions, and cost. The principal structural and functional characteristics of these electrochemical systems are examined in the subsequent discussion [5].

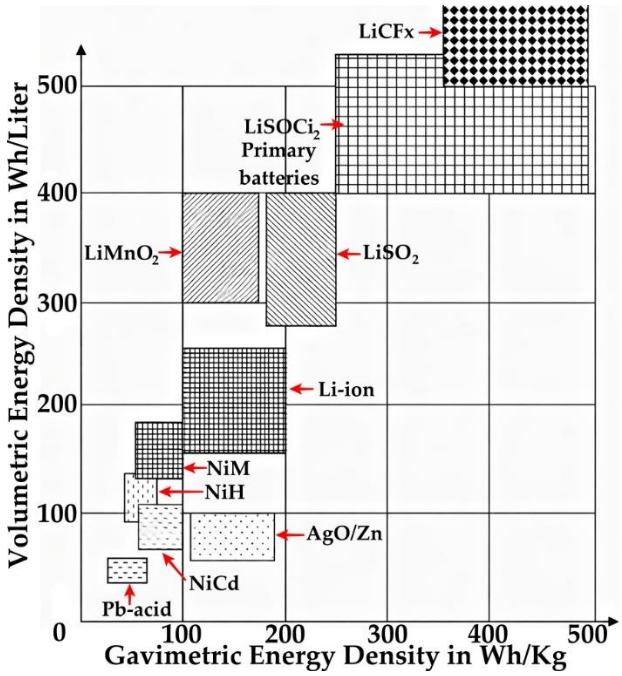

Figure 2 A comparative study on the energy density of different cell technologies [5]

2.1 Lead-acid

Rechargeable lead-acid batteries remain among the most extensively used electrochemical storage systems due to their technological maturity and favorable cost-to-

Journal of Marine Technology and Environment
DOI:10.53464/JMTE.02.2026.07
ISSN (Print): 1844-6116
ISSN (Online): 2501-8795
https://www. jmte.eu

performance ratio [19], despite their relatively low gravimetric and volumetric energy density. During discharge, the electrochemical reactions lead to the formation of water and lead sulfate, which results in dilution of the sulfuric acid electrolyte and a corresponding decrease in electrolyte specific gravity as the state of charge declines. When the battery is recharged, these reactions proceed in the opposite direction, regenerating metallic lead at the negative electrode and lead dioxide at the positive electrode, thereby restoring the cell to its charged condition [5], [20], [21].

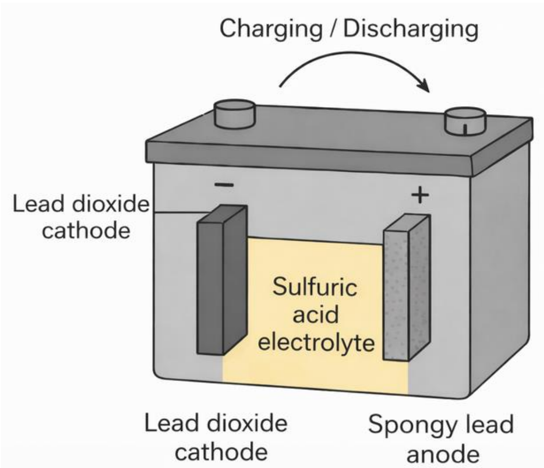

Figure 3 Lead-acid batteries [9]

Lead-acid batteries are manufactured in several configurations designed for different operating requirements. Shallow-cycle types are primarily intended for applications such as automotive and marine engine starting, where the battery must deliver a high current pulse over a short period. By contrast, deep-cycle designs are better suited to repeated charge-discharge operation and are therefore preferred in most energy storage installations. Another important variant is the sealed gel-cell battery, in which additives convert the electrolyte into a gelled, non-spillable medium. Owing to this construction, such batteries can be installed in inclined or inverted positions. However, their comparatively higher cost has restricted their broader use in specialized fields such as military avionics [5], [9], [20], [21], [22].

Table 3. Technical benefits and limitations associated with lead-acid battery technology [23]

Technical advantages
• Economical production due to mature and comparatively simple manufacturing processes • Reduced cost per unit of stored energy • High specific power and strong capability for delivering elevated discharge currents • Stable operation across a broad temperature range, including both low- and high-temperature conditions • In many conventional configurations, complex cell-level or block-level battery management systems are not essential
Technical limitations
• Low specific energy, resulting in limited gravimetric energy performance • Long recharge duration; full charging typically requires extended time intervals • Requirement for storage in a charged state in order to minimize sulfation effects • Restricted cycle life, particularly under repeated deep-discharge operation • Periodic water replenishment is necessary in flooded lead-acid designs • Transport and handling constraints are more significant for flooded battery configurations • Environmental concerns related to lead content and disposal requirements

2.2 *Nickel-cadmium (NiCd)*

Nickel-cadmium (NiCd) batteries represent a well-established rechargeable battery technology. In this system, nickel hydroxide functions as the positive active material, while cadmium serves as the negative electrode material. The electrodes are typically isolated by polymer-based separators and immersed in an alkaline electrolyte, commonly potassium hydroxide, within a metallic enclosure. Owing to their sealed construction and lower mass relative to conventional lead-acid systems, NiCd batteries were historically adopted in a wide range of portable rechargeable consumer devices [5], [9].

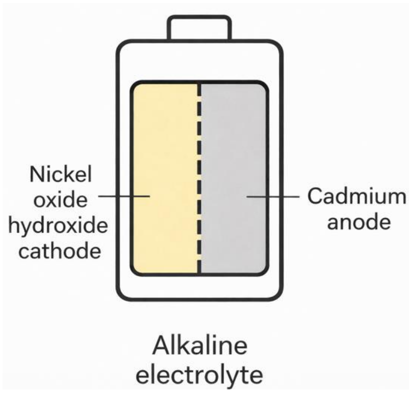

Figure 4 Nickel-cadmium (NiCd) batteries [9]

Compared with lead-acid batteries, NiCd systems generally provide superior tolerance to temperature variation and a longer service life under deep cycling conditions. Nevertheless, their application has declined because of two major limitations. First, they are susceptible to the memory effect, which can reduce the available capacity under certain operating conditions.

Journal of Marine Technology and Environment
DOI:10.53464/JMTE.02.2026.07
ISSN (Print): 1844-6116
ISSN (Online): 2501-8795
https://www.jmte.eu

Second, the toxic nature of cadmium has led to increasing environmental and regulatory concerns. As a result, NiCd technology has gradually been displaced in laptop computers and other high-value portable electronic products by nickel-metal hydride and lithium-ion batteries [5].

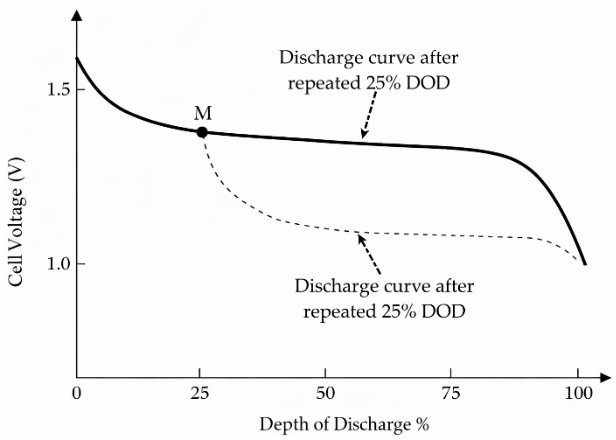

Figure 5 The Memory Effect in Nickel-Cadmium (NiCd) battery [5]

NiCd batteries are known to exhibit a so-called memory effect, meaning that their electrochemical behavior may adapt to a repeatedly imposed charge-discharge regime. When the battery is cycled many times over only a limited portion of its total capacity, for example up to approximately 25% of full discharge, it tends to retain that operating range as a reference condition. If the cell is later discharged beyond this previously repeated limit, the terminal voltage may decline sharply below its normal profile, creating the impression that the battery has lost part of its usable capacity [5].

This behavior can be interpreted as a temporary reduction in accessible energy caused by long-term shallow cycling. Recovery of the original capacity can often be achieved through a reconditioning procedure, sometimes referred to as battery exercising. In practice, this involves occasionally discharging the cell to a very low voltage level and then recharging it completely to its nominal full-charge voltage. The memory effect is generally considered characteristic of NiCd batteries, whereas most other rechargeable battery chemistries do not display this phenomenon to the same extent [5].

Table 4. Principal technical merits and limitations of nickel-cadmium battery technology [23]

Technical merits
• High structural and electrochemical robustness, with the ability to sustain a large number of charge-discharge cycles when maintained appropriately • Capability to accept very high charging rates with comparatively low degradation stress • Strong tolerance to demanding load conditions and relatively stable behavior under misuse or non-ideal operation • Long storage life; cells may remain in a discharged state and be restored to operation after suitable conditioning • Straightforward storage and transport requirements in comparison with some other battery systems • Reliable low-temperature performance, making the technology suitable for cold-environment operation • Favorable economic performance in terms of cost per cycle over the service lifetime • Availability in a broad spectrum of cell formats, capacities, and performance categories
Technical limitations
• Lower specific energy than more recent rechargeable battery technologies, which reduces suitability for weight- and volume-constrained systems • Pronounced memory effect, which may require periodic deep discharge or reconditioning to recover usable capacity • Use of cadmium, a hazardous toxic metal, creates significant environmental and disposal constraints • Elevated self-discharge rate, leading to noticeable energy loss during storage and the need for recharging before use • Low nominal cell voltage, approximately 1.20 V, necessitates the connection of numerous cells in series to obtain higher pack voltages

2.3 Nickel-Metal Hydride Batteries

Nickel-metal hydride (NiMH) batteries were developed as an advanced alternative to nickel-cadmium (NiCd) systems, with the primary objective of improving energy storage capability while reducing the environmental drawbacks associated with cadmium-based electrodes. From an electrochemical standpoint, NiMH technology preserves several operating principles of NiCd batteries, but replaces the cadmium-containing negative electrode with a hydrogen-absorbing metal alloy. This design modification not only mitigates toxicity-related concerns, but also contributes to a higher specific energy and a less pronounced memory effect during repeated cycling [5], [9].

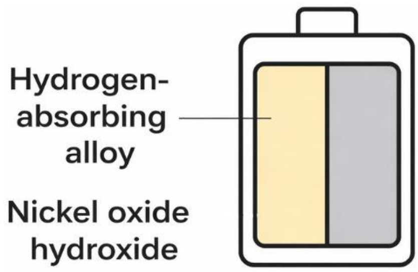

Figure 6 Nickel-metal hydride (NiMH) batteries [9]

Journal of Marine Technology and Environment
DOI:10.53464/JMTE.02.2026.07
ISSN (Print): 1844-6116
ISSN (Online): 2501-8795
https://www. jmte.eu

One of the principal advantages of NiMH batteries is their improved energy density compared with NiCd cells, which makes them more suitable for applications where mass and volume are important design constraints. In addition, the reduced memory effect enhances their practical usability under partial charge-discharge operation. For these reasons, NiMH batteries were widely adopted in portable electronics, hybrid vehicles, and various industrial devices, particularly during the period preceding the large-scale dominance of lithium-ion technology [5].

Despite these advantages, NiMH systems also exhibit several technical limitations. Their peak power capability is generally lower than that of comparable NiCd batteries, which can restrict their use in applications requiring very high transient current delivery. Moreover, NiMH batteries typically present a relatively high self-discharge rate, leading to progressive capacity loss during storage when compared with more advanced lithium-based systems. Another important drawback is their sensitivity to overcharging, since excessive charging may accelerate degradation processes, increase internal temperature, and shorten service life if charge management is not properly controlled [5].

NiMH batteries have been used in automotive, industrial, and consumer electronics because they offer a practical balance between cost, safety, and performance. However, as lithium-ion technology has become more advanced, offering higher energy density, lower self-discharge, and better overall performance in demanding applications, NiMH batteries have gradually become less important in both the market and research. Even so, they still remain a suitable choice in certain applications where reliability, reasonable cost, and well-established manufacturing processes are valued more than achieving the highest possible energy density [5].

Table 5. Main engineering advantages and limitations of nickel-metal hydride battery technology [23]

Technical advantages
• Higher energy density than several conventional rechargeable chemistries, enabling either extended operating duration or reduced battery-pack volume for a given energy requirement • Elimination of cadmium-related manufacturing, handling, and end-of-life constraints, thereby improving environmental acceptability and regulatory compliance • Easier substitution in systems originally designed for nickel-cadmium cells because of the substantial design and functional similarities between the two technologies • Favorable operational capability in low-temperature environments, including applications around subzero conditions
Technical limitations
• Restricted cycle durability under repeated deep-discharge operation, particularly at elevated current demand; performance degradation becomes more pronounced under severe cycling conditions • Sensitivity to high-rate discharge; although capable of supplying substantial current, frequent operation under heavy load accelerates aging and shortens service life • Greater charging complexity, as NiMH cells generate more heat during charging and generally require more controlled charging protocols than NiCd systems • Increased self-discharge during storage relative to NiCd batteries, resulting in more rapid capacity loss when the battery is not in use • Trickle-charge management is more critical, since improper charge maintenance can promote thermal stress and long-term degradation • Chemical modifications introduced to reduce self-discharge may improve storage retention, but can also be associated with compromises in energy density

The electrochemistry of the nickel–metal hydride (NiMH) battery is based on [9]:

- Positive electrode: The cathodic active material is commonly nickel oxyhydroxide (NiOOH).
- Negative electrode: The anodic side is generally based on a metal alloy capable of reversibly absorbing hydrogen, usually denoted MH.
- Electrolyte: Ionic transport takes place through an aqueous potassium hydroxide (KOH) solution.

2.4 Lithium-Ion battery technology

Lithium-ion technology constitutes a relatively recent but highly influential development in the field of rechargeable batteries. Its widespread adoption is mainly due to its high specific and volumetric energy density, which markedly exceeds that of lead-acid systems. This performance benefit arises in large part from the low atomic mass of lithium and from the comparatively high nominal voltage of Li-ion cells. Because each cell provides a higher voltage than lead-acid, NiCd, or NiMH cells, fewer units are required in series to reach a prescribed battery voltage, thereby reducing pack complexity and potentially lowering assembly-related costs [5], [9], [24].

Despite these advantages, Li-ion batteries are associated with important electrochemical and safety constraints. Interfacial reactions between the electrode surfaces and the electrolyte lead to the formation of passivation layers that influence long-term cycling behavior. In addition, these batteries are particularly vulnerable to overcharge, overheating, and other battery-management deficiencies. Consequently, Li-ion systems

Journal of Marine Technology and Environment
DOI:10.53464/JMTE.02.2026.07
ISSN (Print): 1844-6116
ISSN (Online): 2501-8795
https://www. jmte.eu

require sophisticated charging strategies and integrated protection electronics to ensure safe and reliable operation [5], [24], [25].

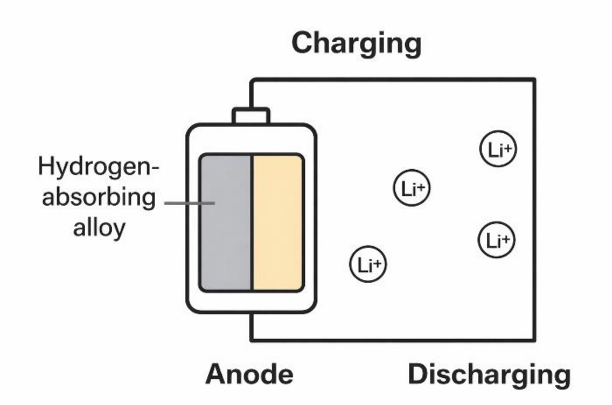

Figure 7 Lithium-Ion batteries [9]

In electric-vehicle applications, Li-ion batteries must simultaneously satisfy high power demand, sufficient energy storage capacity, long cycle life, and acceptable cost. Their high energy and power density make them attractive for such uses, but also intensify thermal management requirements because substantial heat may be generated within a compact volume. Although early large-scale Li-ion battery systems were characterized by high cost, ongoing technological progress has been directed toward improving durability, safety, and affordability [5], [24], [25].

Table 6. Principal engineering advantages and limitations of lithium-ion battery technology [23]

Technical advantages
• High specific energy combined with strong power-delivery capability, particularly in power-oriented cell configurations • Extended cycle life and favorable calendar life under properly controlled operating conditions, with minimal routine maintenance requirements • High usable capacity, low internal impedance, and efficient charge transfer reflected in favorable Coulombic efficiency • Relatively straightforward charging strategy compared with some alternative advanced chemistries, together with comparatively short charge duration
Technical limitations
• Requirement for dedicated protection electronics to prevent hazardous operating conditions, including thermal runaway under electrical or thermal abuse • Accelerated degradation at elevated temperature and under prolonged storage at high state of charge or high terminal voltage • Rapid charging is severely constrained or impractical at subzero temperatures due to increased risk of lithium plating and performance deterioration • Large-scale transport and distribution are subject to strict safety and regulatory requirements, particularly for high-energy shipments

The selection of the cathode material plays a decisive role in determining battery performance, giving rise to multiple Li-ion chemistries, each tailored to particular application requirements [9], [22]:

- Anode: In most lithium-ion cells, the negative electrode is commonly based on graphite, often represented as LiC_6.
- Cathode: The positive electrode is generally composed of a lithium-containing metal oxide, such as $LiCoO_2$, $LiFePO_4$, or NMC-type materials.
- Electrolyte: Ionic conduction is ensured by a lithium salt, for example $LiPF_6$, dissolved in an organic solvent medium.
- Separator: The two electrodes are kept apart by a microporous polymer separator that prevents electrical contact while allowing ion transport.
- Lithium ions: During discharge, Li^+ ions migrate from the anode toward the cathode.

2.5 Lithium-Polymer batteries

Lithium-polymer (Li-polymer) batteries constitute a variant of lithium-based electrochemical storage systems in which the electrolyte is incorporated into a polymer matrix rather than being present exclusively as a conventional free-flowing liquid. In this configuration, the polymer medium performs a dual function by enabling ionic transport while also acting as a separator between the electrodes. This structural approach permits the development of compact and lightweight cells with improved packaging flexibility, which is one of the principal reasons for the growing interest in this technology [5].

From a construction standpoint, lithium-polymer cells are generally based on layered architectures in which lithium-containing active materials are combined with thin polymer electrolyte films. The use of a solid or gel-like polymer electrolyte can contribute to an increase in specific energy because the electrolyte and separator functions are integrated into a single component, thereby reducing inactive material within the cell. In addition, the replacement of a fully liquid electrolyte with a polymer-based medium may reduce leakage risk and improve mechanical adaptability, especially in applications where thin, lightweight, or custom-shaped battery formats are required [5], [26].

Another important advantage of lithium-polymer technology is related to interfacial stability. Compared with traditional liquid-electrolyte systems, the interaction between lithium and a polymer-based electrolyte may be less aggressive under controlled operating conditions, which can be beneficial for reducing certain parasitic reactions and improving safety characteristics. However,

Journal of Marine Technology and Environment
DOI:10.53464/JMTE.02.2026.07
ISSN (Print): 1844-6116
ISSN (Online): 2501-8795
https://www.jmte.eu

the practical performance of these batteries strongly depends on electrolyte formulation, ionic conductivity, temperature, and cell design. As with other lithium-based systems, careful control of charging conditions and thermal behavior remains essential to ensure reliability and long-term durability [5], [27].

Lithium-polymer batteries have attracted considerable attention in transportation and portable electronics because of their high energy density and design versatility. In electric-vehicle applications, their low mass and potential for efficient space utilization make them particularly attractive for extending driving range compared with heavier conventional battery technologies. The ability to manufacture cells in thin and flexible geometries also supports their use in compact electronic devices, aerospace subsystems, and other applications where strict mass and volume constraints apply [5].

Despite these advantages, lithium-polymer technology also presents several engineering challenges. The ionic conductivity of solid or polymer-rich electrolytes may be lower than that of liquid electrolytes, particularly at reduced temperatures, which can limit rate capability and overall power performance. In addition, production cost, material stability, and long-term cycling behavior remain critical considerations for large-scale deployment. For these reasons, current research continues to focus on improving polymer electrolyte conductivity, interfacial compatibility, thermal stability, and manufacturing scalability [5].

Overall, lithium-polymer batteries are regarded as a promising direction in advanced electrochemical energy storage, particularly where a combination of high specific energy, reduced weight, and geometric flexibility is required. Their future development is closely linked to progress in solid-state and hybrid polymer-electrolyte systems, which may further enhance both safety and performance in next-generation battery applications [5].

2.6 Sodium battery technology

Sodium-based batteries are among the most recent electrochemical storage technologies to enter advanced energy markets. They have been developed primarily for applications in which high power capability, operational durability, and suitability for large-scale energy storage are required. In particular, sodium-metal halide systems have demonstrated relevance for hybrid rail transport, heavy-duty vehicles, and stationary backup storage associated with renewable energy installations [5].

This electrochemical technology is especially appropriate for operating regimes that combine short bursts of high power with the need for sustained energy delivery over longer periods. Such characteristics are advantageous in transportation systems requiring strong starting or traction support, as well as in wind and solar power installations where storage is needed to improve continuity and operational stability. Although sodium-based batteries may involve higher system complexity in certain designs, they remain a promising option for high-capacity applications due to the abundance of sodium resources and their potential cost advantages [5].

4. CONCLUSIONS

This study shows that electrochemical batteries continue to be among the most important energy-storage solutions for modern industrial, transport, and power-system applications, mainly because they can efficiently convert electrical energy into chemical energy and back again. The analysis also confirms that battery performance depends on several key factors, including cell chemistry, nominal voltage, capacity, energy density, cycle life, and operating safety constraints. In addition, the design of the battery pack plays a major role in determining the final voltage, current, and energy capability of the system.

The comparison highlights that lead-acid batteries are still a practical option for low-cost and high-power applications, even though they have relatively low energy density and limited durability under deep cycling. NiCd batteries offer strong robustness and fast-charging capability, but their use is limited by the memory effect and the environmental concerns associated with cadmium. NiMH batteries provide a better balance between energy density and environmental acceptability, although they are affected by self-discharge and charging-related thermal issues. Among all the technologies reviewed, lithium-ion batteries currently offer the best overall combination of energy density, voltage level, and flexibility of use, although they require advanced protection and thermal-management systems. Lithium-polymer and sodium-based batteries also appear to be promising solutions, especially for lightweight designs and large-scale energy-storage applications.

Overall, the study makes it clear that no rechargeable battery technology is ideal for every application. Each chemistry has its own strengths, limitations, and areas of suitability. For this reason, the choice of a battery system must always be based on the specific requirements of the intended application, whether the priority is low cost, high energy density, high power capability, long service life, environmental compatibility, or grid support. Future progress in electrochemical energy storage will depend on continued advances in active materials, electrolyte systems, thermal management, battery-pack engineering, and intelligent control methods, with strong emphasis on safety, sustainability, and long-term performance.

5. FUNDING

Journal of Marine Technology and Environment
DOI:10.53464/JMTE.02.2026.07
ISSN (Print): 1844-6116
ISSN (Online): 2501-8795
https://www. jmte.eu

The authors received no financial support for the research, authorship, and/or publication of this work.

6. CREDIT AUTHORS STATEMENT

Conceptualization: D.A.-D.; Investigation: P.C.; Methodology: D.A.-D.; Resources: P.C.; Visualization: D.A.-D.;

Writing – original draft: P.C.; Writing – review & editing: D.A.-D.

7. REFERENCES

[1] M. Muzammal Islam *et al.*, "Improving Reliability and Stability of the Power Systems: A Comprehensive Review on the Role of Energy Storage Systems to Enhance Flexibility," *IEEE Access*, vol. 12, pp. 152738–152765, 2024, doi: 10.1109/ACCESS.2024.3476959.

[2] A. F. Schiochet, G. J. Friedrich, J. A. P. Filho, and J. G. De Oliveira, "Dynamic State-of-Charge Modeling in Battery Energy Storage Systems with Power Ramp-Rate Control," *IEEE Access*, 2026, doi: 10.1109/ACCESS.2026.3666451.

[3] A. E. Leon, A. R. Del Nozal, and J. M. Mauricio, "Frequency Support Strategy for Fast Response Energy Storage Systems," *IEEE Trans. Power Syst.*, vol. 39, no. 3, pp. 5439–5442, May 2024, doi: 10.1109/TPWRS.2024.3358631.

[4] K. D. Pippi, G. C. Kryonidis, A. I. Nousdilis, and T. A. Papadopoulos, "Assessing the Provision of Ancillary Services by PV-BES Systems Considering BES Capacity Degradation," *IEEE Trans. Ind. Appl.*, vol. 60, no. 3, pp. 4821–4831, May 2024, doi: 10.1109/TIA.2024.3371391.

[5] Mukund R. Patel, "Shipboard Electrical Power Systems", Second Edition, Taylor & Francis Group, 2022.

[6] M. Elmahallawy, T. Elfouly, A. Alouani, and A. M. Massoud, "A Comprehensive Review of Lithium-Ion Batteries Modeling, and State of Health and Remaining Useful Lifetime Prediction," *IEEE Access*, vol. 10, pp. 119040–119070, 2022, doi: 10.1109/ACCESS.2022.3221137.

[7] N. Morawan, I. Mungkhala, C. Attaphong, J. Katers, and P. Sarikprueck, "Environmental Impact Assessment of Lead-Acid and Lithium-ion Battery Waste Management in Thailand," *2024 IEEE IAS Ind. Commer. Power Syst. Asia, I CPS Asia 2024*, pp. 729–734, 2024, doi: 10.1109/ICPSASIA61913.2024.10761693.

[8] C. Ji, J. Dai, C. Zhai, J. Wang, Y. Tian, and W. Sun, "A Review on Lithium-Ion Battery Modeling from Mechanism-Based and Data-Driven Perspectives," *Process. 2024, Vol. 12*, vol. 12, no. 9, Sep. 2024, doi: 10.3390/PR12091871.

[9] I. Redhwi, S. Almalki, H. Radhwi, A. Jarwali, A. Abaaltahin, and A. Fallatah, "Advancements in battery technology: A comprehensive review," *Clean Energy Sci. Technol.*, vol. 4, no. 1, 2026, doi: 10.18686/CEST573.

[10] J. B. Goodenough and K. S. Park, "The Li-ion rechargeable battery: A perspective," *J. Am. Chem. Soc.*, vol. 135, no. 4, pp. 1167–1176, Jan. 2013, doi: 10.1021/JA3091438.

[11] D. Noel Buckley, C. O'Dwyer, N. Quill, and R. P. Lynch, "Electrochemical Energy Storage," *Issues Environ. Sci. Technol.*, vol. 2019-January, no. 46, pp. 115–149, Oct. 2018, doi: 10.1039/9781788015530-00115.

[12] K. Arslan, K. B. Dermenci, J. Van Mierlo, and M. Berecibar, "Current and future trends in lithium-ion battery electrode production machinery: A comprehensive review," *Appl. Energy*, vol. 402, p. 126968, Jan. 2026, doi: 10.1016/J.APENERGY.2025.126968.

[13] J. T. Warner, "Battery Structure, Mechanical Packaging, and Material Selection," *Handb. Lithium-Ion Batter. Pack Des.*, pp. 213–233, 2024, doi: 10.1016/B978-0-443-13807-2.00009-2.

[14] L. He, L. Kong, Y. Gu, C. Liu, T. He, and K. G. Shin, "Extending battery system operation via adaptive reconfiguration," *ACM Trans. Sens. Networks*, vol. 15, no. 1, Jan. 2019, doi: 10.1145/3284556.

[15] M. Ceylan and A. Balikci, "An Intermodular Active Balancing Topology for Efficient Operation of High Voltage Battery Packs in Li-Ion Based Energy Storage Systems: Switched (Flying) DC/DC Converter," *Energies 2023, Vol. 16*, vol. 16, no. 15, Jul. 2023, doi: 10.3390/EN16155608.

[16] P. Herodotou, R. Hao, G. E. Georghiou, and S. Yagi, "Rechargeable magnesium batteries: System-level opportunities and challenges for battery energy storage applications," *Electrochim. Acta*, vol. 555, p. 148315, Apr. 2026, doi: 10.1016/J.ELECTACTA.2026.148315.

[17] G. G. Njema, R. Ben, O. Ouma, and J. K. Kibet, "A Review on the Recent Advances in Battery Development and Energy Storage Technologies," *J. Renew. Energy*, vol. 2024, no. 1, p. 2329261, Jan. 2024, doi: 10.1155/2024/2329261.

[18] A. Nekahi, A. K. Madikere Raghunatha Reddy, X. Li, S. Deng, and K. Zaghib, "Rechargeable Batteries for the Electrification of Society: Past, Present, and Future," *Electrochem. Energy Rev.*, vol. 8, no. 1, Dec. 2025, doi: 10.1007/S41918-024-00235-8.

[19] M. O'Brien, M. E. Borcherdt, S. Harris, and H. Shadravan, "REPLACING LEAD-ACID AND NICKEL-CADMIUM STATIONARY BATTERIES WITH LITHIUM-ION – IT'S NOT A SIMPLE SWAP," *Rec. Conf. Pap. - Annu. Pet. Chem. Ind. Conf.*, 2024, doi: 10.1109/PCIC47799.2024.10832197.

[20] B. V. Rajanna and M. K. Kumar, "Dynamic model development for lead acid storage battery," *Indones. J. Electr. Eng. Comput. Sci.*, vol. 15, no. 2, pp. 609–619, Aug. 2019, doi: 10.11591/IJEECS.V15.I2.PP609-619.

[21] G. J. May, A. Davidson, and B. Monahov, "Lead batteries for utility energy storage: A review," *J. Energy Storage*, vol. 15, pp. 145–157, Feb. 2018, doi: 10.1016/J.EST.2017.11.008.

[22] M. C. Kocer *et al.*, "Assessment of Battery Storage Technologies for a Turkish Power Network," *Sustain. 2019, Vol. 11*, vol. 11, no. 13, Jul. 2019, doi: 10.3390/SU11133669.

[23] A. Development Bank, "HANDBOOK ON BATTERY ENERGY STORAGE SYSTEM," 2018, doi: 10.22617/TCS189791-2.

[24] P. Parvizi, M. Jalilian, A. M. Amidi, M. R. Zangeneh, and J. R. Riba, "From Present Innovations to Future Potential: The Promising Journey of Lithium-Ion Batteries," *Micromachines 2025, Vol. 16*, vol. 16, no. 2, Feb. 2025, doi: 10.3390/MI16020194.

[25] Y. Chen *et al.*, "A review of lithium-ion battery safety concerns: The issues, strategies, and testing standards," *J. Energy Chem.*, vol. 59, pp. 83–99, Aug. 2021, doi: 10.1016/J.JECHEM.2020.10.017.

[26] C. POPA, I. CHIABURU, and H. ISAC, "REVIEW OF BATTERY TYPES AND APPLICATION TO WIND POWER GENERATION SYSTEM.," *J. Mar. Technol. Environ.*, vol. 2, no. 2, pp. 72–79, Oct. 2023, doi: 10.53464/JMTE.02.2023.12.

[27] Florețiu Deliu, "FENOMENE TRANZITORII ÎN ECHIPAMENTELE ELECTRICE NAVALE ALIMENTATE HIBRID.", Editura Politehnica Timişoara, 2011.

Journal of Marine Technology and Environment
DOI:10.53464/JMTE.02.2026.08
ISSN (Print): 1844-6116
ISSN (Online): 2501-8795
https://www. jmte.eu

REDUCTIONS IN ENGINE EXHAUST EMISSIONS IN A HYBRID FLETTNER ROTOR POWER-ASSISTED VESSEL

Lubomir A. RIBAROV[1]

[1]United States Merchant Marine Academy, Department of Marine Engineering, 300 Steamboat Road, Kings Point, NY 11027, USA, e-mail ribarovl@usmma.edu

Abstract : With the increase of Greenhouse Gas (GHG) emissions, the maritime industry has seen an influx of low emission and environmental protection solutions to reduce the GHG-, Hydrocarbon (HC)-, Nitrogen oxides (NOx)-, Sulphur oxides (SOx)-, and particulate matter (PM) emissions. The Flettner rotor is a technology that utilizes wind and the Magnus effect to generate lift for propulsion assist of the vessel. This paper builds on recently reported findings demonstrating the viability of a Flettner rotor propulsion in a hybrid diesel-electric propulsion system for a small cargo ship. Prior related work provided CFD analyses to determine the optimal system architecture in terms of number of Flettner rotors, rotor sizing (diameter, length, etc.), rotation speed and direction, rotor(s) spacing, relative rotor(s) arrangement, etc. Optimal rotor rotational speed was determined to maximize the Lift-to-Drag (L/D) ratios for various geometric rotor configurations. Sample calculations for optimal operating conditions based on Flettner rotor geometry, rotational speed, wind speed, ship's velocity highlight the potential shipboard power contributions from the operation of Flettner rotor as a power-assist to total onboard propulsive ship power. Estimations of commensurate emissions reductions from engine exhaust (assuming a Diesel-powered main engine) support the estimated environmental benefits of the proposed hybrid Flettner rotor power-assisted propulsion architecture.

Key words : Exhaust Gas Emissions Reduction; Flettner Rotor; Hybrid Ship Propulsion; System Integration; Wind-Assisted Propulsion Systems (WAPS)

1. INTRODUCTION

This paper illustrates a reduction of pollution from emissions present in the exhaust of heat engine (mainly Diesel cycle)-powered merchant ships, specifically, during operations of such ships both near, and in port. Typically, these (Diesel cycle) heat engines, burning hydrocarbon (HC) fuels, are predominantly used for main propulsion. Most of the hydrocarbon pollution reduction initiatives are focused on the emissions from larger heat engines used for main ship propulsion.

About 90% of the world's global trade is carried by large sea going vessels. Of these, the following three types are the highest fuel consumers on per annual basis: container ships, bulk carriers, and oil tankers. Combined, these types of ships consume nearly 2/3 (> 66%) of the annual global shipping fuel (HFO-equivalent) based on recent data analyses from Janes Sea Module Global Shipping Database [1].

According to current estimates presented in the Third IMO GHG Study 2014 [2], international shipping emitted 796 million tons of CO_2 in 2012, which accounts for no more than about 2.2% of the total emission volume for that year. Furthermore, the mid-range forecasted scenarios discussed during the Third IMO GHG Study 2014 showed that by 2050, CO_2 emission from international shipping could grow by between 50% and 250% depending on the expected future economic growth, world maritime commerce, and energy developments.

The Fourth IMO GHG Study 2020 [3] provided a global perspective for ocean-going vessels fuel consumption. This was consistent with the earlier findings based on the 2018 data from Janes Sea Module Global Shipping Database [1].

GHG emissions, which trap heat in the Earth's atmosphere, resulting in global warming thus leading to climate changes, consist of the following gases [4]: 79.7% Carbon Dioxide (CO_2), 11.1% methane (CH_4), 6.1% Nitrous oxide (N_2O), and trace amounts (3.1%) of Fluorinated gases, such as hydrofluorocarbons (HFCs), perfluorocarbons (PFCs), Sulphur hexafluoride (SF_6), and Nitrogen trifluoride (NF_3).

The international requirements on ship engines' emissions of NOx, SOx, and PM are determined and regulated by the IMO's document *MARPOL Convention*

Journal of Marine Technology and Environment
DOI:10.53464/JMTE.02.2026.08
ISSN (Print): 1844-6116
ISSN (Online): 2501-8795
https://www.jmte.eu

Annex VI – Regulations for the Prevention of Air Pollution from Ships [5]. These stringent requirements for NOx and SOx apply even close to shores within the Emission Control Areas (ECAs) for ship operations near land.

Energy Efficiency Design Index (EEDI) concept is an amendment to the IMO's MARPOL Annex VI [5], ensuring the reduction of GHG emissions from shipping. The EEDI principle is to compare the GHG emissions of new ships with a baseline of existing ships built during the 2000 – 2010 period. A reduction factor in the EEDI is required for all new ship builds.

The present work focused on the feasibility of the Flettner rotor power assist in augmenting ship propulsion in a hybrid diesel-electric power concept. This, in turn, demonstrated reductions in HC fuel consumption and commensurate decrease in HC-based airborne pollutants towards green (and/or "more-green") energy technologies to be implemented in ship propulsion systems. This is consistent with the IMO's recently announced goals for reducing shipping emissions: 40% compared to 2008 levels by 2030, and 70% by 2050.

2. AIRFOIL THEORY – LIFT AND DRAG

The current paper builds upon the earlier findings from a related previous work [6]. Detailed 2-D CFD analyses were completed with EasyCFD [7], a simple CFD teaching tool with a RANS κ-ε turbulence model. EasyCFD's built-in gas library was used to determine the air properties (at ambient conditions), with moderate mesh sizing (approx. 25,000 cells) for relatively fast processing. Denser meshing (auto-generated) was used near rotor's surface for higher resolution. Readers are directed to our previous work [6] for related details.

A rotating rotor (such as the Flettner Rotor) is similar to an aerofoil in producing lift, *L*, and drag, *D* (Fig. 1) while monitoring the value of *L/D* [8]. The lift, drag, and pitching moments of aerofoils, described by their respective section coefficients, c_l, c_d, and c_m, are functions of the angle of attack (AOA), α, and the operational speed of the aerofoil (i.e., the Reynolds number, *Re*. For a given α and *Re*, a typical aerofoil reaches its maximum lift at the maximum α beyond which it is assumed to be stalled due to separation of flow (where lift is rapidly lost, while drag is increasing).

Fundamental aerofoil theory [9] indicates that different aerofoil shapes (cross-sectional profiles) offer different lift-to-drag (*L/D*) ratios.

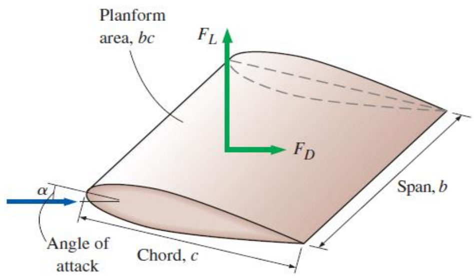

Figure 1. Typical aerofoil [8]

The Aspect Ratio, *AR* (i.e., span/chord) is an important wing performance characteristic relating lift and drag. Typically, higher *AR*s lead to higher *L/D* ratios but with more structural challenges (i.e., wing bending, wing tip deflection, wing root stresses, etc.). Lift and drag are defined in (1) and (2), respectively:

$$L = \frac{1}{2}\rho V^2 A C_L \tag{1}$$

$$D = \frac{1}{2}\rho V^2 A C_D \tag{2}$$

In our calculations we used well-established values for C_L = 12.5 and C_D = 0.2 from prior work [10]. The total lift coefficient, C_L, for a finite wing [11] is defined in (3).

$$C_L = \frac{(c_l)^2}{1+\frac{c_l}{\pi\,(AR)}} \tag{3}$$

Similarly, for modest values of α, the induced drag coefficient, $C_{D,i}$, and the total drag coefficient, C_D, are defined in (4) and (5), respectively.

$$C_{D,i} = \frac{(C_L)^2}{\pi\, e\, AR} \tag{4}$$

$$C_D = c_d + C_{D,i} \tag{5}$$

According to Prandtl Lifting Line Theory [9], an elliptical oval represents an ideal wing planform are (which minimizes induced drag through reduced wing downwash). In (4), *e* is the span efficiency factor, which is an index of how ideal a wing planform is, compared to the ideal elliptical oval shape.

A rotating rotor (such as the Flettner Rotor) is similar to an airfoil in producing lift, *L*, and drag, *D* while monitoring the value of *L/D*. A symmetric aerofoil, such as the NACA 0024 [12] produces no lift at α = 0 deg. (Fig. 2). The values of C_L/C_D for the NACA 0024 aerofoil (Fig. 2) are given as function of several different Re numbers (i.e., 100,000; 200,000; 500,000; 1,000,000). C_L/C_D ratio increases progressively with higher Re number. The corresponding maximum value for C_L/C_D = 68.8 at *Re* = 1,000,000 occurs at α = 9 deg.

Journal of Marine Technology and Environment
DOI:10.53464/JMTE.02.2026.08
ISSN (Print): 1844-6116
ISSN (Online): 2501-8795
https://www.jmte.eu

Values for C_L/C_D are lower for the lower *Re* values, respectively.

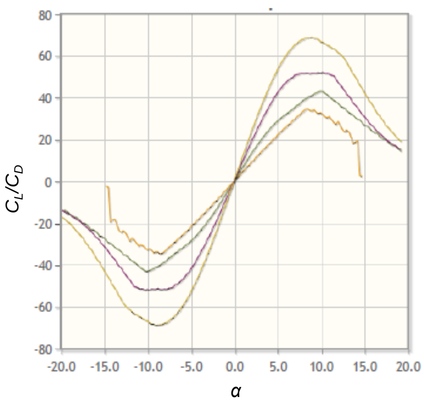

Figure 2. C_L/C_D vs. α for NACA 0024 airfoil [12]

In our calculations for the Flettner Rotor, we used $C_L/C_D = 12.5/0.2 = 62.5$, which is similar (within approx. 9%) to the maximum value of C_L/C_D (at α = 9 deg.) for the NACA 0024 symmetric aerofoil profile.

3. RELATIVE WIND CALCULATIONS

Due to the motion of a ship with velocity V_{ship}, relative to the true wind, V_{true}, the apparent wind speed, V_a, creates an angle β between the *L* and *D* force vectors for any true wind speed (and resulting apparent wind speed) direction (Fig. 3).

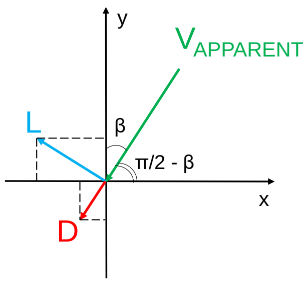

Figure 3. Basic Directions of Wind Relative to Ship

Considering the component of *L* (10) in the y-direction (Fig. 4) and the component of D (11) in the y-direction (Fig. 5):

$$L_y = L\cos\left(\frac{\pi}{2} - \beta\right) \#(10)$$

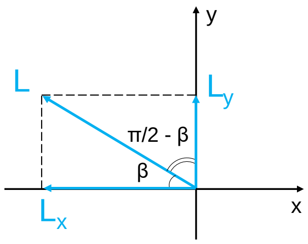

Figure 4. Lift Force Components

$$D_y = D\sin\left(\frac{\pi}{2} - \beta\right) \#(11)$$

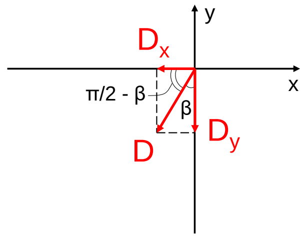

Figure 5. Drag Force Components

and summing only their components in the y-direction, we obtain:

$$F_{Thrust} = L\cos\left(\frac{\pi}{2} - \beta\right) - D\sin\left(\frac{\pi}{2} - \beta\right) \quad (12)$$

Substituting in the corresponding equations for Lift and Drag (Fig. 6) gives:

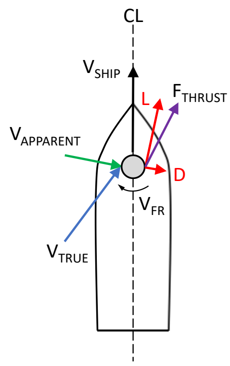

Figure 6. Basic wind directions and resultant forces vectors

$$F_{Thrust} = \frac{1}{2}\rho A V_a^2 [C_L(\sin\beta) - C_D(\cos\beta)] \ (13)$$

4. FLETTNER ROTOR POWER CALCULATIONS

Calculations yielded the expected power produced by a single Flettner Rotor in different wind speed and wind direction conditions to maintain a constant ship

Journal of Marine Technology and Environment
DOI:10.53464/JMTE.02.2026.08
ISSN (Print): 1844-6116
ISSN (Online): 2501-8795
https://www. jmte.eu

direction (heading) and speed. Additionally, the power required to rotate the Flettner Rotor was calculated (as electrical motor power consumption). This electrical motor power was then subtracted from the raw generated power by the Flettner Rotor. The remaining produced power by the Flettner Rotor is considered as replacement (or augmentation) power to the normally operating Diesel engine used to propel the ship along its charted heading and speed. The contributed power by the Flettner Rotor was compared to the total required ship propulsion power.

A set of calculations for a typical Flettner rotor application illustrates the expected benefits of the proposed hybrid propulsion system. Based on the total Lift and Drag due to the rotating Flettner Rotor, the power delivered by the Flettner Rotor (FR), $P_{L\&D}$ is shown in (14). The power, P_{motor}, consumed by an electric motor to rotate the FR is shown in (15).

$$P_{L\&D} = (L + D)V_{ship} \quad (14)$$

$$P_{motor} = \frac{1}{2}\rho A V_a^3 C_M \alpha \quad (15)$$

This power (15) is added as an additional load to the overall ship electrical load system. The power contribution from the FR, (i.e., “net power”) to the overall ship power, P_{FRprop} shown in (16).

$$P_{FRprop} = P_{L\&D} - P_{motor} \quad (16)$$

The assumed lift coefficient, C_L = 12.5, and drag coefficient, C_D = 0.2, were based on a prior study [10] The assumed moment coefficient, C_M = 0.2, was based on the original work by Flettner [13].

In our work we modelled a Flettner Rotor with no end plates. Configurations using FRs with end plates will generally show improved results, hence, our initial assumptions are conservative.

The selected FR geometry is as follows:

A – vertical projected cross-sectional area of FR (i.e., *h x d*, *h* = FR height; *d* = FR diameter)

h = 35 m; *d* = 5 m; *h/d* = 7; *A* = *h x d* = 35 m x 5 m = 175 m^2;

SR – spin ratio α (ratio of FR surface tangential speed, V_{FR}, to apparent wind speed, V_a) = 0.5 – 4.0 (for a correlation of FR surface tangential speed, V_{FR}, to FR rotational speed, ω_{FR}, please see Table 1). The formula used to convert from V_{FR} (m/s) to ω_{FR} (rpm) is:

$$\omega_{FR} = \frac{V_{FR}}{0.5(FR_d)}(60) \quad (17)$$

A summary of results for a fixed FR_h = 30 m, FR_d = 5 m, *h/d* = 6, and variable surface tangential speeds, V_{FR}, is shown in Table 1. Conversion of ship speed, V_{ship}, true wind speed, V_{true}, or apparent wind speed, V_a, is done according to the relationship: 1 m/s = 1.9438 kn.

Table 1. Various operating speeds for FR installation

				Tangential	V_{FR} / V_a					Rotational
V_{true}, kn	V_{true}, m/s	V_{ship}, m/s	V_a, m/s	V_{FR}, m/s	*SR*	FR_h, m	FR_d, m	*h/d*	*A*, m^2	ω_{FR}, rpm
11.7	6.0	4.5	1.5	5	3.33	30	5	6	150	120
14.6	7.5	4.5	3	10	3.33	30	5	6	150	240
17.5	9.0	4.5	4.5	15	3.33	30	5	6	150	360
20.4	10.5	4.5	6	20	3.33	30	5	6	150	480
23.3	12.0	4.5	7.5	25	3.33	30	5	6	150	600
26.2	13.5	4.5	9	30	3.33	30	5	6	150	720
29.2	15.0	4.5	10.5	35	3.33	30	5	6	150	840

V_{ship} = ship’s velocity vector; V_{true} = true wind speed; V_a = apparent wind speed = V_{true} – $V_{ship;}$ ρ – density of air (assume value at T = 20°C, 1 atm) = 1.205 kg/m^3; FR surface area = $h \; x \; \pi \; x \; d$ = 35 m x π x 5 m = 549.8 m^2 ≈ 550 m^2.

Further assumptions for ship operational parameters include SFC = 180 g/kW-h using Bunker Heavy Fuel Oil (HFO) at a price of USD 650/ton. For the purpose a typical small general cargo ship (approx. 5500 dwt) was considered, operating at slow steaming speed. The resulting average ship propulsion power was approx. 1100 kW for average ship speed of 8.8 kn (4.5 m/s). The assumed average sea voyage distance was 2000 nm with an average voyage duration of approx. 10 days (240 h).

5. MOST LIKELY WIND SPEEDS (TRUE WIND SPEED) CALCULATIONS

A recent IMO publication [14] provides information on major global shipping routes (Ibid., Fig. 9) and statistical distribution of prevailing sea winds (Ibid., Fig. 10) along global shipping routes. Hence, consistent with this IMO guidance [14], the selected wind conditions (speeds) for our example were: V_{true} = 10.5 m/s; V_{ship} = 4.5 m/s; V_a = V_{true} – V_{ship} = 6 m/s, for a Flettner rotor surface tangential speed V_{FR} = 20 m/s; and a resulting spin ratio, SR = V_{FR}/V_a = 20/6 = 3.33. Recalculating the resulting Lift, *L*, and Drag, *D*, forces, and resulting *L/D* ratio is shown in (18), (19), and (20), respectively.

$$L = \frac{1}{2}\rho A V_a^2 C_L = \frac{1}{2}\left[\left(1.205\frac{kg}{m^3}\right)(175m^2)\left(6\frac{m}{s}\right)^2(12.5)\right] = 47446.9\,N \# (18)$$

$$D = \frac{1}{2}\rho A V_a^2 C_D = \frac{1}{2}\left[\left(1.205\frac{kg}{m^3}\right)(175m^2)\left(6\frac{m}{s}\right)^2(0.2)\right] = 759.2\,N \# (19)$$

$$\frac{L}{D} = \frac{47446.9}{759.2} = 62.5 \quad (20)$$

The power delivered by the Flettner Rotor (FR), $P_{L\&D}$ is shown in (21). The power consumed by an electric motor to rotate the FR, P_{motor} is shown in (22). Power contribution from the FR, P_{FRprop} is shown in (23).

$$P_{L\&D} = (L + D)V_{Ship} = (47446.9\,N + 759.2\,N)\left(4.5\frac{m}{s}\right) = 216927.5\,W \# (21)$$

Journal of Marine Technology and Environment
DOI:10.53464/JMTE.02.2026.08
ISSN (Print): 1844-6116
ISSN (Online): 2501-8795
https://www. jmte.eu

$$P_{motor} = \frac{1}{2}\rho A V_a^3 C_M \alpha = \frac{1}{2}\left[\left(1.205\frac{kg}{m^3}\right)(175m^2)\left(6\frac{m}{s}\right)^3(0.2)(3.33)\right] = 15168\ W \#(22)$$

$$P_{FRprop} = P_{L\&D} - P_{motor} = 201.7\ kW \quad (23)$$

These results are consistent with recently published similar estimates (Fig. 3, p. 9 of [15]) for a ship using: V_{ship} = 14 kn, V_{true} = 10 m/s, d/h = 4.76, SR = 3.

Average power contribution (%) from FR, $P_{FRprop,\%}$, to total ship power demand, P_{ship}:

$$P_{FRprop,\%} = \left(\frac{PP_{FRprop,\%}}{P_{ship}}\right)100\% = \left(\frac{201.7}{1100}\right)100\% = 18.33\% \#(24)$$

6. SHIP ENGINE EMISSIONS REDUCTION CALCULATIONS

The annual reduction in emissions due to using Flettner Rotor (AER_{FR}) is calculated by Eq. 25 [16]:

$$AER_{FR} = \sum_{i=1}^{i=n} N_{FR}\, P_{FR} F_e H \#(25)$$

where:

N_{FR} – number of FRs used; P_{FR} – net power provided by FR(s) to main engine propulsion; F_e – emission factors (energy based), g/kW-h; H – sailing hours per year.

Exhaust emissions from marine diesel engines consist mostly of N_2, O_2, CO_2, H_2O and with smaller quantities of CO, SOx, NOx, partially reacted/non-fully burned HCs and PM, as well as a group of trace pollutants named, known as micro pollutants. Next, we consider each of these emission species.

6.1 Exhaust gas emission species

NOx

Oxides of Nitrogen resulting for the oxidation of molecular nitrogen (N_2) in the combustion chamber and partially due to incomplete combustion are grouped as “NOx” to include various compounds: nitric oxide (NO), dinitrogen dioxide (N_2O_2), nitrogen dioxide (NO_2), etc. In addition to their high toxicity, NOx emissions combined with volatile organic compounds (VOCs) result in photochemical reactions leading to increased tropospheric ozone (O_3) levels [17]. These increased tropospheric O_3 levels are detrimental to plant vegetation. Global warming is particularly affected by the depletion of stratospheric O_3, due to another NOx emission (from nitrous oxide, N_2O).

SOx

Oxides of Sulphur due to Sulphur content in combusted fuel are grouped under “SOx” [18] to include Sulphur monoxide (SO), Sulphur dioxide (SO_2), di-Sulphur monoxide (S_2O), and Sulphur trioxide (SO_3). Similar to NOx, SO_2 emissions are detrimental to plant vegetation. Emissions regulations for SOx are becoming more stringent as lower Sulphur content in marine fuels is demanded. Alternative ways to reducing SOx emissions have been discussed in regulation 14 of IMOs’ MARPOL Annex VI legislation [5].

CO

Carbon monoxide (CO) formation is due to incomplete combustion (as function of excess oxidizer, among other parameters) in diesel engines. Typically, CO emissions are low, in well-maintained diesel engines. However, the CO’s relative concentration can increase significantly when diesel engines are not running optimally (and/or are poorly maintained). CO emissions have adverse health effects on humans causing respiratory issues. The effect of CO on global warming is relatively small.

CO_2

Carbon dioxide (CO_2) emissions result from the fuel being burned in diesel engines. The quantity of fuel burned is proportional to the engine power, and on a global scale, this has been increasing as shipping traffic is growing steadily through recent years. CO_2 has received increased attention lately due to its role as a GHG and its effect on global warming. IMO’s EEDI legislation (in effect since 2013) has mandated strict lower EEDI limits to newly built ships compared to existing ships’ EEDI indexes. As the global economy relies on shipping for over 90% of its trade, increased shipping will lead to commensurately higher CO_2 emissions, which, in turn, will continue to impact negatively global warming.

HC

Hydrocarbon (HC) emissions, which include various combinations of C, H, O, N, and S, result from partially burned fuel in the diesel engine. The concentration of HC emissions is also dependent on the specific engine operational load. HC emissions can be involved in the formation of photochemical smog and tropospheric O_3 thus affecting global warming.

PM

Particulate matter (PM) emissions (generally regarded as “soot”) resulting from incomplete (partial) combustion processes of HC fuels contain a mixture of inorganic and organic substances. In diesel engines, PM tend to be very small, in the order of sub-μm (i.e., < 1 x 10^{-6} m) in diameter, which contributes to their easy

Journal of Marine Technology and Environment
DOI:10.53464/JMTE.02.2026.08
ISSN (Print): 1844-6116
ISSN (Online): 2501-8795
https://www. jmte.eu

dispersal. Other versions of PM, as quantified by their statistically predominant diameter of approx. 10 μm (i.e., PM_{10}) have been characterized. The sooting tendency in combustion depends on the type of flames (i.e., premixed vs. diffusion), operational flame temperature (i.e., "cool" vs "hot), etc. It is a complicated process whose details are beyond the scope of this study. A detailed review has been published elsewhere [18].

MPs

The last (and smallest) group of emission pollutants, i.e., micro pollutants, consists of trace constituents (typically in ppb[1] levels), but which can still demonstrate sever adverse environmental effects even at these diminished concentrations. In the context of diesel engines emissions, micro pollutants include organic trace pollutants and heavy metals [17]. The organic micro pollutants include polyaromatic hydrocarbons (PAH), polychlorinated biphenyls (PCB), polychlorinated dibenzodioxins (PCDD), and polychlorinated dibenzofurans (PCDF). The group of heavy metals includes many transition metals[2] such as Cd, Cr, Cu, Hg, Ni and Zn; and some non-transition metals[3] such as Pb and the metalloids As and Se. Due to the very low (trace) amounts of these micro pollutants we will not consider them in our analyses. Further details in photochemistry of air pollution can be found elsewhere [19].

6.2 *Exhaust gas emission factors*

The following values for exhaust gas emission factors, F_e, were used (in units of g/kW-H): NOx = 18.1; SOx = 10.29; CO = 1.4; CO_2 = 620.62; HC = 0.6; PM = 1.42 [16]. These annual emissions reduction values (AER) appeared to be consistently updated from the earlier AER values [20]: NOx = 17; SOx = 10; CO = 1.4; CO_2 = 655; HC = 0.6; PM = 1.25. In this same earlier work [20], the AER value for SOx was based on an assumed average fuel-sulphur content of 2.5% for HFO.

Compared to the above emission values for NOx (rather dated at 18.1 g/kW-h), IMO's NOx limits have been dropping considerably from 17.0 g/kW-h (2000) to about 3.4 g/kW-h (2016), and with a continued tendency to further restrictions [21]. These NOx weighted cycle emission limits are based on ship engine's rated speed (rpm). In our case, we have selected the NOx limits for large 2-cycle turbocharged crosshead diesel engines, with rated speeds under 130 rpm. At the same time, marine engine makers have been developing strategies for newly built ships (post-2000) to comply with IMO's stringent limits by introducing water in the combustion chamber, or by humidifying the intake air (approx. 4 g/kW-h). Further NOx reductions are achieved by applying Selective Catalytic Reactor (SCR) technologies [22] to reach even lower emissions (< 2 g/kW-h).

6.3 *Global ship utilization*

Global merchant ships utilization generally varies with prevailing global freight rates. Assuming low freight rates, hence low annual ship utilization (say, 60%), i.e., 5256 engine hours/year, or high freight rates, hence high annual ship utilization (80%), i.e., 7008 engine hours/year, one can choose an appropriate estimated average of, say, 70% annual ship utilization, i.e., 6132 engine hours/year. These values are generally consistent with the prior estimates [20] of 5500, 6500, and 7010 engine hours/year. In our example we use the average value of 6500 engine hours/year. This is a reasonable average value of (approx. 70%) annual ship utilization consistent with prior works [23].

More detailed analyses [24] based on geographic specification of global ship activities and average annual usage derived from the publicly available International Comprehensive Ocean-Atmosphere Data Set (ICOADS) and the U.S. Coast Guard's own data set Automated Mutual-Assistance Vessel Rescue System (AMVER) were, in general, consistent with the earlier findings [23]. Furthermore, these authors [23] adjusted their estimates for average annual ship utilization accordingly based on related feedback from colleagues [25].

6.4 *Reductions in ship main engine exhaust emissions - example*

Calculations for the reduction in each of the emissions species separately (on an annual basis), NOx, SOx, CO, CO_2, HC, and PM are shown in equations (26), (27), (28), (29), (30), and (31), respectively.

$$\sum_{i=1}^{i=n} N_{FR}\, P_{FR} F_e H = (1)(201.7\ kW)\left(18.1\ \frac{g}{kW-h}\right)(6500\ h)\left(\frac{1\ ton}{1\ x\ 10^6\ g}\right) = 23.73\ tons \quad \#(26)$$

$$\sum_{i=1}^{i=n} N_{FR}\, P_{FR} F_e H = (1)(201.7\ kW)\left(10.3\ \frac{g}{kW-h}\right)(6500\ h)\left(\frac{1\ ton}{1\ x\ 10^6\ g}\right) = 13.51\ tons \quad \#(27)$$

$$\sum_{i=1}^{i=n} N_{FR}\, P_{FR} F_e H = (1)(201.7\ kW)\left(1.4\ \frac{g}{kW-h}\right)(6500\ h)\left(\frac{1\ ton}{1\ x\ 10^6\ g}\right) = 1.84\ tons \quad \#(28)$$

$$\sum_{i=1}^{i=n} N_{FR}\, P_{FR} F_e H = (1)(201.7\ kW)\left(620.62\ \frac{g}{kW-h}\right)(6500\ h)\left(\frac{1\ ton}{1\ x\ 10^6\ g}\right) = 813.66\ tons \quad \#(29)$$

$$\sum_{i=1}^{i=n} N_{FR}\, P_{FR} F_e H = (1)(201.7\ kW)\left(0.6\ \frac{g}{kW-h}\right)(6500\ h)\left(\frac{1\ ton}{1\ x\ 10^6\ g}\right) = 0.79\ tons \quad \#(30)$$

[1] ppb = parts per billion, i.e., 1 x 10^{-9} concentration

[2] Transition metals are found in the "d-block" of the Periodic Table (groups 3 to 12)

[3] Non-ttransition metals are found in the "s-block" (groups 1 and 2) and "p-block" (groups 13 to 18) of the Periodic Table

Journal of Marine
Technology and Environment
DOI:10.53464/JMTE.02.2026.08
ISSN (Print): 1844-6116
ISSN (Online): 2501-8795
https://www.jmte.eu

$$\sum_{i=1}^{i=n} N_{FR} P_{FR} F_e H = (1)(201.7\ kW)\left(1.42\ \frac{g}{kW-h}\right)(6500\ h)\left(\frac{1\ ton}{1\ x\ 10^6\ g}\right) = 1.86\ tons \ \#(31)$$

The effects of using one Flettner Rotor for a ship speed of 4.5 m/s (8.8 kn.), for various wind direction angles (0° – 360°) on the annual emissions reduction are shown in Fig. 7 (CO_2), Fig. 8 (NOx (upper trace) and SOx (lower trace)), and Fig. 9 (CO (upper trace) and HC (lower trace)). Due to some uncertainty in the estimated and measured approaches for PM, no PM data were plotted. In general, however, annual PM emissions reduction followed closely the CO emissions reduction curve (Fig. 9, upper trace).

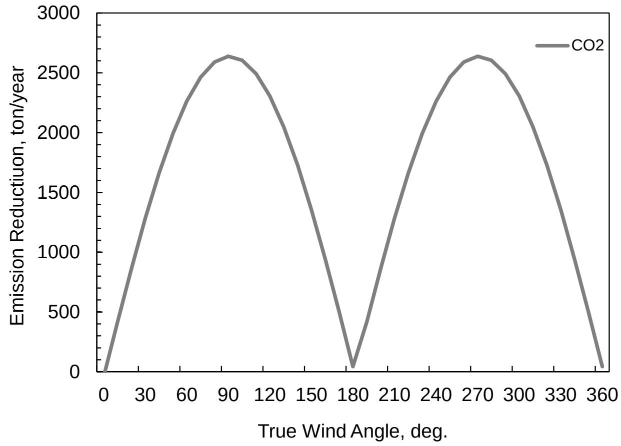

Figure 7. CO_2 Emissions Reduction

The highest emissions reduction occurs at true wind speed angles of approx. 90° and 270°. This is consistent with the occurrence of the FR's maximum lift force and resulting net output power along the intended movement direction (heading) of the ship. Even at close angles to the wind (close-hauled), at say, 25°-35°, and at high angles before the bind (running), at say, 145°-155°, the emissions reduction is already significant (across all emission species). Conversely, the lowest emissions reduction is shown near 0° (head wind) and 360° (tail wind).

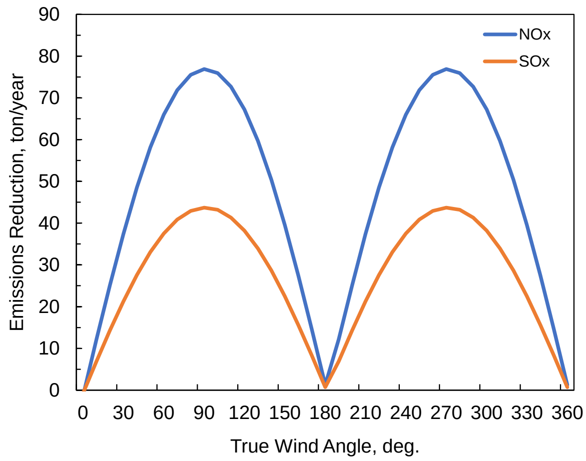

Figure 8. NOx and SOx Emissions Reductions

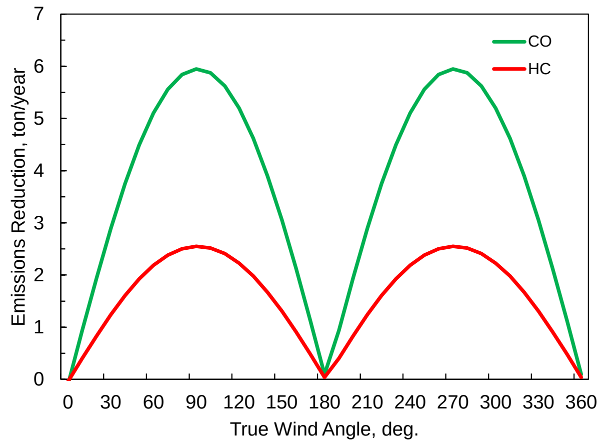

Figure 9. CO and HC Emissions Reductions

In these instances, the sensible operational suggestion may be to depower (and/or stow away where possible) the Flettner Rotor and operate the ship entirely on diesel power. At these true wind directions (0° and 360°) there is no effective power extracted by the Flettner Rotor as shown in the previous related work [6].

Journal of Marine Technology and Environment
DOI:10.53464/JMTE.02.2026.08
ISSN (Print): 1844-6116
ISSN (Online): 2501-8795
https://www. jmte.eu

7. CONCLUSIONS

Consistent with our prior work CFD analyses, a directly proportional relationship between Flettner rotor rotational speed and resulting lift was confirmed. The resulting optimal L/D ratio appears to be optimized at true wind speeds of approx. 10 to 15 m/s.

For a typical predominant true wind speed of about 10.5 m/s, we demonstrated optimal performance and significant reduction in exhaust emissions (near true wind speed angles of approx. 90° and 270°) form a typical Diesel main engine, when an operational Flettner rotor is used in a hybrid mode application (Diesel-electric propulsion).

8. ACKNOWLEDGMENTS

The author welcomes any related comments on improving the contents of this paper, as well as suggestions for any future related follow-on papers.

9. CREDIT AUTHORS STATEMENT

Conceptualization: R.L.; Investigation: R.L.; Methodology: R.L.; Resources: R.L.; Visualization: R.L.; Writing – original draft: R.L.; Writing – review & editing: R.L.

9. REFERENCES

[1] *Janes Sea Module Global Shipping Database*, 2024, May 13, https://customer.janes.com/portal/Account/PreAuthenticate?callingurl=https%3A%2F%2Fcustomer.janes.com%2

[2] Smith, T.W.P., et al., 2105, *Third IMO Greenhouse Gas Study 2014* – Executive Summary and Final Report, London, UK.

[3] Fiber, J. et al., 2021, *Fourth IMO GHG Study 2020* – Executive Summary and Final Report, London, UK.

[4] *EPA. United States Environmental Protection Agency. Overview of Greenhouse Gases*, 2026, April 27, https://www.epa.gov/ghgemissions/overview-greenhouse-gases

[5] MARPOL, 1997, *Annex VI*, IMO, London, UK.

[6] Almadani, Z., Garcia-Billings, J., Newsom, H., Ribarov, L.A., 2023, Flettner Rotor-Powered Marine Vessel – Design Evaluation and Systems Optimization. *Sustainability in Ship Design and Operations (SISDO 2023) Conference*, Glen Cove, NY.

[7] Lopes, A. M. G., 2016, A 2D Software System to Expedite Analysis of CFD Problems in Complex Geometries. *Comp. Appl. Eng. Educ.*, 24(1), 27–38

[8] Çengel, Y.A., Cimbala, J.M., 2014, *Fluid Mechanics*. 4th ed. McGraw Hill, New York, NY, USA.

[9] Anderson, J.D.**,** 2005, *Introduction to Flight*. McGraw-Hill Education, New York, NY, USA.

[10] Craft, T.J., Iacovides, H., Johnson, N., Launder, B., 2012, Back to the Future: Flettner-Thom Rotors for Maritime Propulsion? *Turb., Heat and Mass Trans*., (7), 1–10.

[11] Houghton, E.L., Carpenter, P.W., 2003, *Aerodynamics for Engineering Students*. Butterworth-Heinemann, Oxford, UK.

[12] Airfoil Tools (NACA 0024) – Cl/Cd v Alpha http://airfoiltools.com/airfoil/details?airfoil=naca0024-il

[13] Flettner, A., 1926, *Mein Weg zum Rotor. ("The Story of the Rotor") MIT 114 ABB. Verlag Koehler & Amelang, Leipzig 1926. 123 S*. ZAMM - Journal of Applied Mathematics and Mechanics / Zeitschrift Für Angewandte Mathematik Und Mechanik, 6(6), 505–505. doi.org/10.1002/zamm.19260060625.

[14] *IMO MEPC.1/Circ.896*, 2021, London, UK.

[15] Vigna, V., Figari, M., 2023, *Wind-Assisted Ship Propulsion: Matching Flettner Rotors with Diesel Engines and Controllable Pitch Propellers*. J. Mar. Sci. Eng., 11(1072), 1–18.

[16] Seddiek, I., Ammar, N.R., 2021, *Harnessing Wind Energy on Merchant Ships: Case Study Flettner Rotors onboard Bulk Carriers*. Env. Sci. and Pollution Res., (28), 32695–32707.

[17] Kristiansen, H.O., 2017, *Energy Demand and Exhaust Gas Emissions of Marine Engines. Project no. 2016-108: Update of Decision Support System for Exhaust Gas Emissions Calculations*. Report no.5. Technical University of Denmark (DTU).

[18] Glassman, I., 1996, *Combustion*. 3rd ed. Academic Press, San Diego, CA, USA.

[19] Leighton, P.A., 1961, *Photochemistry of Air Pollution*. Academic Press, New York.

DOI:10.53464/JMTE.02.2026.08
ISSN (Print): 1844-6116
ISSN (Online): 2501-8795
https://www.jmte.eu

[20] Corbett, J.J., Koehler, H.W., 2003, *Updated Emissions from Ocean Shipping.* J. of Geophys. Res., 108(D20):4650, doi:10.1029/2003JD003751.

[21] IMO Nitrogen Oxides (NOx) – Regulation 13 (https://www.imo.org/en/OurWork/Environment/Pages/Nitrogen-oxides-(NOx)-%E2%80%93-Regulation-13.aspx).

[22] Koehler, H.W., 2003, *NOx Emissions from Merchant Ships*. Marine Reporter & Eng. News, (June 2003), 68-70.

[23] Corbett, J.J., Koehler, H.W., 2004, *Considering Alternative Input Parameters in an Activity-Based Ship Fuel Consumption and Emission Model: Reply to Comment by Øyvind Endersen et al on "Updated Emissions from Ocean Shipping*." J. of Geophys. Res.,109(D23303):4650,doi:10.1029/2004JD005030.

[24] Endresen, Ø, Søgård, E., Sundet, J.K., Dalsøren, S.B., Isaksen, I.S.A., Berglen, T.F., Gravir, G., 2003, *Emission from International Sea Transportation and Environmental Impact.* Journal of Geophysical Research, 108(D17), 4560. doi:10.1029/2002JD002898.

[25] Endresen, Ø, Søgård, E., Bakke, J., Isaksen, I.S.A., 2004, *Substantiation of a Lower Estimate for the Bunker Inventory: Comment on "Updated Emissions from Ocean Shipping*" by J. J. Corbett and H.W. Koehler. J. of Geophys. Res., 109(D23302), 4560. doi:10.1029/2004JD004853.

Journal of Marine Technology and Environment
DOI:10.53464/JMTE.02.2026.09
ISSN (Print): 1844-6116
ISSN (Online): 2501-8795
https://www. jmte.eu

DESIGN AND IMPLEMENTATION OF AN APPLICATION FOR SMART PARKING MANAGEMENT

Petre-Iustin SCHIFÎRNEȚ [1], Mihaela BARHALESCU[2]

[1] Petroleum-Gas University of Ploiești Faculty of Mechanical and Electrical Engineering – Automation and Applied Informatics, e-mail address:Iustin_petre21@yahoo.com;
[2] Constanta Maritime University, Faculty of Naval Electro-Mechanics, 104 Mircea cel Batran Street, 900663, Constanta, Romania, e-mail address:mihaela.barhalescu@cmu-edu.eu

Abstract : A smart parking management application uses IoT sensors, cloud databases, and a mobile app to help drivers find and reserve open parking spots in real time. An intelligent parking system can help drivers in finding parking slots by providing real-time information.This paper addresses two common issues in urban parking: the lack of real-time information about available parking spots and the difficulty of locating the exact available one. The proposed solution consists of a smart parking system based on IR sensors, an ESP32 microcontroller, and two web applications: one allows users to view available spots and report problems, while the other enables administrators to control the barriers both automatically and manually via Firebase.

Key words : Design, ESP32 microcontroller, Firebase Real time Database, implementation, IR sensor, smart parking management, urban life.

1. INTRODUCTION

Parking is often seen as a frustrating part of daily urban life. Drivers frequently waste time circling around crowded lots, hoping to find a free spot. Even when digital signs indicate that spaces are available, locating the exact free spot can be nearly impossible, especially in large parking areas.

These issues lead to delays, stress, traffic congestion, and in some cases, missed appointments or work hours [1-4].

This project aims to address these everyday frustrations by designing and implementing an intelligent parking management system.

The solution provides real-time information about the availability of parking spots and automates barrier control to improve flow and reduce human intervention [5].

At the core of the system is an ESP32 microcontroller, which collects data from infrared (IR) sensors installed in each parking space. The ESP32 processes the data and sends a binary code representing the state of each spot to a Firebase Real time Database via Wi-Fi. This allows seamless synchronization with two dedicated web applications: one for users to view parking availability and report issues, and another for administrators to manually control the barriers and monitor the system [6].

2. HARDWARE SYSTEM DESIGN

The hardware structure of the smart parking system consists of several electronic components working together to detect the presence of vehicles, control access through entry and exit barriers, and exchange data with an online database. The central component is the ESP32 microcontroller. It features multiple digital and analogue input/output pins and built-in Wi-Fi connectivity [7]. The ESP32 continuously monitors the state of the connected sensors, processes their input, and transmits structured data to the Firebase Real time Database. It also receives commands from the administrator interface and triggers actions on the servomotors controlling the barriers. Internally, each pin of the ESP32 reads digital HIGH or LOW signals depending on the voltage it receives from external components. Each of the five parking spots is equipped with an infrared (IR) proximity sensor, which consists of an IR LED (emitter) and a phototransistor (receiver). When a vehicle is parked in front of the sensor, the infrared light emitted by the LED is reflected back toward the phototransistor. This reflection alters the current flowing through the phototransistor, pulling the output pin of the sensor to a LOW voltage level (typically under 1V) [8].

Journal of Marine
Technology and Environment
DOI:10.53464/JMTE.02.2026.09

ISSN (Print): 1844-6116
ISSN (Online): 2501-8795
https://www. jmte.eu

The ESP32 detects this change on the corresponding digital input pin and registers the spot as occupied. To prevent false readings caused by brief interferences such as people passing by or shadows, a simple method is implemented: the ESP32 checks if the signal remains in the LOW state for at least one second before confirming that the spot is truly occupied. If the signal returns to HIGH too quickly, it is ignored. In addition to these five sensors, two more IR sensors are placed near the entry and exit points of the parking lot.

These work similarly and are used to detect the presence of vehicles approaching the barriers. When the entry sensor detects a car, the ESP32 sends a signal to the corresponding servo motor to rotate to 90 degrees, lifting the barrier. Once the vehicle has passed and the sensor no longer detects an object, the ESP32 initiates a delay of one second, after which it sends a new signal to return the servo to 0 degrees, lowering the barrier. This delay ensures that the barrier does not close prematurely while the car is still passing.

The system uses two servo motors — one for the entrance and one for the exit. Each motor is connected to a separate PWM-capable pin on the ESP32. The ESP32 sends position values to the servo through pulse-width modulation (PWM) signals. A pulse of around 1.5 milliseconds corresponds to the neutral (midpoint) position, while longer or shorter pulses rotate the motor shaft to a specific angle. In this implementation, 0 degrees corresponds to the closed position of the barrier, and 90 degrees to the open position.

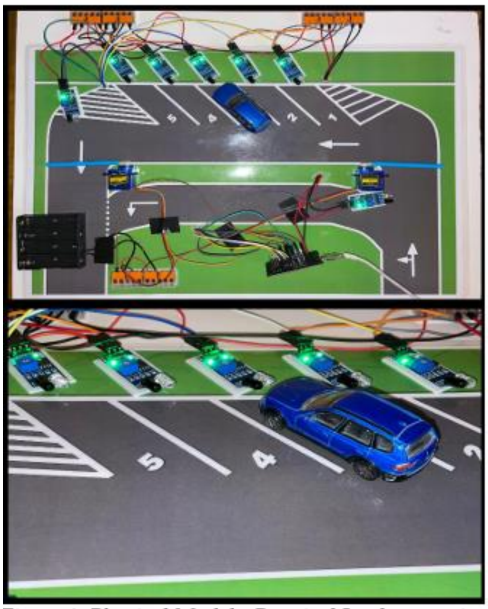

Figure 1 Physical Model - Practical Implementation

For one of the motors, the orientation required inverting the logic due to its physical mounting (Fig. 1).

3. ELECTRICAL CONNECTIONS

The power distribution for the system is designed to be modular and effective in supporting all connected components (Fig. 2).

The ESP32 microcontroller provides a 3.3V output and a common ground (GND), which are routed to a set of terminal blocks (WAGO-type). These connectors serve as distribution hubs, allowing the same voltage and ground lines to be shared efficiently across multiple devices without soldering or complex wiring. This setup simplifies maintenance and offers flexibility in future expansions or hardware replacements.

All seven IR sensors in the system, five for the individual parking spots and two for the entrance and exit proximity detection, are powered directly through these terminal connectors using the regulated 3.3V output of the ESP32.

As illustrated in Figure 1, this layout enables a clean and structured organization of the power lines.

The control wires, which carry the digital output signals from each IR sensor, are routed discretely underneath the surface of the physical parking model.

This decision was made to optimize the visual appearance and minimize physical interference with other components. Each of these signal wires is connected to a dedicated digital input pin on the ESP32, allowing individual monitoring of each sensor's state.

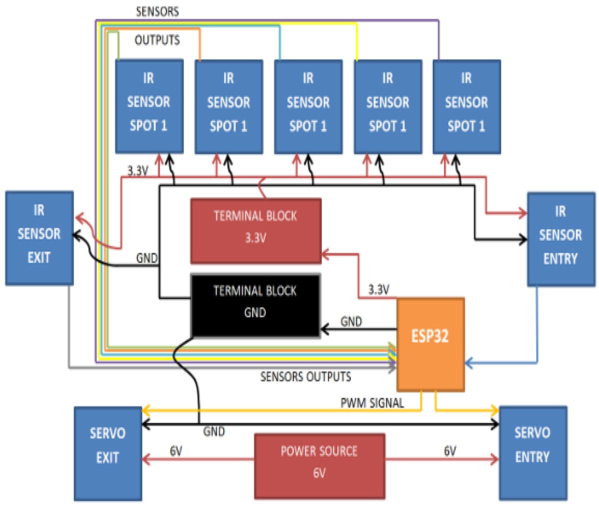

Figure 2 Electrical Schematic of the System

The servo motors used to actuate the entry and exit barriers operate at a higher current and voltage than the sensors, and therefore require a separate power source. A 6V DC supply is provided via a battery holder containing four AA batteries, delivering both sufficient voltage and current capacity to drive the motors smoothly.

Journal of Marine Technology and Environment
DOI:10.53464/JMTE.02.2026.09
ISSN (Print): 1844-6116
ISSN (Online): 2501-8795
https://www. jmte.eu

This design avoids drawing large currents from the ESP32's on board voltage regulator, which could cause system instability or resets during motor operation , and aligns with best practices for low-power microcontroller-based systems [9].

The servo motors share a common ground with the ESP32 to maintain proper signal reference, ensuring consistent response to the PWM control signals.

To provide a better understanding of the hardware implementation, Table 1 presents the complete list of components and their corresponding connections to the ESP32 microcontroller.

Table 1. Hardware Connections

Component	ESP32 Pin	Signal Type	Voltage (V)
IR Sensor 1 (Parking Spot 1)	5	Digital Input	3.3
IR Sensor 2 (Parking Spot 2)	18	Digital Input	3.3
IR Sensor 3 (Parking Spot 3)	19	Digital Input	3.3
IR Sensor 4 (Parking Spot 4)	21	Digital Input	3.3
IR Sensor 5 (Parking Spot 5)	27	Digital Input	3.3
IR Sensor - Entry	32	Digital Input	3.3
IR Sensor - Exit	23	Digital Input	3.3
Servo Motor - Entry Barrier	25	PWM Output	6 (external)
Servo Motor - Exit Barrier	26	PWM Output	6 (external)

4. SOFTWARE SYSTEM DESIGN

The software architecture of the smart parking system is based on the interaction between a microcontroller, a real-time cloud database, and two separate web applications. All components communicate through HTTP requests and real-time synchronization mechanisms to ensure data is updated efficiently and consistently, following a model similar to previously proposed IoT-based parking systems [10].

The central element of the system's data flow is the Firebase Real time Database. It acts as the bridge between hardware and software, storing all relevant information in real time [11]. The ESP32 microcontroller writes data to Firebase every two seconds, sending the binary code that represents the state of the five parking spots.

Additionally, it reads specific values from Firebase that determine the current mode of operation ("automatic" or "manual") and, if in manual mode, listens for commands to raise or lower the entry and exit barriers.

Firebase also receives reports from users and displays them in the administrator interface.

Communication between the ESP32 and Firebase is made via HTTPS requests using a secret authorization key.

The two web interfaces (user and admin) are hosted on GitHub Pages, providing a simple and reliable deployment method [12].

The websites use JavaScript to send and retrieve data from Firebase via RESTful API calls [13].

Data is fetched at a controlled interval (e.g., every 1 or 3 seconds), and optimizations are implemented to ensure that requests are only made while the browser tab is active, reducing unnecessary traffic and staying within Firebase's daily quota limits.

The interaction between hardware components, the Firebase database, and the two web interfaces is summarized in Figure 3, which illustrates the system's overall functionality and data flow.

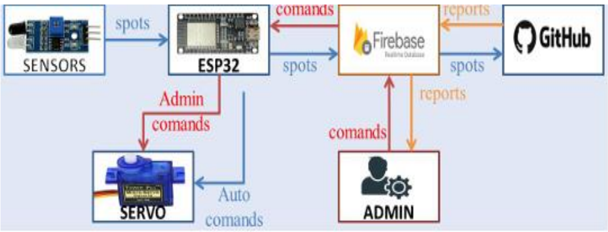

Figure 3 System Functionality Diagram

The user interface is focused on accessibility and real-time visualization. It displays the parking layout with live updates showing which spots are currently occupied. Changes in the parking state are highlighted using notifications, and the number of available spots is shown at the top of the screen. The interface is designed

Journal of Marine Technology and Environment
DOI:10.53464/JMTE.02.2026.09
ISSN (Print): 1844-6116
ISSN (Online): 2501-8795
https://www.jmte.eu

to be fully responsive, adapting its layout and design depending on the screen size, allowing users to access the system comfortably from both desktop and mobile devices (Fig. 4, Fig. 5).

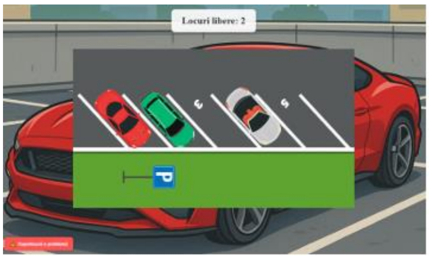

Figure 4 Desktop Application Interface

Additionally, the interface includes a simple report form that allows users to report issues such as blocked spots or malfunctioning barriers.

These reports are sent to Firebase and displayed for the administrator [14].

Figure 5 Mobile Application Interface

The admin interface provides full control and monitoring capabilities (Fig. 6).

Figure 6 Administration Page

Administrators can switch between automatic and manual operation modes, and in manual mode, can directly control the entry and exit barriers using action buttons.

All received user reports are displayed on the admin page, along with timestamps, and can be cleared after being handled.

The interface is password-protected and styled for clarity, making it easy to operate from any device.

5. CONCLUSIONS

This project demonstrates a functional and scalable solution to real-world parking challenges by combining simple hardware with cloud-based services and intuitive web interfaces.

By using infrared sensors, an ESP32 microcontroller, Firebase, and GitHub Pages, the system provides real-time parking availability updates and remote control of access barriers.

The modular design, low cost, and potential for future improvements, such as AI-based detection and online reservations, make this implementation both practical and adaptable for smart city applications.

6. ACKNOWLEDGMENTS

The authors bring thanks and gratitude to the Maritime University of Constanta for the financial support.

7. CREdit authors statement

Conceptualization: B.M., S.P.-I.;

Data curation: S.P.-I.;

Formal analysis: S.P.-I.;

Funding acquisition: B.M.;

Investigation: S.P.-I. B.M;

Methodology: S.P.-I. B.M;

Project administration: S.P.-I., B.M.;

Resources: B.M.;

Software: S.P.-I.;

Supervision: S.P.-I., B.M;

Validation: S.P.-I.;

Visualization: S.P.-I.;

Writing – original draft: S.P.-I.;

Writing – review & editing: S.P.-I..

8. REFERENCES

[1] Samar Alkhuraiji, 2020, *Design and Implementation of an Android Smart Parking Mobile Application*, TEM Journal, Volume 9, Issue 4, pp 1357-1363, ISSN 2217-8309, DOI: 10.18421/TEM94-06

[2] Kianpisheh, A., Mustaffa, N., Limtrairut, P., &Keikhosrokiani, P., 2012, *Smart parking system(SPS) architecture using ultrasonicdetector*. International Journal of Software Engineering and Its Applications, vol. 6(3),pp 55-58.

[3] Thangam, E. C., Mohan, M., Ganesh, J., & Sukesh, C.V, 2018, *Internet of Things (IoT) based smartparking reservation system using raspberry-pi*, International Journal of Applied EngineeringResearch, vol. 13(8), pp 5759-5765.

[4] Hanumanthakari, S., 2024, *Intelligent and real-time Parking System*. In: E3S Web of Conferences 472, 03003

[5] Anand R., Khanna A., 2016, *IoT based smart parking system*. In: 2016 International Conference on Internet of Things and Applications (IOTA).

[6] Sadhukhan, P., 2017, *An IoT-based E-parking system for smart cities*. In: International Conference on Advances in Computing, Communications and Informatics (ICACCI).

[7] Espressif Systems, 2023, ESP32 Technical Reference Manual, https://www.espressif.com.

[8] Bucur, G., *Tehnici de măsurare. Senzori şi traductoare de mărimi neelectrice*. Sisteme pentru măsurat mărimi neelectrice, Ploieşti, Editura UPG, 2010.

[9] Burd T.D., Brodersen R.W., Energy Efficient Microprocessor Design, Springer, 2012.

[10] Anand R., Khanna A., 2016, *IoT based smart parking system*. In: 2016 International Conference on Internet of Things and Applications (IOTA).

[11] Google Firebase, 2025, Firebase Realtime Database Documentation, https://firebase.google.com/docs/database.

[12] GitHub, 2025, GitHub Pages Documentation, https://docs.github.com/en/pages.

[13] Mozilla Developer Network, 2025, JavaScript Fetch API Guide, https://developer.mozilla.org/en-US/docs/Web/API/Fetch_API.

[14] Andrei, G., 2021, *Approaches based on artificial intelligence for water supply system*, Journal of Marine Technology and Environment, Vol.1, pp 5-9, Nautica publish House, Constanta, Romania

.

Journal of Marine Technology and Environment
DOI:10.53464/JMTE.02.2026.10
ISSN (Print): 1844-6116
ISSN (Online): 2501-8795
https://www. jmte.eu

OPTIMAL INJECTOR SPRING DESIGN FOR MAN B&W AG ENGINE

Mihaela TUROF[1], George Gr. POPESCU [2]

[1]Constanta Maritime University, Faculty of Naval Electro-Mechanics, 104 Mircea cel Batran Street, 900663, Constanta, Romania, e-mail address: mihaela_turof@yahoo.com
[2] Doctoral School of Industrial Engineering and Robotics, National University of Science and Technology POLITEHNICA, 313 Splaiul Independenței, 060042 Bucharest, Romania, , e-mail address:george.gr.popescu@gmail.com

Abstract : The injector is the machine part that performs the function of atomizing the fuel and introducing it into the combustion chamber. Mechanical injection is used in almost all types of diesel engines.

Springs are machine parts that provide an elastic connection between certain parts or subassemblies of a machine. When designing and calculating springs, the number of parameters that must be taken into account is greater than the number of relationships between them. Various methods are used to adopt some parameters and the rest are calculated.

Thus, the dimensioning of a spring can be carried out partly on the basis of such methods and partly by strength calculations, knowing the load that loads the spring, the type of stress, the shape of the spring.

This paper presents a method for the optimal design of the spring that is part of a MAN B&W AG engine injector. The theoretical part of the paper includes notions related to the injection system, types of injection pumps and their role, as well as types of injectors.

The case study of the paper includes the components of the MAN B&W AG engine injector, then starting from the initial input data, the helical cylindrical compression spring for the injector was designed and the necessary checks were made to determine whether the chosen spring meets the technical requirements for operating the injector.
Key words : Injector, diesel engine, compression spring, spring parameters.

1. INTRODUCTION

The diesel engine is an internal combustion engine in which the fuel is ignited by the high temperature created by the compression of the air necessary for combustion, and not by the use of an auxiliary device, such as the spark plug in the case of a spark ignition engine.

The engine works on the basis of the Diesel cycle.[1]

The engine was named after German engineer Rudolf Diesel at the suggestion of his wife, Martha Diesel, who in 1895 advised him: Nenn ihn doch einfach Dieselmotor! ("*Just call it the Diesel engine*!"), thus making it easier for Diesel to find a name for the engine, which he invented in 1892 and patented on February 23, 1893. Diesel intended his engine to run on a wide range of fuels, including coal dust. Diesel presented his invention running at the 1900 World's Fair on peanut oil. [2]

A vital component of diesel engines is the speed governor, mechanical or electronic, which regulates the engine speed by correctly dosing the injected diesel fuel. Unlike spark ignition (Otto) engines, the amount of air sucked in is not controlled, which leads to engine overspeed. Mechanical governors use different mechanisms depending on the load and speed. Modern, electronically controlled engine governors control fuel injection and limit engine speed via a central control unit that constantly receives signals from sensors, correctly dosing the amount of diesel fuel injected.[1]

Precise control of injection timing is the secret to reducing fuel consumption and pollutant emissions. Injection timing is measured in crankshaft rotation angles before top dead center. For example, if the central control unit initiates injection 10 degrees before top dead center, this is an injection timing of 10 degrees. The optimal injection timing is determined by the design, speed and load of the respective engine. [1]

2. HISTORICAL SHIELD OF THE DEVELOPMENT MECHANICALLY AND ELECTRONICALLY CONTROLLED INJECTION

Journal of Marine Technology and Environment
DOI:10.53464/JMTE.02.2026.10
ISSN (Print): 1844-6116
ISSN (Online): 2501-8795
https://www. jmte.eu

Older engines used a mechanical pump and a valve mechanism driven by the crankshaft, usually via a chain or timing belt. These engines used simple injectors, with a valve and spring, that opened/closed at a certain fuel pressure. The pump consisted of a cylinder that compressed the diesel fuel and a disc-shaped valve that rotated at half the speed of the crankshaft. The valve had a single opening on one side, for the pressurized fuel and another for each injector. As it rotated, the valve disc distributed a precise amount of high-pressure fuel to each injector. The injector valve was actuated by the pressure of the injected diesel fuel as long as the disc delivered fuel to the respective cylinder. The engine speed was controlled by a third disc that rotated only a few degrees and was operated by a lever. This disc controlled the opening through which the fuel passed, thus dosing the amount of diesel fuel injected.

Old diesel engines could be started in reverse, by mistake, although they operated inefficiently due to the misaligned ignition sequence. This was usually the result of starting the car in the wrong gear.

Modern engines have an injection pump that provides the necessary injection pressure. Each injector is electromagnetically actuated by a central control unit, which allows precise control of the injection depending on the speed and load, resulting in increased performance and low consumption. The simpler technical solution of the pump-injector assembly has led to the construction of more reliable and quieter engines.[1]

In the case of the indirect injection diesel engine, the diesel fuel is not injected directly into the combustion chamber, but into a pre-chamber where combustion is initiated and then extends into the main combustion chamber, driven by the turbulence created. The system allows for quiet operation, and, since combustion is favoured by turbulence, the injection pressure can be lower, so high rotation speeds are allowed (up to 4000 rpm), much more suitable for cars. The pre-chamber had the disadvantage of high heat losses, which had to be borne by the cooling system, and of low combustion efficiency, up to 5-10% lower than direct injection engines. Almost all engines had to have a cold start system, such as glow plugs. Indirect injection engines were widely used in the automotive and marine industries from the early 1950s until the 1980s, when direct injection progressed significantly.

Indirect injection engines are cheaper and easier to build for industries where emissions are not a priority. Even with new electronically controlled injection systems, indirect injection engines are slowly being replaced by direct injection engines, which are much more efficient.

3. INJENCTION PUMPS

3.1 Types. Role. Description

The injection pump is the organ that gives the fuel the high pressure it needs to enter the combustion chamber of the engine cylinder at high speed.

The technical conditions for injection pumps are the following:

→ The amount of fuel injected into each cylinder must be constant and the same for all cylinders, not being allowed to vary over time or from cylinder to cylinder, for the same speed and load

→ The injection advance angle must not vary over time, for the same speed, it must be adjustable, increasing with increasing speed

→ The injection pressure must be as constant as possible throughout the injection period

→ The flow rate must be easily adjustable, and, for the same adjustment position, the amount of fuel injected at each stroke of the pumping element must not vary with the pump speed

→ The power consumption for driving the injection pump must be as low as possible

Injection systems can be classified into two groups:

→ the pulse injection system, in which the pressure necessary to atomize the fuel and introduce it into the combustion chamber is produced only at the moment of injection and lasts as long as the injection lasts;

→ the pressure accumulation injection system, in which the injection pump maintains the pressure necessary for atomization, at a constant value, in an accumulator, and the injection of fuel into the combustion chamber is controlled by another organ (the injector, which, as will be shown, performs the function of a valve with controlled opening, the duration of the opening representing the duration of the injection).

Injection pumps that are part of injection equipment have a complex and varied role. First, to obtain optimal characteristics of the fuel jet injected into the engine cylinder, injection pumps must develop very high discharge (injection) pressures (300…1100 bar and sometimes higher – for example, in injector pumps). Second, injection pumps must allow dosing the amount of fuel per cycle in accordance with the operating mode, while ensuring uniformity of the fuel dose in all cylinders of multi-cylinder engines. Third, injection pumps must ensure optimal injection advance, limitation of injection duration and optimal injection characteristic.

Also, injection pumps must be reliable, durable, have simple construction, low cost, and as simple to operate as possible.

The essential problem of injection pumps is the achievement of high injection pressures, required by the need for fine atomization of the fuel. These pressures can only be provided by piston pumps. For these values of injection pressure (hundreds of bars), however, special

Journal of Marine Technology and Environment
DOI:10.53464/JMTE.02.2026.10
ISSN (Print): 1844-6116
ISSN (Online): 2501-8795
https://www.jmte.eu

problems arise in connection with the precision of execution of the piston and cylinder of the pump, as well as with the sealing of this pair of parts from the external environment. The only way to effectively seal is to reduce the clearance between the piston and the cylinder of the pump to values of 1.5…3 μm and to practice an execution with an increased piston length in relation to its diameter. This involves fine grinding operations, with extremely tight deviations in shape (from the quality of surface processing and from their mutual position), as well as lapping operations and “pairing” of the piston with the cylinder, which thus become non-interchangeable. [5]

3.2. Operating principle

To carry out the injection process, the pump piston performs a suction stroke and a discharge stroke. The piston is driven rigidly in the discharge stroke by a profiled cam. This has the main advantage of being able to choose the piston movement law so as to ensure the optimal injection characteristic and to satisfy the conditions for good fuel atomization. For this reason, the piston drive with a profiled cam is currently almost universally used. The piston can also be driven elastically in the discharge stroke by a spring. However, with elastic drive, the piston movement law cannot be controlled; instead, the injection process is removed from the influence of the speed, which also favours the uniformity of the injected fuel doses at low speeds. [4]

The schematic diagram of a piston injection pump is shown in Figure 1 below. The pumping element consists of the cylinder (1) and the piston (2). The fuel is sucked, through the suction valve (3), into the space (C), when the piston moves in the suction stroke under the action of the spring (4). The movement of the piston in the discharge stroke takes place under the action of the cam (5) and the tappet (6). The fuel in the space (C) is compressed and discharged at pressures of hundreds of bars to the space (R), through the discharge valve (7).

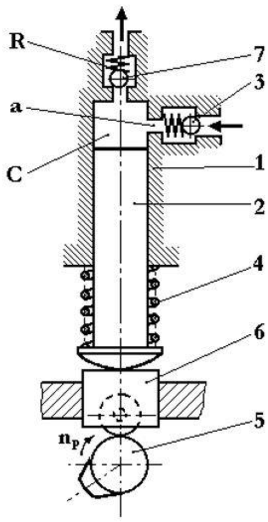

Figure 1 Schematic diagram of a piston injection pump [4]

The size of the discharged dose is established in accordance with the needs of the engine operating regime, by dividing the piston discharge stroke into a variable useful stroke s_u (Figure 2) and, most often, into two dead strokes s_m1 and s_m^{2}, one fixed and the other variable or both variable. The useful stroke s_u is usually placed in the maximum piston speed portion.

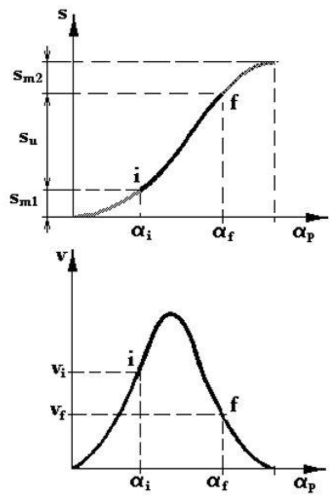

Figure 2 Engine operating mode [4]

In the form shown in figure 1., the piston injection pump discharges into space (R) the entire quantity of fuel sucked into space (C). To correlate the dose of fuel discharged with the engine operating mode, either the flow section (a) is externally controlled, or an axially movable variable profile cam is used.

Journal of Marine
Technology and Environment
DOI:10.53464/JMTE.02.2026.10
ISSN (Print): 1844-6116
ISSN (Online): 2501-8795
https://www. jmte.eu

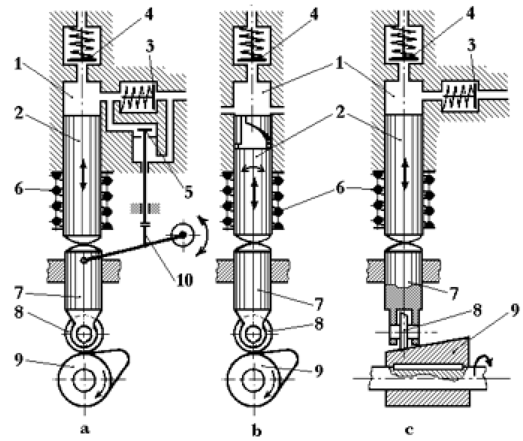

Figure 3 Types of valve pumps [4]
a-valve pump, with constant piston stroke
b-rotary plunger injection pump, with constant piston stroke
c-injection pump, with adjustable piston stroke

The composition and operation of the mentioned injection pumps (figure 3) is as follows: by rotating the cam (9) the roller (8) and the tappet (7) are activated, which determine the movement of the piston (2) and the pressing of the fuel in the cylinder (1). Through the discharge valve (4), the fuel pressed at the injection pressure level is sent to the injector. In the case of the injection pump in figure 3. a), the pressing is interrupted when the pressing valve (5) opens, operated by the regulating device (10).

Due to the potential energy of deformation of the spring (6), the piston (2) performs the filling stroke, the fuel enters the pump cylinder through the suction valve (3) in Figure 3. a) and c). In the piston-slide pump (figure 3. b), the suction valve (3) is missing, and the amount of fuel discharged is adjusted by rotating the piston (2). In the pump in Figure 3. c, the adjustment is made by axial movement of the cam (9).

In the case of the injection pumps in Figure 3. a) and b), only a fraction of the amount of fuel sucked into the cylinder (1) is discharged. These are pumps with invariable suction and partial discharge. Their main advantage is the discharge of fuel at high piston speeds. In this sense, the useful stroke s_u (figure 3. b) is placed between the dead strokes s_m1 and s_m2, where the speeds are reduced.

The pump in figure 3. c, is of the variable suction and total discharge type. The pump with a single discharge element and a rotary distributor, currently widespread in high-speed MACs used in road traction, is also built according to this principle of regulation. In these pumps, the fuel dose corresponding to each engine operating mode is sucked entirely into the suction space, after which it is completely discharged to the injector.

4. SPRINGS

4.1. Definition. Area of use

Springs are machine parts that create an elastic connection between certain parts or subassemblies of a machine. Due to their shape and the special mechanical characteristics of the materials they are made of, springs have the ability to deform under the action of an external force, taking over its mechanical work and storing it in the form of deformation energy. When the external load disappears, the stored energy is returned to the mechanical system of which the spring is a part.[6]

The fields of use of springs are varied, the most important being:

→ shock and vibration damping (in vehicle suspensions, elastic couplings, machinery foundations, etc.);

→ accumulation of energy that must be released gradually or in a short time (in spring clocks, internal combustion engine valve springs, etc.);

→ exerting a permanent, elastic force (in friction safety couplings, friction clutches, etc.);

→ regulating or limiting forces (in presses, control valves, etc.);

→ measuring forces and moments by using the dependence between load and deformation (dynamometric).

→ changing the natural frequencies of some machine parts.

4.2. Cylindrical compression coil springs

Figure 4 presents several solutions for helical compression springs, and Figure 5. presents the geometric elements of cylindrical helical compression springs with a round coil section.

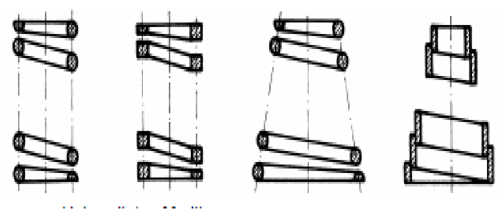

Figure 4 Types of compression coil springs [7]

Journal of Marine Technology and Environment
DOI:10.53464/JMTE.02.2026.10
ISSN (Print): 1844-6116
ISSN (Online): 2501-8795
https://www. jmte.eu

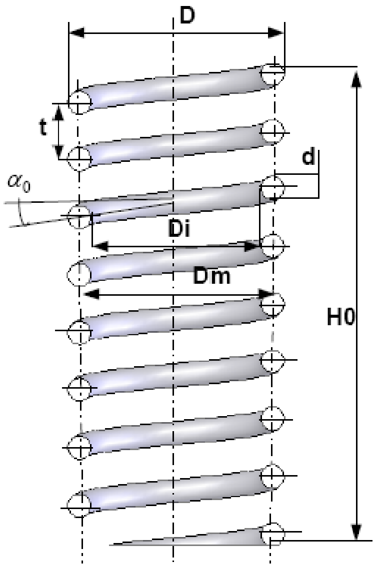

Figure 5 Geometric elements of cylindrical compression coil springs [7]

The terminology used for cylindrical compression helical springs with a round coil section (also applicable to a rectangular coil section) is:
d – diameter of the spring coil
D_i – inner diameter
D_m – average diameter
D – outer diameter
t – coil pitch
H_0 – length of the spring in the free state
α_0 – angle of inclination of the coil in the free state

5. OPTIMAL COMPRESSION SPRING DESIGN

5.1. Injector presentation

Compression springs are produced according to quality standards regulated by DIN 2095 in a wide variety of sizes.

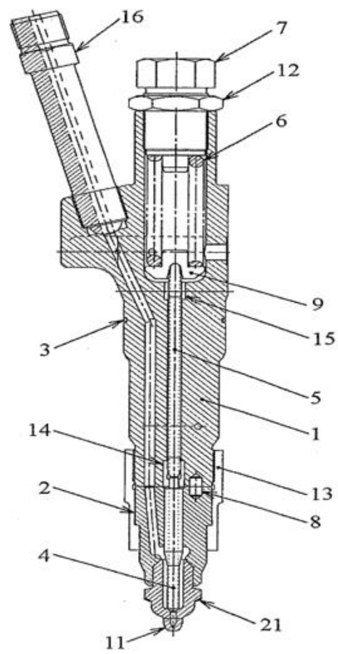

Figure 6 Injector section [8]
1-Injector body; 2-nozzle; 3- o-ring; 4-nozzle valve; 5- needle; 6-spring; 7-adjustment screw; 8-parallel pin; 9-spring lock component; 10-conical disk; 11-nozzle tip; 12-lock washer; 13-nut; 14, 15-spring guide, 16-duct; 17-bolt; 18-washer; 19-spring tube; 20-pine; 21- gasket

In this case, helical springs made of corrosion-protected stainless spring steel are used, cylindrical springs made of round wire with a constant diameter in a range of colours from dark grey to black.

The strength of the springs depends on several factors: period of use, elastic limit, load, etc.

During the operation of springs, residual stresses occur which place an additional load on the spring. Coil springs can lock if the elastic limit of the material is exceeded and plastic deformation can occur. Very long compression coil springs can buckle under higher loads.

Since it is impossible to take into account all real dynamic influences, the strength of the springs cannot be fully guaranteed.

To evaluate the properties of the spring, the “Spring characteristic” is taken into account, whose force F represents the dependence of the spring displacement. The ratio between the spring force and the spring stroke is called the spring constant. In cylindrical helical springs, a linear relationship is formed.

5.3. Initial calculation data

- Maximum load: $F_{max} = 1850\ N$
- Minimum load: $F_{min} = 860\ N$
- Working stroke: $s = 55\ mm$

Journal of Marine Technology and Environment
DOI:10.53464/JMTE.02.2026.10
ISSN (Print): 1844-6116
ISSN (Online): 2501-8795
https://www.jmte.eu

- Material density: $\rho = 7{,}87\ kg/mm^3$,
- Longitudinal modulus of elasticity: $E = 2{,}1 \cdot 10^5\ MPa$,
- Transverse modulus of elasticity: $G = 0{,}81 \cdot 10^5\ MPa$,
- Bearing coefficient: $\nu = 0{,}5$,
- Spring wire diameter: $d = 5\ mm$,
- Arc index: $i = 8$
- Coefficient of the distance between the turns: $k = 0{,}14$

Based on these data, two springs with the following characteristics are chosen from the standard:

Table 1. Characteristics of the spring

Symbol	Label	Unit of measurement	Spring 1	Spring 2
d	Spring wire diameter	mm	5	5
D_e	Outer diameter	mm	45	37
D_m	Average diameter	mm	40	32
D_i	Inner diameter	mm	35	27
L_0	Unstressed spring length	mm	95.5	110
n	Total number of turns		5.5	8.5
D_d	Guide mandrel diameter	mm	34.2	26.4
D_h	Guide bushing diameter	mm	46.3	38
R	Spring constant	N/mm	15.85	20.03
s	Bow stroke	mm	54.2	52.5
L_n	Permissible length related to force	mm	41.3	57.5
F_n	Spring force relative to length	N	859	1051.2
M	Spring weight	g	147.14	164.77

We calculate the weight of the two springs

$$M_1 = l_1 \cdot \frac{\pi \cdot d^2}{4} \cdot \rho = 147{,}14\ g \quad (1)$$

$$M_2 = l_1 \cdot \frac{\pi \cdot d^2}{4} \cdot \rho = 164{,}77\ g \quad (2)$$

One of the criteria for choosing the spring is: the lowest possible weight

Due to this criterion we will choose Spring 1 for the injector.

5.4. *Parameters calculation*

- Spring stiffness

$$c = \frac{F_{max} - F_{min}}{s} = \frac{1850 - 860}{55} = 18\ N/mm \quad (3)$$

- Minimum arrow

$$f_{min} = \frac{F_{min}}{c} = \frac{860}{18} = 47{,}8\ mm \quad (4)$$

- Maximum arrow

$$f_{max} = \frac{F_{max}}{c} = \frac{1850}{18} = 102{,}8\ mm \quad (5)$$

- Minumum winding diameter

$$D_m = i \cdot d = 8 \cdot 5 = 40\ mm \quad (6)$$

- Outer diameter

$$D_e = D_m + d = 40 + 5 = 45\ mm \quad (7)$$

- Inner diameter

$$D_i = D_m - d = 40 - 5 = 35\ m \quad (8)$$

- Number of active turns

$$n_c = \frac{G \cdot d}{8 \cdot c \cdot i^3} = \frac{0{,}81 \cdot 10^5 \cdot 5}{8 \cdot 18 \cdot 8^3} = \frac{81000 \cdot 5}{73728} = 5{,}5 \quad (9)$$

- Number of support turns

$$n_r = 1{,}5 \text{ pentru } n_c < 7$$

$$n_r = 2{,}5 \text{ pentru } n_c > 7 \quad (10)$$

- Total number of turns

$$n_t = n_c + n_r = 5{,}5 + 1{,}5 = 7 \quad (11)$$

- Length of locked spring

$$H_b = n_t \cdot d = 7 \cdot 5 = 35\ mm \quad (12)$$

- Minimum distance between active turns

Journal of Marine Technology and Environment
DOI:10.53464/JMTE.02.2026.10
ISSN (Print): 1844-6116
ISSN (Online): 2501-8795
https://www.jmte.eu

$$S_a = \left(0{,}0015 \cdot \frac{D_m^2}{d} + 0{,}1 \cdot d\right) \cdot n_s = \left(0{,}0015 \cdot \frac{40^2}{5} + 0{,}1 \cdot 5\right) \cdot 5{,}5 = 5{,}39\ mm \quad (13)$$

- Average distance between turns

$$m = \frac{L_0 - d}{n_s} = \frac{95{,}5 - 5}{5{,}5} = \frac{90{,}5}{5{,}5} = 16{,}45\ mm \quad (14)$$

- Unstressed spring pitch

$$t = d + \frac{f_{max}}{n_c} + d \cdot k = 5 + \frac{102{,}8}{5{,}5} + 5 \cdot 0{,}14 = 5 + 18{,}69 + 0{,}7 = 24{,}39\ \ mm \quad (15)$$

- Unstressed spring pitch

$$H_0 = H_b + n_c \cdot (t - d) = 35 + 5{,}5 \cdot (24{,}39 - 5) = 141{,}65\ mm \quad (16)$$

- Length of the assembled spring

$$H_{min} = H_0 - f_{min} = 141{,}65 - 47{,}8 = = 93{,}85\ mm \quad (17)$$

- Spring length at maximum load

$$H_{max} = H_0 - f_{max} = 141{,}65 - 102{,}8 = 38{,}85\ mm \quad (18)$$

- The angle of inclination of the unstressed spring coil

$$\alpha_0 = \frac{180}{\pi} \cdot \alpha \cdot tan\left(\frac{t}{\pi \cdot D_m}\right) = 8{,}5\ grade \quad (19)$$

- Length of spring wire

$$l_s = \frac{\pi \cdot D_m \cdot n_t}{cos(\alpha_0)} = \frac{3{,}14 \cdot 40 \cdot 7}{\cos 8{,}5^\circ} = \frac{879{,}2}{0{,}989} = 888{,}98\ mm \quad (20)$$

- Arrow at spring lock

$$f_b = min(H_0 - H_b) = \min(141{,}65 - 35) = 106{,}65\ mm \quad (21)$$

- Arrow at spring lock

$$F_b = c \cdot f_b = 18 \cdot 106{,}65 = 1919{,}7\ N \quad (22)$$

- Slenderness coefficient

$$\lambda = \frac{H_0}{D_m} = \frac{141{,}65}{40} = 3{,}54 \quad (23)$$

- Theoretical buckling deflection coefficient

$$c_f = \frac{0{,}5}{1 - \frac{G}{E}} = \frac{0{,}5}{1 - \frac{0{,}81 \cdot 10^5}{2{,}1 \cdot 10^5}} = 8{,}13 \quad (24)$$

- Critical slenderness ratio

$$\lambda_c = \frac{\sqrt{c_f}}{v} = \frac{\sqrt{8{,}13}}{0{,}5} = \frac{2{,}85}{0{,}5} = 5{,}7 \quad (25)$$

- Natural operating frequency of the spring

$$f = \frac{3{,}5 \cdot 10^5 \cdot d}{n_c \cdot D_m^2} = \frac{3{,}5 \cdot 10^5 \cdot 5}{5{,}5 \cdot 40^2} = \frac{1750000}{8800} = 198{,}86\ Hz \quad (26)$$

6. CONCLUSIONS

In high-power marine engines, heavy fuel injectors are used that do not differ essentially from diesel injectors. Due to the higher thermal regime of the atomizer, heavy fuel injectors must be cooled. In this regard, an additional channel is made in both the injector body and the atomizer, in which oil or water circulates. Water (distilled or treated, to avoid corrosion and deposits) is preferred for safety reasons. The cooling circuit of the injectors must be independent of the engine cooling circuit.

The injector body is made of OLC of cementation or improvement quality, the semi-finished product being obtained by die forging. The seating surface is carbonitrided and hardened to avoid deformation and ensure proper sealing.

The injector spring is required to have precise characteristics, and stabilization treatments are necessary to ensure that its qualities are maintained over time.

Based on the initial design data, two springs were chosen.

The weight of the two springs was calculated. In the end, one of the main criteria for choosing the spring was taken into account: the lowest possible weight, so Spring 1 was chosen.

The calculation of the parameters was performed and then it was checked whether the spring was chosen correctly.

The condition that is imposed

$$\boldsymbol{\lambda < \lambda_c => 3{,}54 < 5{,}7}$$

=> ***The condition is being checked.***

DOI:10.53464/JMTE.02.2026.10
ISSN (Print): 1844-6116
ISSN (Online): 2501-8795
https://www. jmte.eu

When overloaded, cases encountered in practice, the equivalent stresses do not exceed the breaking strength of the wire, so the spring resists and does not fail during operation.

7. CREdit authors statement

Conceptualization:T.M.; P.G.Gr.;

Data curation: T.M.; P.G.Gr.;

Formal analysis: T.M.; P.G.Gr.;

Funding acquisition: T.M.;

Investigation: T.M.; P.G.Gr.;

Methodology: T.M.;

Project administration: T.M.;

Resources: T.M.; P.G.Gr.;

Software: T.M.; P.G.Gr.;

Supervision: T.M.;

Validation: T.M.;

Visualization: T.M.;

Writing – original draft: T.M.;

Writing – review & editing: T.M..

8. REFERENCES

[1] Buzbuchi N, Dragalina A and Manea L, 1996 *Naval engines. Processes and features* (Bucuresti – Ed. Didactica si Pedagogica) vol 1

[2] https://www.scribd.com/doc/56591094/Motorul-Diesel, Accessed: 15/02/2026

[3] Buzbuchi N and Sabau A, 2001 *Naval internal combustion engines. Constuction and calculation* (Constanta – Ed. Ex Ponto)

[4]https://www.scribd.com/document/345775717/Pompe-de-Injectie-Tipuri-Rol

[5] Gaiginschi R, 2014 *Internal combustion engines* (Iasi – Ed. Ghe. Asachi) vol I

[6] Stefanescu I, Spanu C, 2011, Organe de masini, Vol.1, Ed. Europlus, Galati

[7] Jula A, Lates M, 2004 Organe de masini, Ed. Universitatii Transilvania, Brasov

[8] Technical documentation MAN B&W engine on board the ship

[9] Katelieva, E., 2022, *Methodology for energy efficiency improvement of ship motor driven systems*, Journal of Marine Technology and Environment, Vol. 2, pp28-32, Constanta, Nautica Publish Hoiuse, Romania.

Journal of Marine Technology and Environment
DOI:10.53464/JMTE.02.2026.11
ISSN (Print): 1844-6116
ISSN (Online): 2501-8795
https://www.jmte.eu

OPTIMIZING MARITIME SUPPLY CHAINS USING ARTIFICIAL INTELLIGENCE AND BIG DATA

Dumitru-Cătălin VASILE[1]

[1]National University of Political Studies and Public Administration (SNSPA), Doctoral School of Political Science, 30A Expoziţiei Boulevard, 012104, Bucharest, Romania, ORCID iD: 0009-0003-3257-4156, e-mail address: catalin.vasile@outlook.com

Abstract: Maritime transport carries over 80% of global merchandise trade by volume, yet the sector faces mounting pressure from chokepoint disruptions, port congestion, freight rate volatility and decarbonization mandates. This paper examines how the convergence of artificial intelligence (AI) and big data analytics can optimize maritime supply chains across four operational layers: voyage and route optimization, port and terminal operations, predictive asset maintenance, and end-to-end visibility. Drawing on a structured review of recent peer-reviewed literature and industry evidence, the study synthesizes reported performance gains, including vessel estimated-time-of-arrival prediction errors in the range of roughly 0.25–5% depending on the dataset and method, container handling-time reductions of up to 25%, and idle-equipment reductions of 15–20% in digital-twin-enabled terminals. A four-layer conceptual framework is proposed that links Automatic Identification System (AIS) data streams, machine-learning models and digital twin simulations to measurable supply-chain key performance indicators. The framework is then mapped to the Port of Constanța, the largest port on the Black Sea, as an illustrative application from which a staged optimization roadmap is derived, building on the port's current Port Community System programme; a design for the empirical validation of the framework is also specified. The paper analyses the principal barriers to adoption, namely data quality and interoperability, cybersecurity exposure, infrastructure readiness and organizational capability, and outlines a phased implementation pathway for port authorities and shipping operators. The findings indicate that AI and big data are structural enablers of resilient, efficient and lower-emission maritime logistics rather than incremental tools.

Key words: artificial intelligence, big data, digital twin, maritime supply chain, Port of Constanța, predictive analytics.

1. INTRODUCTION

Maritime transport is the backbone of global commerce. According to the United Nations Conference on Trade and Development, around 80% of the volume of international trade in goods is carried by sea, and global maritime trade reached 12,720 million tons in 2024, up 2.2% from the previous year [1]. The sector, however, operates in an exceptionally demanding environment: geopolitical tensions and climate risks have placed strategic chokepoints under severe pressure, with Red Sea transits falling roughly 70% below 2023 averages as vessels reroute around the Cape of Good Hope, lengthening voyages, raising freight rates and increasing greenhouse gas emissions [1]. Maritime trade is forecast to slow to just 0.5% growth in 2025 amid this volatility [1]. These disruptions expose a structural vulnerability of contemporary supply chains: they are optimized for cost under stable conditions but are fragile when confronted with shocks.

In parallel, the maritime industry has entered an accelerated phase of digitalization. The Automatic Identification System (AIS), satellite connectivity, port sensor networks and terminal operating systems generate continuous, high-volume data streams describing vessel movements, cargo flows and asset conditions [2]. Reviews of emerging maritime technologies converge on one observation: the defining challenge is no longer data scarcity but the capacity to turn data into timely decisions [3]. Artificial intelligence (AI) and big data analytics provide exactly this capability, since big data technologies enable the storage and processing of vast, heterogeneous datasets, while AI methods derive predictive and prescriptive insights from them [2].

This paper examines how the convergence of AI and big data can optimize maritime supply chains. It pursues three objectives: first, to structure the application domain into clearly defined operational layers; second, to synthesize the quantitative evidence on performance improvements reported in recent literature; and third, to propose a conceptual framework and implementation pathway that connect data sources, analytical models and supply-chain key performance indicators (KPIs). Section 2 sets out the methodology and Section 3 the technological foundations. Section 4 presents the four-layer framework, Section 5 applies it to the Port of

Journal of Marine Technology and Environment
DOI:10.53464/JMTE.02.2026.11
ISSN (Print): 1844-6116
ISSN (Online): 2501-8795
https://www. jmte.eu

Constanța, and Section 6 specifies a validation design. Section 7 discusses adoption barriers and Section 8 concludes.

2. METHODOLOGY

This study combines a structured narrative review with conceptual synthesis. The aim is to organize a fragmented, rapidly evolving body of knowledge into a framework useful to researchers and practitioners rather than to perform a statistical meta-analysis.

The literature base was assembled through a structured search of four academic databases: Scopus, Web of Science Core Collection, IEEE Xplore and ScienceDirect, supplemented by Google Scholar queries capturing conference proceedings and recent preprints. The search was conducted between January and April 2026 and covered material published between January 2019 and March 2026, with a few seminal earlier works retained as canonical references. Search strings combined three concept blocks using Boolean operators: a maritime domain block ("maritime" OR "shipping" OR "port" OR "vessel" OR "container terminal"), a technology block ("artificial intelligence" OR "machine learning" OR "deep learning" OR "big data" OR "digital twin" OR "AIS"), and an application block ("supply chain" OR "optimization" OR "ETA prediction" OR "berth allocation" OR "predictive maintenance" OR "visibility"). Reference network expansion from the most recent bibliometric review of the field [4] was used to identify additional high-impact sources missed by keyword searches.

Screening proceeded in three stages. The initial queries returned approximately 380 records, reduced to 220 after duplicate removal and language filtering (English only). Title and abstract screening narrowed this to 71 candidates, of which 47 were retained after full-text reading. Inclusion required explicit relevance to maritime logistics, port operations or maritime supply-chain management; a clearly identified role for artificial intelligence, machine learning or big data analytics; empirical results, a validated prototype or a substantive conceptual contribution; publication in a peer-reviewed venue or issuance by a recognized body such as UNCTAD, the IMO or a national port authority; and availability of the full text. Sources addressing AI only in non-maritime modes, mentioning it in passing, lacking the methodological detail needed to interpret reported figures, or duplicating a more comprehensive source were excluded. Grey literature was included selectively, flagged as such, and used to corroborate deployment figures not yet documented academically. Empirical studies were assessed against a lightweight checklist covering dataset transparency, clarity of method description, presence of a baseline comparator and explicit reporting of evaluation metrics; those failing two or more criteria were retained for context only and not used as sources of quantitative claims.

The selected material was then analyzed thematically using an inductive coding approach. Each source was coded against three dimensions: data sources used, analytical method applied and reported performance indicator. The coded entries were grouped into the four operational layers that structure Section 4, and for each layer the dominant data sources, prevailing techniques and reported indicators were consolidated into the conceptual framework.

Two limitations follow from this design and are examined in Section 7.1: the reported performance metrics are highly heterogeneous, and a structured narrative review retains an element of analyst judgment. The search strings, databases and screening counts are reported above to make that judgment transparent and the procedure replicable.

To strengthen the framework beyond synthesis, two further components were added, both positioned as proposal-oriented rather than confirmatory. A single illustrative application, the Port of Constanța, was selected because it combines regional significance, documented exposure to disruption and a publicly reported digitalization programme; it is examined using port-authority statistics, official communications, regulator and industry reporting, and Eurostat data. In addition, a validation design is specified to test the framework empirically rather than accept it on conceptual grounds alone. Both are presented as a research agenda for subsequent work, and claims about benefits in Section 5 are formulated as expected returns drawn from the reviewed literature rather than as outcomes already realized at Constanța.

3. TECHNOLOGICAL FOUNDATIONS

Optimizing maritime supply chains with AI rests on three interdependent pillars: the data layer, the analytics layer and the decision layer.

3.1 The maritime big data landscape

Maritime operations generate data with the classic characteristics of big data: high volume, high velocity and considerable variety. The Automatic Identification System is the single most important source, broadcasting vessel position, speed, course and identity at frequent intervals to terrestrial and satellite receivers that aggregate billions of such messages [5]. This is complemented by terminal operating system records, quay-crane and yard-equipment telemetry, gate transactions, meteorological and oceanographic feeds, and engine and sensor data from increasingly instrumented vessels [2]. Big data analytics enables maritime businesses to evaluate and forecast cargo

Journal of Marine
Technology and Environment
DOI:10.53464/JMTE.02.2026.11
ISSN (Print): 1844-6116
ISSN (Online): 2501-8795
https://www. jmte.eu

flows, optimize routes and minimize superfluous voyages [6].

The central difficulty is integration. Data originates from many actors, including shipping lines, terminals, port authorities, customs and freight forwarders, in incompatible formats and with uneven quality. Bibliometric analysis of the field confirms that system and technology integration, alongside cyber-attack risk, is among the most frequently cited open problems in maritime big data research [4]. Without a coherent data foundation, advanced analytics cannot deliver reliable results.

3.2 Artificial intelligence and machine-learning methods

On the analytics layer, supervised machine-learning models, including random forests, gradient-boosting methods such as XGBoost and LightGBM, and deep neural networks, dominate predictive tasks such as estimated time of arrival (ETA) forecasting and demand prediction [7][8]. Sequence models, in particular long short-term memory networks, are well suited to the temporal structure of vessel-trajectory data [9]. Reinforcement learning is increasingly applied to sequential decision problems such as crane sequencing and yard allocation, where an agent learns policies that balance productivity against future congestion risk [10].

A complementary technology is the digital twin: a continuously updated virtual representation of a vessel, terminal or port. Combining historical data with live telemetry, it lets operators simulate alternative berth schedules, stacking strategies and equipment assignments before applying them live, shifting from reactive firefighting to proactive planning [10][11]. Together these methods form the decision layer, where predictive and prescriptive outputs become operational instructions.

4. A FOUR-LAYER FRAMEWORK FOR SUPPLY-CHAIN OPTIMIZATION

This section presents the core contribution: a framework organizing AI and big data applications into four operational layers of the maritime supply chain. Figure 1 illustrates it; Table 2 summarizes the data sources, methods and reported gains for each layer.

The framework is intentionally layered rather than monolithic. Each layer can be adopted incrementally and delivers value on its own, but the largest benefits arise when the layers share a common data foundation. Its logic follows the physical flow of a maritime supply chain, from the voyage at sea through the port interface to the assets that sustain operations, and finally to the informational layer that binds the chain together.

4.1 Voyage and route optimization

The first layer concerns the vessel in transit. Accurate prediction of vessel ETA is fundamental because port resource planning, berth allocation and downstream land-side logistics all depend on it; inaccurate ETAs propagate as a ripple effect, leading to schedule disruptions, congestion and reduced terminal effectiveness [12]. Machine-learning models trained on historical AIS data have substantially improved ETA accuracy. A study using AIS data from the Port of Houston reported a mean absolute percentage error of approximately 5% with an XGBoost model [7]. In comparison, a hybrid tree-based stacking ensemble applied to Baltic Sea traffic achieved a mean absolute percentage error of 0.25% [8]. The two figures are not directly comparable: they come from different datasets, regions, vessel populations and prediction horizons, and illustrate a range of plausible accuracy rather than a like-for-like benchmark.

Big data analytics also supports weather routing and speed optimization: analyzing meteorological and oceanographic data alongside vessel performance, AI systems recommend routes and speeds that cut fuel consumption and emissions [6][13]. Dynamic rerouting in response to predicted congestion helps vessels avoid costly waiting time, improving schedule reliability and just-in-time coordination across the wider chain [2].

Table 1 makes this heterogeneity explicit. Ensemble and deep-learning methods consistently outperform classical baselines, but reported accuracy is strongly conditioned by dataset, geographic scope and the definition of the prediction horizon, which is why the standardized benchmark discussed in Section 6 is needed before such figures can be treated as comparable.

Journal of Marine Technology and Environment
DOI:10.53464/JMTE.02.2026.11
ISSN (Print): 1844-6116
ISSN (Online): 2501-8795
https://www. jmte.eu

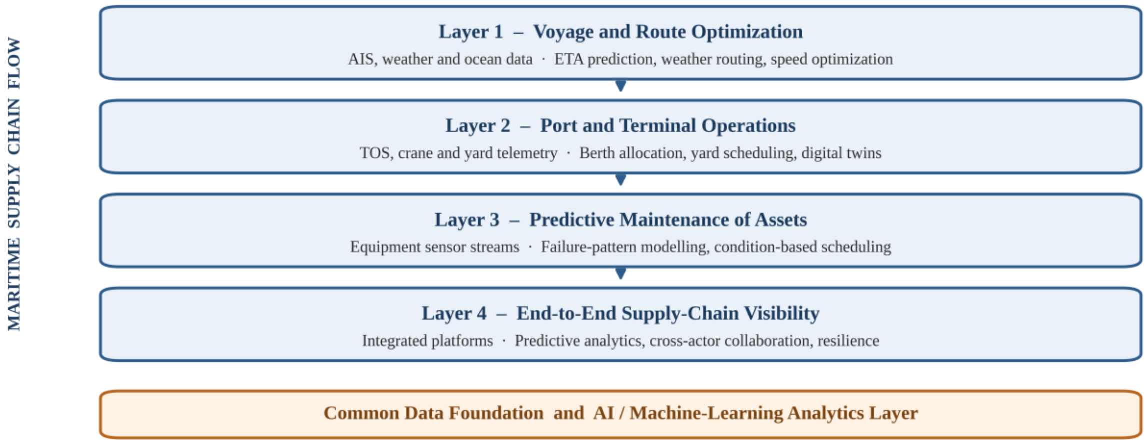

Figure 1 Conceptual four-layer framework for optimizing maritime supply chains with artificial intelligence and big data

Table 1. Comparison of representative machine-learning studies on vessel estimated-time-of-arrival (ETA) prediction

Study (reference)	Dataset / region	Method	Accuracy reported	Scope
Yu et al. 2024 [7]	Port of Houston, USA (2018–2020)	XGBoost with trajectory features	MAPE ≈ 5%	Narrow-waterway transit
Hossain et al. 2025 [8]	Baltic Sea AIS	Hybrid tree-based stacking ensemble	MAPE ≈ 0.25%	Seaport-bound vessels
El Mekkaoui et al. 2023 [9]	Bulk-port vessels, Mediterranean	LSTM / sequence models	Sequence models outperform baselines	Bulk-port arrivals
Xu et al. 2025 [14]	Container vessels, AIS	ML prediction coupled to the berth-allocation model	Reduced berth conflict	Berth scheduling

MAPE = mean absolute percentage error. Accuracy metrics are not directly comparable across studies because of differences in datasets, regions and prediction horizons; see Section 2.

4.2 Port and terminal operations

The second layer addresses the port-terminal interface, where the maritime and land-side chains meet and congestion costs are most acute. Accurate ETA predictions feed directly into berth allocation: integrating real-time AIS forecasts with berth scheduling models mitigates conflicts caused by arrival uncertainty and improves resource utilization [14]. Within the terminal, machine-learning models anticipate yard congestion and gate queues, supporting stacking, sequencing and truck-appointment decisions [15].

Digital twin technology amplifies these gains by enabling risk-free experimentation with yard layouts, crane allocations and berth schedules in a virtual environment before changes reach the quay [11][15]. Industry evidence and selected case-study reports indicate that integrated simulation and analytics can reduce idle equipment time by 15–20% and increase throughput by 10–12%, with some deployments reporting container-handling time reductions of up to 25% [15][16]. These figures are drawn from heterogeneous and partly vendor-reported sources and are conditioned on their baseline, so they indicate plausible upper bounds rather than guaranteed outcomes. With that caveat, the improvements they describe would shorten vessel turnaround and stabilize schedule reliability.

4.3 Predictive maintenance of assets

The third layer concerns the physical assets (vessels, quay cranes and yard equipment) whose availability determines supply-chain continuity. By monitoring telemetry and modeling wear and failure patterns, AI-driven predictive maintenance lets operators schedule repairs in low-impact windows rather than react to breakdowns [16]. This reduces emergency downtime, extends asset life and protects quay productivity during demand peaks.

4.4 End-to-end supply-chain visibility

The fourth layer is informational. It integrates maritime data with the broader supply-chain management systems used by shippers and logistics

Journal of Marine Technology and Environment
DOI:10.53464/JMTE.02.2026.11
ISSN (Print): 1844-6116
ISSN (Online): 2501-8795
https://www. jmte.eu

providers, creating a seamless, end-to-end view of operations [2]. Cloud-based platforms and collaboration tools let ports, shipping lines and logistics providers synchronize operations, making the system more agile [17]. Real-time visibility into vessel positions and arrival times improves coordination with land-side logistics, supports just-in-time delivery and reduces inventory holding costs [2].

This layer is also where AI most directly supports resilience. Predictive analytics across integrated data can give early warning of disruption and quantify its propagation, letting operators pre-position resources and reroute flows. Given the documented vulnerability of maritime chokepoints, this capability is strategic rather than merely operational [1].

Table 2. Summary of AI and big data applications across the four optimization layers of the maritime supply chain

Optimization layer	Primary data sources	Dominant AI / analytics methods	Reported performance gains
Voyage and route optimization	AIS, weather and ocean data, vessel performance	XGBoost, LightGBM, stacking ensembles, LSTM	ETA error 0.25–5% MAPE [7][8]
Port and terminal operations	Terminal operating system, crane and yard telemetry, gate logs	Berth-allocation optimization, digital twins, reinforcement learning	Idle time −15–20%; throughput +10–12% [15][16]
Predictive maintenance	Equipment sensor and telemetry streams	Anomaly detection, failure-pattern modeling	Reduced unplanned downtime [16]
End-to-end visibility	Integrated maritime and supply-chain platforms	Predictive analytics, cloud collaboration	Lower inventory and disruption cost [2][17]

Reported figures are indicative orders of magnitude drawn from heterogeneous studies and deployments; see Section 2.

5. CASE STUDY: APPLYING THE FRAMEWORK TO THE PORT OF CONSTANȚA

This section applies the framework to the Port of Constanța, the largest port on the Black Sea and the principal maritime gateway of Romania and its landlocked Central and Eastern European hinterland. It is an instructive case because it combines significant scale, acute exposure to disruption and an active but early-stage digitalization programme, precisely the conditions under which a layered approach is most relevant, and because the blue economy and Black Sea risk have become explicit regional policy priorities [18].

5.1 Operational profile and the case for optimization

Constanța is a port of call covering almost 3,926 hectares, offering depths of up to 18.5 meters and a direct link to the Danube via the Danube–Black Sea Canal [19]. Its recent traffic illustrates the volatility that motivates this study. In 2023 the port handled a record 92.7 million tonnes; in 2024 total tonnage fell by roughly 14% according to Eurostat, the steepest decline among major EU ports, as Ukrainian grain transit was redirected once Ukraine reopened its own export corridor [20]. Container traffic moved in the opposite direction: throughput reached 989,795 TEU in 2024, up from 884,598 TEU in 2023, and had surged by more than 30% between 2022 and 2024 as the port absorbed boxed cargo redirected from blockaded Ukrainian ports [21][22]. This divergence, contracting bulk tonnage alongside expanding container volumes, is itself an argument for the demand-uncertainty-aware optimization the framework provides. The port operates under a landlord model serving around 40 private operators, with the DP World-operated Constanța South Container Terminal as its main container facility [19][23].

This profile generates exactly the optimization problems the framework addresses. Volatile growth in container and grain volumes, the latter dependent on the Ukrainian export corridor, creates demand uncertainty that strains berth and yard planning [21]. Redirected Ukrainian containers caused congestion at terminal gates and at the entrance from the Danube Canal, a bottleneck the port has identified as a priority [22][23], and the berth-allocation and yard-scheduling gains summarized in Table 2 indicate the order of magnitude of potential improvement. The multiplicity of independent operators and public agencies (customs, border police, and veterinary and sanitary authorities) creates the fragmented information environment that Layer 4 is designed to integrate. Constanța thus offers a plausible, publicly documented setting for the framework, though the mapping is conceptual: it has not been validated against the port's operational data, and the benefits remain expected rather than measured.

5.2 Current digitalization baseline

Constanța is not starting from zero. The National Company Maritime Ports Administration S.A. Constanța has launched a digitalization programme centred on a Port Community System (PCS): a neutral, open platform serving as a one-stop shop for secure information exchange between public and private stakeholders [23]. The port joined the International Port Community Systems Association in 2020, and in 2024 a Romanian, German and Estonian consortium delivered the PCS specification; the system is designed to connect to the

Journal of Marine Technology and Environment
DOI:10.53464/JMTE.02.2026.11
ISSN (Print): 1844-6116
ISSN (Online): 2501-8795
https://www. jmte.eu

national Maritime Single Window [22][24]. A complementary truck appointment-booking application has also been developed to reduce congestion at the port gates [23].

Mapped onto the framework, this baseline corresponds principally to the foundational data layer and the early stages of Layer 4 (end-to-end visibility). The PCS standardizes and centralizes documentary and procedural data flows, a precondition for, but not equivalent to, analytical optimization. The predictive and prescriptive capabilities of Layers 1 to 3 are not yet part of the publicly documented programme. The case therefore illustrates a common situation: a port that has begun the digital groundwork but has not converted it into AI-driven decision support.

5.3 A staged optimization roadmap for Constanța

The framework translates this gap into a staged roadmap. In the near term, the PCS and the Maritime Single Window should be consolidated into a common data foundation, with explicit attention to data quality and interoperability, so that later analytics rest on reliable inputs. As an early-value step within Layer 1, AIS-based ETA prediction could be deployed for vessels approaching through the Bosphorus; Table 1 indicates such models are mature and that better berth planning and reduced waiting time are plausible, though the magnitude at Constanța would need a pilot calibrated to the port's own traffic.

In the medium term, the truck-appointment system provides a natural entry point for Layer 2: its booking data, combined with terminal-operating-system and gate records, could feed machine-learning models that anticipate gate and yard congestion, while a digital twin of the container terminal would allow berth and stacking strategies to be tested virtually before deployment. Layer 3 could be introduced in parallel by instrumenting quay cranes and yard equipment for condition-based maintenance. In the longer term, extending the PCS with predictive analytics across all operators and agencies would complete Layer 4, turning the platform into a decision-support system with early warning of disruption, which is of particular value given the exposure of Constanța to Black Sea geopolitical risk. Demonstrating realized benefits would require partnership with the port authority and access to operational data.

6. TOWARDS EMPIRICAL VALIDATION OF THE FRAMEWORK

A framework derived from a structured review must ultimately be tested against data. This section outlines a design through which the framework, and the Constanța roadmap in particular, could be validated. The aim is to specify a falsifiable evaluation rather than to report results.

6.1 Proposed methodology and data

The most tractable starting point is Layer 1. A validation study would assemble a historical AIS dataset of vessels arriving at Constanța over at least 12 months, enriched with meteorological and oceanographic data and actual berthing times from port records. Following the ETA literature, the data would be split by vessel route rather than at random, avoiding the optimistic bias that arises when trajectory segments from one voyage appear in both training and test sets [8]. Several model families (a regression baseline, gradient-boosting methods such as XGBoost and LightGBM, and a sequence model such as an LSTM) would be trained and compared, mirroring the studies summarized in Table 1.

For Layer 2, validation would take the form of a discrete-event simulation or digital twin of the container terminal, calibrated on historical terminal operating system and truck appointment data. It would compare a baseline reproducing current practice with scenarios in which berth allocation and yard stacking are driven by predictive models, isolating the marginal contribution of optimization under reproducible conditions.

6.2 Evaluation metrics and hypotheses

Validation requires metrics defined in advance. For Layer 1, the primary metric is the mean absolute percentage error of ETA prediction, with mean absolute error in hours as a more interpretable secondary measure. For Layer 2, the metrics are average vessel turnaround time, berth and quay-crane utilization, container dwell time and gate turnaround time, all of which connect to the KPIs identified in Section 4.

The study would test three hypotheses. First, that machine-learning models reduce ETA error relative to the schedule-based estimates currently used (H1). Second, that feeding these predictions into berth-allocation and yard-planning logic reduces turnaround time and raises equipment utilization against the baseline (H2). Third, that the largest gains arise when layers share a common data foundation rather than operate in isolation (H3), testing the central integration claim. Stating these hypotheses explicitly makes the framework falsifiable.

7. DISCUSSION: ADOPTION BARRIERS AND IMPLEMENTATION PATHWAY

The evidence reviewed above demonstrates substantial potential, yet adoption remains uneven, as the Constanța case illustrates. Four barriers recur. The first is data quality and interoperability: fragmented and sometimes incomplete data undermines model reliability,

DOI:10.53464/JMTE.02.2026.11
ISSN (Print): 1844-6116
ISSN (Online): 2501-8795
https://www. jmte.eu

and the absence of common standards impedes the data sharing on which integrated optimization depends [4]. The second is cybersecurity: as operations become data-driven and interconnected the attack surface expands, and cyber risk is consistently identified as a leading concern [4][25]. The third is infrastructure readiness, particularly the uneven sensorization and connectivity of ports and fleets [26]. The fourth is organizational capability: realizing value from AI requires analytical skills, redesigned processes and cross-actor governance, a point underscored by practitioners on the Constanța PCS, who stress that digitalization is above all a change in working practices rather than a technical upgrade [24].

These barriers suggest a phased pathway, with the Constanța roadmap in Section 5.3 as a concrete instance. The first phase establishes the data foundation: instrumentation, data-quality management and interoperability standards, since every subsequent gain depends on it. The second deploys predictive analytics on a single high-value layer such as ETA prediction, where evidence of return is strongest and disruption least. The third introduces digital-twin simulation and prescriptive optimization for terminal operations. The fourth integrates the layers and extends visibility across actors, embedding cybersecurity and data governance throughout.

Two cross-cutting themes deserve emphasis. First, optimization and sustainability are complementary rather than competing: reductions in idle time, rerouting and superfluous voyages cut both cost and emissions, aligning AI adoption with the decarbonization agenda [6][13]. Second, benefits scale with integration; isolated pilots yield modest returns, whereas a shared data foundation across the four layers compounds them.

7.1 Limitations

Four limitations of the present study should be made explicit. First, the synthesis is a structured narrative review, not a PRISMA-compliant systematic review with independent dual screening; analyst judgment enters inclusion decisions, and the search strategy in Section 2 makes that judgment transparent rather than eliminating it. Second, the performance figures cited throughout come from heterogeneous studies and partly from vendor or industry sources, and should be read as indicative orders of magnitude rather than directly comparable benchmarks. Third, the Constanța case is an illustrative application rather than a completed empirical case study: it incorporates no primary field data, operator interviews or terminal-level operational records, so its findings are a mapping of the framework onto a real port rather than measured outcomes. Fourth, several sources in that analysis are online institutional and industry publications; while appropriate for documenting a live digitalization programme, they limit independent verification. The validation design in Section 6 is the planned response to the second and third of these limitations.

8. CONCLUSIONS

This paper has examined how the convergence of artificial intelligence and big data can optimize maritime supply chains. It proposed a four-layer framework covering voyage and route optimization, port and terminal operations, predictive maintenance and end-to-end visibility. The quantitative evidence for each layer was synthesized, with the heterogeneity of the underlying studies acknowledged throughout. The framework was then mapped to the Port of Constanța; the resulting staged roadmap shows how it can be operationalized at a specific port, while stopping short of demonstrating realized benefits, which would require validation against operational data.

The analysis supports three conclusions. First, the technological foundations are mature enough for operational deployment, but value depends decisively on the quality and interoperability of the underlying data. Second, the principal obstacles are organizational and infrastructural rather than algorithmic, which is why a phased pathway, instantiated here as the Constanța roadmap, is essential. Third, AI and big data are structural enablers of resilient, efficient and lower-emission maritime logistics in an era of chokepoint vulnerability and decarbonization pressure.

Future research should pursue the validation design of Section 6, beginning with AIS-based ETA prediction for Constanța and extending to digital twin simulation of its container terminal. Standardized benchmarks are needed to make cross-study results comparable, along with methods for secure multi-actor data sharing and longitudinal studies measuring realized rather than projected benefits. Testing the integration hypothesis empirically would be the most valuable single contribution of that work.

9. ACKNOWLEDGMENTS

The author is grateful to the Doctoral School of the National University of Political Studies and Public Administration (SNSPA), Bucharest, for the academic framework within which this research was developed.

10. FUNDING

This research received no specific grant from any funding agency in the public, commercial or not-for-profit sectors.

11. CREDIT AUTHORS STATEMENT

Conceptualization: D.-C. V.; Data curation: D.-C. V.; Formal analysis: D.-C. V; Funding acquisition: not

DOI:10.53464/JMTE.02.2026.11
ISSN (Print): 1844-6116
ISSN (Online): 2501-8795
https://www.jmte.eu

applicable; Investigation: D.-C. V; Methodology: D.-C. V; Project administration: D.-C. V; Resources: D.-C. V; Software: not applicable; Supervision: D.-C. V; Validation: D.-C. V; Visualization: D.-C. V; Writing – original draft: D.-C. V; Writing – review and editing: D.-C. V.

12. REFERENCES

[1] United Nations Conference on Trade and Development, 2025, " Review of Maritime Transport 2025: Staying the Course in Turbulent Waters", UNCTAD/RMT/2025, United Nations, Geneva.

[2] United Nations Conference on Trade and Development, 2024, " Navigating the future: how AI, big data and autonomous systems are reshaping maritime transport", UNCTAD, Geneva, https://unctad.org (accessed 19.05.2026).

[3] Bulat V., Cojocaru I., 2024, " Beyond the horizon: future technologies transforming maritime navigation", *Journal of Marine Technology and Environment*, Vol. II, NAUTICA Publishing House, Constanta, Romania.

[4] Munim Z.H., Dushenko M., Jimenez V.J., Shakil M.H., Imset M., 2020, " Big data and artificial intelligence in the maritime industry: a bibliometric review and future research directions", *Maritime Policy & Management*, Vol.47, no.5, pp.577–597, Taylor & Francis, London.

[5] Yang D., Wu L., Wang S., Jia H., Li K.X., 2019, " How big data enriches maritime research: a critical review of Automatic Identification System (AIS) data applications", *Transport Reviews*, Vol.39, no.6, pp.755–773, Taylor & Francis, London.

[6] Cariou P., Parola F., Notteboom T., 2019, " Towards low carbon global supply chains: a multi-trade analysis of CO_2 emission reductions in container shipping", *International Journal of Production Economics*, Vol.208, pp.17–28, Elsevier, Amsterdam.

[7] Yu H., Fang Z., Murray A.T., Peng G., Lu F., 2024, " Automatic Identification System-based prediction of tanker and cargo estimated time of arrival in narrow waterways", *Journal of Marine Science and Engineering*, Vol.12, no.2, art.215, MDPI, Basel.

[8] Hossain N.U.I., Sakib N., Govindan K., 2025, " High-accuracy prediction of vessels' estimated time of arrival in seaports: a hybrid machine learning approach", *Machine Learning with Applications*, Vol.20, art.100005, Elsevier, Amsterdam.

[9] El Mekkaoui S., Benabbou L., Berrado A., 2023, " Deep learning models for vessel's ETA prediction: bulk ports perspective", *Flexible Services and Manufacturing Journal*, Vol.35, no.1, pp.5–28, Springer, Berlin.

[10] Hofmann E., Rusch M., 2023, " Industry 4.0 and the digital twin in container terminal operations: a review of scheduling and optimization applications" *Computers & Industrial Engineering*, Vol.178, art.109173, Elsevier, Amsterdam.

[11] Klievink B., van Stijn E., Hofman W., 2024, " Digital twins for ports and terminals: applications in berth allocation and yard scheduling", *Journal of Shipping and Trade*, Vol.9, art.11, Springer, Berlin.

[12] Heilig L., Lalla-Ruiz E., Voß S., 2020, " Digital transformation in maritime ports: analysis and game-theoretic framework", *Flexible Services and Manufacturing Journal*, Vol.32, no.1, pp.65–97, Springer, Berlin.

[13] Perera L.P., Mo B., 2017, " Machine intelligence-based data handling framework for ship energy efficiency", *IEEE Transactions on Industrial Electronics*, Vol.64, no.12, pp.9529–9537, IEEE, New York.

[14] Xu L., Yang Z., Chen J., Zou Z., 2025, "An optimization study on dynamic berth allocation based on vessel arrival time prediction", *Ocean Engineering*, Vol.322, art.120512, Elsevier, Amsterdam.

[15] Notteboom T., Pallis A., Rodrigue J.-P., 2022, "Port Economics", *Management and Policy*, Routledge, London.

[16] Kapkaeva N., Gurzhiy A., Maydanova S., Levina A., 2021, " Digital platform for maritime port ecosystem: Port of Hamburg case", *Transportation Research Procedia*, Vol.54, pp.909–917, Elsevier, Amsterdam.

[17] Lee P.T.-W., Kwon O.K., Ruan X., 2019, " Sustainability challenges in the maritime transport and logistics industry and its way ahead", *Sustainability*, Vol.11, no.5, art.1331, MDPI, Basel.

[18] Lyubcheva M., Dimitrov M., Barhalescu M., 2025, " How to address the challenges in the Black Sea region in the context of the development of the blue economy", *Journal of Marine Technology and Environment*, Vol. II, NAUTICA Publishing House, Constanta.

[19] National Company Maritime Ports Administration S.A. Constantza, 2024, " Port of Constantza: infrastructure, operators and cargo traffic", MPA Constantza, Constanta,

Journal of Marine Technology and Environment
DOI:10.53464/JMTE.02.2026.11
ISSN (Print): 1844-6116
ISSN (Online): 2501-8795
https://www. jmte.eu

https://www.portofconstantza.com (accessed 19.05.2026).

[20] Eurostat, 2025, " Maritime transport of goods: annual data, Eurostat", Luxembourg, https://ec.europa.eu/eurostat (accessed 19.05.2026).

[21] United Nations Conference on Trade and Development, 2025, " Container port throughput, annual", UNCTAD stat, Geneva, https://unctadstat.unctad.org (accessed 19.05.2026).

[22] Maritime Executive, 2024, " The Black Sea container market has adapted to disruption", *The Maritime Executive*, 22 May 2024, https://maritime-executive.com (accessed 19.05.2026).

[23] Horovei S., 2024, Constantza Port Community System, Danube Commission, Expert Group on Ports, Budapest, https://www.danubecommission.org (accessed 19.05.2026).

[24] HPC Hamburg Port Consulting, 2024, " Romanian-German-Estonian team delivers specification for Port Community System (PCS) to Port of Constantza", *HPC Hamburg Port Consulting*, Hamburg, https://www.hamburgportconsulting.com (accessed 19.05.2026).

[25] Tam K., Jones K., 2019, " Maritime cybersecurity policy: the scope and impact of evolving technology on international shipping", *Journal of Cyber Policy*, Vol.4, no.2, pp.147–164, Taylor & Francis, London.

[26] Munim Z.H., Saha R., Skuld H., Schøyen H., Sornn-Friese H., 2024, " Autonomous ships and digitalization in the maritime supply chain: opportunities and barriers" , *Maritime Economics & Logistics*, Vol.26, no.2, pp.320–343, Springer, Berlin.

PUBLISHED SINCE : 2008

ISSN (Print): 1844-6116 ISSN (Online): 2501-8795

ON LINE SINCE : 2008

https://www. jmte.eu

PUBLISHED BY : EDITURA NAUTICA/CONSTANTA MARITIME UNIVERSITY

ISSN: 1844-6116